

Towards a Better Understanding of the Fundamental Period of Metal Building Systems

Santiago Bertero

Thesis submitted to the Faculty of the
Virginia Polytechnic Institute and State University
in partial fulfillment of the requirements for the degree of

Master of Science

in

Civil Engineering

Rodrigo Sarlo, Chair

Finley A. Charney

Matthew R. Eatherton

May 9, 2022

Blacksburg, Virginia

Keywords: Metal Buildings, Seismic Design, Operational Modal Analysis, Equivalent

Lateral Force, Non-Structural Elements

Copyright 2022, Santiago Bertero

Towards a Better Understanding of the Fundamental Period of Metal Building Systems

Santiago Bertero

(ABSTRACT)

Metal buildings account for over 40% of low-rise construction in the US. Despite this, predictive fundamental period equations that were obtained empirically for mid-rise construction are used in seismic design. Analytical modeling of metal building frames implied that these equations significantly underpredict the period, which led to the development of a new predictive equation. However, experimental tests showed that these models may overestimate the measured period.

In this work, further tests were carried out in order to single out possible causes. Buildings were tested during different stages of construction to evaluate how non-structural elements could affect the behavior. Both planar and three-dimensional models were developed to determine if design assumptions are accurate for the purpose of estimating the period.

The results from tests showed that, unlike other single-story buildings, non-structural components seem to have negligible effect on the structural behavior. However, several buildings seemed to exhibit signs of fixed conditions at the column base. This assertion was corroborated by updating the analytical models. The two modeling approaches showed good agreement with each other as well, validating the use of planar models to predict the period. Finally, new predictive equations are proposed that take into account the type of cladding, as it was found to be an important variable not previously considered. However, low mass participation ratios coupled with the stiffness provided by the secondary framing put the use of the equivalent lateral force procedure into question.

Towards a Better Understanding of the Fundamental Period of Metal Building Systems

Santiago Bertero

(GENERAL AUDIENCE ABSTRACT)

When designing buildings for earthquake loads it is necessary to know their dynamic properties in order to define the equivalent forces that must be applied. Building codes provide predictive equations that were obtained empirically for typical mid-rise construction. Metal buildings do not fall within the range of buildings tested for their development, and so a new equation was proposed for them based on a database of planar models. However, previous tests implied that this equation was predicting larger periods than those obtained experimentally.

In this work, further tests were carried out during different stages of construction to evaluate how non-structural elements could affect the behavior. Models were also created for each building in order to determine if the approach used to develop the metal building database was adequate for estimating the period.

The results from tests showed that, unlike other single-story buildings, non-structural components seem to have negligible effect on the structural behavior, and the modeling assumptions within the database were validated. Further analysis showed that the type of cladding (concrete or metal sheeting) had a large influence on the properties of metal buildings. In consequence, a new set of predictive equations is proposed that takes this into account.

Acknowledgments

First of all, I would like to thank my advisor Dr. Rodrigo Sarlo for trusting me as an incoming student to work for him in different projects from which I can take a lot from. His support is deeply appreciated, both from an academic and (especially) personal standpoint. I would also like to extend my gratitude to my committee members, Dr. Finley A. Charney and Dr. Matt R. Eatherton, whose feedback and commentary I believe made for a better end product. I learned a lot not only from trying to answer their inquiries, but also from the knowledge they shared in the classroom and in casual conversation when available.

I would also like to thank the Metal Building Manufacturers Association for sponsoring this research, and Igor Marinovic and Dr. W. Lee Shoemaker for their guidance. I would also like to thank the industry people who provided vital information or access to the tested buildings: Dustin Cole from Chief Buildings, Matt Bartels and Justin Kestler from Bartels Construction Solutions, Herman Baber from Clark Nexsen Construction Services and Shane West from TKS Contracting.

The experimental portion of this thesis would not have been possible without the help of my fellow labmates who took time out of their own busy student lives to lend a hand: Tasha Vipond, Hesam Soleimani, Amin Moghadam and Alan Smith.

On a personal note, I'd like to thank my friend Zayeem Zaman for helping me settle in Blacksburg and having my back at all times. My family's support, now at a distance, is also invaluable to me and I can't wait to be back close to them.

Finally, I'd like to thank Universidad de Buenos Aires and Argentina's public education system for making me the engineer I was when I came to Blacksburg, and Virginia Tech for turning me into the engineer I am now.

Contents

- List of Figures** **xi**

- List of Tables** **xviii**

- 1 Introduction** **1**
 - 1.1 Background and Motivation 1
 - 1.2 Thesis Scope and Organization 4

- 2 Literature Review** **6**
 - 2.1 Seismic Design Principles and its Application to Metal Buildings 6
 - 2.1.1 Defining the Seismic Demand 6
 - 2.1.2 Estimating the Fundamental Period 11
 - 2.1.3 Force distribution along its members 19
 - 2.1.4 Assumptions Made in Metal Building Design 23
 - 2.2 Structural modelling of the main lateral resisting system 24
 - 2.2.1 Modeling of web tapered elements 25
 - 2.2.2 Shear Deformations 26
 - 2.2.3 Panel Zone Deformations 27
 - 2.2.4 Base Fixity 29

2.2.5	Discussion	31
2.3	Modeling of steel sheeting	34
2.3.1	Developments in the U.S.	35
2.3.2	European approach	40
2.3.3	Limitations of current empirical equations	44
2.4	Experimental Testing for Period Extraction	47
3	Methodology	51
3.1	Introduction	51
3.2	Operational Modal Analysis	52
3.2.1	Background and Justification	52
3.2.2	State-Space Representation and Subspace Identification	54
3.2.3	Process Automation	58
3.3	Testing Procedure	60
3.3.1	Equipment	61
3.3.2	Sensor Placement	62
3.3.3	Data gathering, pre and post-processing	65
3.4	3D Modeling of metal buildings	66
3.4.1	Main framing	66
3.4.2	Secondary framing and bracing	69

3.4.3	Cladding	71
3.4.4	Other considerations	73
3.5	Tested Buildings	74
3.5.1	Building VA-1	75
3.5.2	Building VA-2	77
3.5.3	Building WV-1	78
3.5.4	Building WV-2	79
3.5.5	Building NC-1	80
3.5.6	Building NC-2	82
3.5.7	Building NC-3	83
3.5.8	Summary	84
4	Results	87
4.1	Building VA-1	88
4.1.1	Bare Frame Test	88
4.1.2	Completed Building Test	97
4.2	Building NC-2	102
4.2.1	Bare Frame Test	102
4.2.2	Test with Walls installed	106
4.2.3	Test on completed building	109

4.3	Building NC-1	111
4.3.1	Test on Bare Frame	111
4.3.2	Test on fully clad building	116
4.4	Building VA-2	120
4.4.1	Test with roof installed	120
4.4.2	Test on fully clad building	123
4.5	Building WV-2	127
4.6	Building WV-1	130
4.7	Building NC-3	134
4.8	Discussion	136
4.8.1	Summary	136
4.8.2	2D Model analysis of metal buildings	139
4.8.3	Modal mass participation factor	141
4.8.4	Influence of purlins and flexible diaphragm assumption	143
4.8.5	Revisiting the VTH and BBTC buildings	148
5	Evaluation of the Smith and Uang Equation	151
5.1	Fundamental period comparison with best guess weight	151
5.2	Fundamental period comparison with design weight	155
5.3	Comparison between the synthetic data set and the tested buildings	158

5.3.1	Building classification	158
5.3.2	Differences with building classification	160
5.3.3	Differences with loading conditions	161
5.3.4	Geometric parameters	163
5.4	Summary and Discussion	165
6	Development of new period prediction formulas	169
6.1	Introduction	169
6.2	Rational analysis for determining the equation type	170
6.3	Linear regression analysis	173
6.4	Proposed lower-bound equations	176
6.5	Equation performance in tested buildings	180
7	Observations on the application of the Equivalent Lateral Force Method	181
7.1	Introdcution	181
7.2	Simplified N-DOF model of a metal building	182
7.3	Base shear distribution among frames	185
8	Conclusions and Future Work	189
8.1	Summary	189
8.2	Main Conclusions	193
8.3	Future Work	194

Bibliography	196
Appendix A Plan and Elevation Drawings for Tested buildings	203
Appendix B Summary of Tests on Fully-Clad Metal Buildings to Date	210

List of Figures

1.1	Typical components of a metal building system (Newman, 2015)	2
2.1	Generic Design Response Spectrum (ASCE/SEI 7-16, 2017)	9
2.2	Comparison of periods of steel moment frames from records for low-to-medium rise buildings (Kim et al., 2009)	12
2.3	Building period for one story building with varying wall and diaphragm stiffness, and mass distribution (Fischer and Schafer, 2021)	14
2.4	Comparison between Smith and Uang formula and ASCE-7 formula for a given mean roof height (Kumar et al., 2020)	16
2.5	Summary of the results of the experimental tests carried out on metal buildings by Kumar et al. (Kumar et al., 2020)	17
2.6	Example of loading on a frame for illustrative purposes, taken from Smith and Uang (Smith and Uang, 2013)	20
2.7	Finite-element model for computing diaphragm flexibility (Charney et al., 2020)	22
2.8	Panel Zone Model Comparison (Smith and Uang, 2013)	28
2.9	Modeling of Column-to-Base Connection when Base Plate is Flexible (Bajwa et al., 2010)	30
2.10	Diaphragm distortion for shear strength and shear stiffness calculations (Avcı et al., 2016)	36

2.11	Profile of the Strukturoc system (Strukturoc, Inc.)	45
2.12	Schematic view of instrumentation layout (Wei et al., 2020)	46
3.1	Example Power Spectral Density, obtained via ambient vibrations, showing peaks at $2Hz$ and $2.5Hz$: the first two natural frequencies of the structure (Kumar et al., 2020).	54
3.2	Example Stabilization diagram.	59
3.3	Typical instrumentation of a frame.	63
3.4	Example instrumentation scheme for metal building testing. In orange, sensor locations for the first measurement. In blue, sensor locations for the second measurement.	64
3.5	Typical 3D model used for analysis of a metal building in its operative stage.	67
3.6	Main frame modelling. Left: 2D View of extruded frame. Right: close up view of the beam-column connection.	67
3.7	Isometric view showing the connection of secondary framing elements to the main frame.	70
3.8	Isometric view showing the introduction of cladding as thin shell elements	72
3.9	Building VA-1 after completion of the cladding installation.	76
3.10	Building VA-1 during the the first test on September 24, 2021.	76
3.11	Building VA-2 across different tests.	78
3.12	Outside view of Building WV-1	78
3.13	Interior of building WV-1	79

3.14	Building WV-2 at the time of testing.	80
3.15	Building NC-1 during the second (Top) and first (Bottom) tests.	81
3.16	Building NC-2 during different stages of construction.	83
3.17	Building NC-3	84
4.1	Sensor locations for Test 1 in Building VA-1	88
4.2	Collected data for the first test in Building VA-1	89
4.3	Spectrogram of the acceleration data recorded by sensor 3 on the first test in Building VA-1	90
4.4	Stabilization diagram for test 1 in Building VA-1. Blue dots represent stable poles. Red crosses represent unstable poles. and small blue circles represent unstable modes in terms of damping. The selected modes are circled.	91
4.5	Final clusters from test 1 in Building VA-1	92
4.6	Experimental modes from test 1 in Building VA-1	93
4.7	SAP2000 model of building VA-1 for test 1	94
4.8	Mode prediction from SAP2000 for test 1 in Building VA-1	95
4.9	crossMAC for building VA-1 – test 1	97
4.10	Sensor locations for Test 2 in Building VA-1	98
4.11	Collected data for the second test in Building VA-1	99
4.12	First mode from test 2 in Building VA-1	99
4.13	SAP2000 model of building VA-1 for test 2	101

4.14	Mode prediction from SAP2000 for test 2 in Building VA-1	101
4.15	Sensor locations for Test 1 in Building NC-2. In orange: measurement 1. In blue: measurement 2.	103
4.16	Collected data for the second measurement of the first test in Building NC-2	103
4.17	Experimental modes from test 1 in Building NC-2	104
4.18	SAP2000 model of building NC-2 for test 1	105
4.19	Mode prediction from SAP2000 for test 1 in Building NC-2	105
4.20	crossMAC for building NC-2 – test 1	106
4.21	Collected data for the second measurement of the second test in Building NC-2	107
4.22	Experimental modes from test 2 in Building NC-2	108
4.23	Mode prediction from SAP2000 for test 2 in Building NC-2	108
4.24	crossMAC for building NC-2 – test 2	109
4.25	Collected data for the second measurement of the third test in Building NC-2	110
4.26	First mode from test 3 in Building NC-2. Left: experimental. Right: predicted	111
4.27	Sensor locations for Test 1 in Building NC-1. In orange: measurement 1. In blue, measurement 2.	112
4.28	Collected data for both measurements of the first test in Building NC-1 . . .	113
4.29	Experimental modes from test 1 in Building NC-1	114
4.30	Mode prediction from SAP2000 for test 1 in Building NC-1	115
4.31	crossMAC for building NC-1 – test 1	116

4.32	Acceleration record for sensor 5 during measurement 1, test 2 for building NC-1	117
4.33	SAP2000 model of building NC-1 for test 2	118
4.34	Mode prediction from SAP2000 for test 2 in Building NC-1	119
4.35	Sensor locations for Test 1 in Building VA-2. In orange: measurement 1. In blue: measurement 2.	121
4.36	Collected data for the second measurement of the first test in Building VA-2	121
4.37	SAP2000 model of building VA-2 for test 1	122
4.38	Mode prediction from SAP2000 for test 1 in Building VA-2	123
4.39	Sensor locations for Test 2 in Building VA-2. In orange: measurement 1. In blue: measurement 2.	124
4.40	Collected data for the second measurement of the first test in Building VA-2	124
4.41	Experimental modes from test 2 in Building VA-2	125
4.42	Mode prediction from SAP2000 for test 2 in Building VA-2	126
4.43	crossMAC for building VA-2 – test 2	126
4.44	Sensor locations for the test in Building WV-2. In orange: measurement 1. In blue: measurement 2.	127
4.45	Collected data for the first measurement during the test in Building WV-2 .	128
4.46	Experimental modes from the test in Building WV-2	128
4.47	Analytical model of building WV-2	130
4.48	Experimental modes from the test in Building WV-1	131

4.49	Analytical model of building WV-1	132
4.50	crossMAC for building WV-1	133
4.51	Collected data during the test in Building NC-3	135
4.52	Comparison between the empirical and analytical first mode for building NC-3	135
4.53	Close up view of the column bases for two different metal buildings	138
4.54	Deflections on Building NC-2 to a point load applied at the rafter level of frame line 5.	144
4.55	First mode of building NC-2 seen from above.	145
4.56	Deflections due to a surface unit load applied to the roof diaphragm.	146
4.57	Acceleration data from middle interior frame of the VTH building during the free vibration test.	149
5.1	Comparison between the different period estimates (relative to T_{test})	153
5.2	Ratio between model and predicted period based on different classifiers for the Smith and Uang data set.	160
5.3	Ratio between model and predicted period based on loading conditions	162
5.4	Scatter plot showing the geometric properties of different buildings.	164
6.1	Simplified analysis of a single-story moment frame	172
6.2	Performance of proposed equation for metal buildings with metal panels using Smith and Uang's data set	177

6.3	Performance of proposed equation for metal buildings with concrete hardwalls using Smith and Uang's data set	178
6.4	Performance of the alternative proposal for metal buildings with concrete hardwalls using Smith and Uang's data set	179
7.1	Generic example of a simple N-DOF model for 3D analysis of metal buildings.	183
7.2	First three modes for simplified WV-2 model.	186
A.1	Plan and elevation drawings for Building VA-1.	203
A.2	Plan and elevation drawings for Building VA-2.	204
A.3	Plan and elevation drawings for Building WV-1.	205
A.4	Plan and elevation drawings for Building WV-2.	206
A.5	Plan and elevation drawings for Building NC-1.	207
A.6	Plan and elevation drawings for Building NC-2.	208
A.7	Plan and elevation drawings for Building NC-3.	209

List of Tables

3.1	Summary of properties of the buildings tested – design parameters	85
3.2	Summary of properties of the buildings tested - structural classification	86
4.1	Summary of fundamental period on bare frame structures	136
4.2	Comparison between tests for buildings in which applied mass stayed constant	137
4.3	Summary of tests done on fully clad buildings	138
4.4	Summary of tests done on fully clad buildings	140
4.5	Modal mass participation ratios for the first mode	142
4.6	Summary of tests done on fully clad buildings	148
5.1	Fundamental period of tested buildings using different methods	152
5.2	Fundamental period of tested buildings using different methods	156
5.3	Classification of tested metal buildings	159
6.1	Regression models for metal buildings with metal cladding in high seismic areas.	175
6.2	Regression models for metal buildings with concrete hardwalls in high seismic areas.	176
6.3	Fundamental period of tested buildings using the new proposed equations	180
7.1	Modal properties of simplified proxy of building WV-2	186

7.2	Distribution of base shear among frames based on RSA and ELF, in units of <i>kip</i>	187
B.1	Summary of properties of the buildings tested to date - structural classification	210
B.2	Summary of properties of the buildings tested – design parameters and mea- sured period	211

Chapter 1

Introduction

1.1 Background and Motivation

Metal buildings are quite popular in America, accounting for over 1,000,000 *tons* of steel yearly for low-rise commercial construction. A growing industry as well, in 2020 there was a sharp increase in sales of buildings in excess of 150,000 *ft*² due to the new demand for storage warehouses for e-commerce (MBMA, 2020). These systems, mostly defined by the use of web-tapered, built-up steel moment frames for the main lateral load resisting system and cold-formed steel sections for secondary elements (Figure 1.1), provide ample floor plan flexibility to the building owner as clear spans can extend over 100 *ft* (MBMA, 2019a). This, coupled with their fast shipment and erection times makes them a cost-effective solution, reaching 65% of all new low-rise construction in 1995 (Newman, 2015). These buildings can be classified as Clear Span when the interior frames span the whole width of the building (Figure 1.1), or as Modular when interior gravity columns (hinged on both ends) are present. Still referred to as *pre-engineered buildings* due to the use of standard designs in the 60's, they are now however custom-designed and optimized for each project.

A non-trivial portion of the design process is ensuring the structure will perform adequately against seismic events. Historically, metal buildings have shown good performance due to their light weight and flexible nature, an exception being those built with hardwalls (Langley, 2018). The moment frames used in metal buildings differ from those seen in conventional

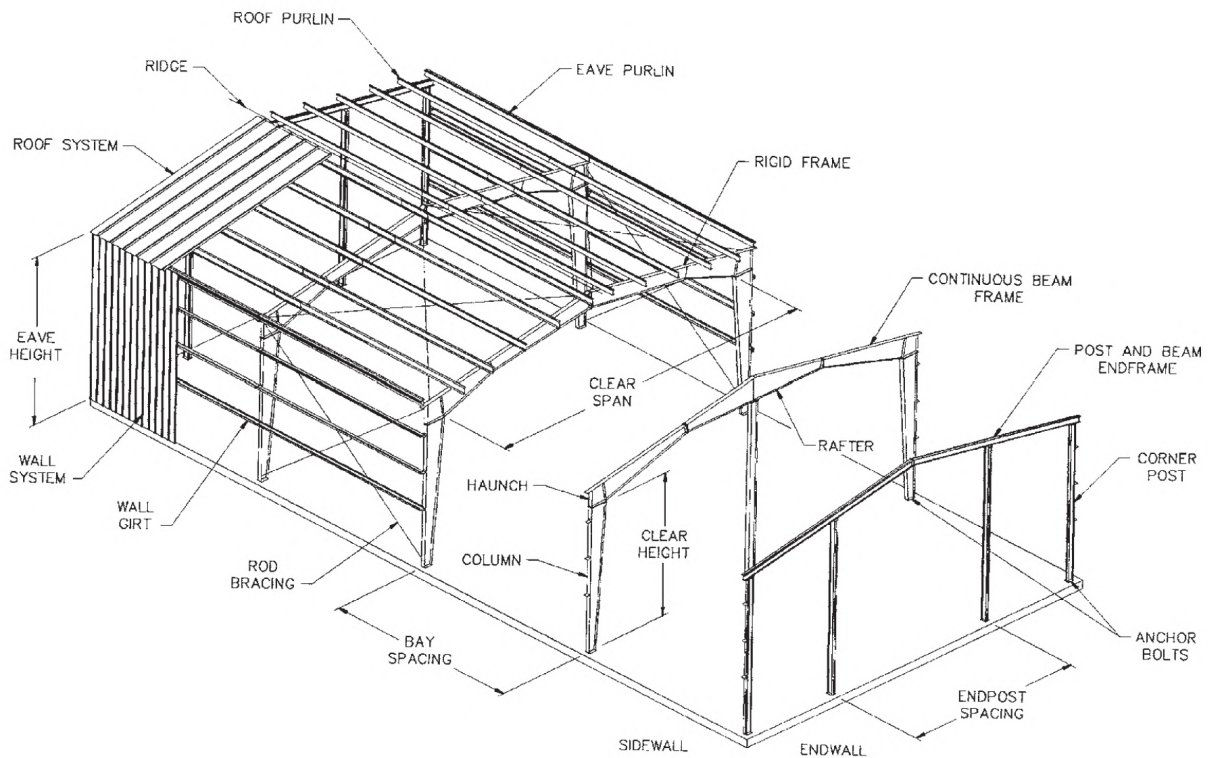


Figure 1.1: Typical components of a metal building system (Newman, 2015)

mid-rise buildings. Since they consist of tapered beams and columns with bolted end-plate connections, most of the research done following the 1994 Northridge earthquake and the subsequent code changes (such as height limits for ordinary moment frames in high seismic areas) may not fully apply to them. For example, most of the damage seen in Northridge was related to the brittle failure of the welded beam-column connection, which is not present in metal buildings. In fact, experimental testing has shown that the ductile mechanism of gabled frames is a three-hinged arch due to alternating lateral torsional buckling at the rafter level, unlike the conventional flexural hinge (Smith, 2013). The Metal Building Manufacturers Association (MBMA) has in response funded different research projects specific to the structural systems commonly used by its members. Among them, work by the University of California, San Diego (UCSD) led to the proposal of a new formula to estimate the period of vibration of metal buildings (Smith and Uang, 2013).

The natural period of a structure is of great importance for seismic design as the seismic load is dynamic in nature. Most buildings are usually designed using the equivalent lateral force (ELF) method, which converts the seismic effects (forces due to displacements) into equivalent applied forces. Generally speaking, the more flexible a structure is (that is, the longer the period if the mass is kept constant), the lower the design forces will be.

The proposed equation by Smith and Uang was developed by doing a regression analysis of 192 analytical 2D-models of an interior bay of a given metal building designed according to current industry practices (Smith and Uang, 2013). This equation, however, was shown to overestimate the period when compared to field experiments carried out by Virginia Tech (Kumar et al., 2020). In consequence, the use of this equation could underestimate the design forces and result in unconservative designs.

The reasons for the discrepancy were not clear, though some possible explanations were given. First of all, Smith and Uang's analytical models assumed the columns were ideally pinned at the base, though in reality the connection always has some degree of fixity (Bajwa, 2010; Verma, 2012). Beyond that, constructed buildings include partitions, appendices and non-structural elements (such as metal sheeting and diaphragms) that are attached to the main structure, affecting its stiffness. These effects were not captured by the models used.

With this in mind, it was proposed to do a set of field experiments – measuring the dynamic properties of metal buildings during different construction stages – in order to better understand and quantify the sources of such difference with the proposed formula. This project, funded by the MBMA and carried out at Virginia Tech results in the masters thesis here presented.

1.2 Thesis Scope and Organization

The main purpose of this thesis is to have a better understanding of how metal buildings perform in service in terms of their fundamental period, and explain and quantify possible sources of divergence between analytical models and test data. The agreement of predictive equations with said results is also studied. In order to accomplish this, a set of experimental tests was carried out at different stages of construction. For each construction stage, a full 3D-model of the as-built structure was developed and calibrated in order to reduce uncertainty in a sequential manner, including the effect of non-structural elements such as the endwalls and roof sheeting if required.

Then, the use of 2D-models for the purpose of evaluating the natural period of metal building systems with standing seam roofs (SSR) was evaluated, to potentially validate the analysis that led to the development of Smith and Uang's prediction formula. Finally, an analysis of the goodness of fit of the formula itself was carried out in order to provide recommendations on its applicability or how to improve its accuracy otherwise. The effects of the different period formulas on the design of these buildings is out of the scope of this project. Similarly, the adequacy of ELF will not be covered in detail, though some potential issues will be raised and/or addressed in preliminary fashion.

The thesis is organized as follows:

- Chapters 1 and 2: Introduction and literature review, covering different aspects of metal building systems, seismic design; and structural analysis and modeling
- Chapter 3: Methodology, detailing the theoretical and practical aspects of vibration measuring and system identification; as well as a description of the tested buildings and the assumptions made for 3D modeling

- Chapter 4: Results of experimental work and validation of different modeling approaches for metal building design
- Chapter 5: Evaluation of Smith and Uang's formula in light of new test data, looking at both the assumptions made and the overall accuracy in the tested parameter range.
- Chapter 6: Development of new predictive equations for metal buildings based on the cladding type
- Chapter 7: A preliminary look at some potential shortcomings of the equivalent lateral force procedure in light of the observed behavior in experimental tests
- Chapter 8: Conclusions, recommendations and future work

Chapter 2

Literature Review

2.1 Seismic Design Principles and its Application to Metal Buildings

2.1.1 Defining the Seismic Demand

Design Philosophy

Along with gravity and wind loads, buildings are generally designed to withstand the effect of ground motions, though the latter is dependent on the location of the structure. Given that the design earthquake can be quite large in magnitude, it becomes economically unfeasible to ensure that the building remains elastic during these events. As a result, the design philosophy has evolved into allowing energy dissipation through inelastic yielding of some of the structural components. This in turn means that some damage is allowed and expected while still avoiding collapse.

The way the current version of ASCE-7 ([ASCE/SEI 7-16, 2017](#)) achieves this is by computing the loads assuming linear behavior, and then reduce them by a response modification coefficient R for the design of the ductile system. The value of R will depend on the degree of inelasticity the chosen structural system can reliably accommodate. For example, designing a structure to remain elastic would imply the use of $R = 1$. Meanwhile, an ordinary steel

moment frame can be designed with value of $R = 3.5$ which reduces the design loads. However, prescriptive requirements need to be followed such as connection detailing requirements and drift limits if applicable.

Describing The Design Earthquake

In any case, defining the design earthquake is the first step in the process. This will depend on the location of the building and the soil characteristics (described by the site class as per Chapter 20 of ASCE-7). The seismic hazard is not in itself a load, but an unknown ground motion or set of possible ground motions. However, its properties can be effectively summarized by the response it would produce on a linear-elastic, single degree-of-freedom (1-DOF) system with what is called a response spectrum (Chopra, 2017). The response spectrum shows the maximum elastic force (or a proxy of it) a 1-DOF system would be subjected to by the earthquake given its natural period. This force is referred to as the base shear. For a 1-DOF system with stiffness k and mass m , the base shear $\max\{F_k\}$ would be

$$\max\{F_k\} = k \max\{x(t)\} = k S_d \quad (2.1)$$

where $x(t)$ is the displacement response of the structure to the ground motion, which is a function of its natural period T and the damping ratio ζ ; and S_d is then known as the spectral displacement. Knowing that

$$T = 2\pi\sqrt{\frac{m}{k}} \quad (2.2)$$

then Equation 2.1 can be rewritten as

$$\max\{F_k\} = k S_d = m \left(\frac{2\pi}{T}\right)^2 S_d = m S_a \quad (2.3)$$

with S_a being the pseudo-acceleration or spectral acceleration, and is just as before a function of the period and damping ratio for a given ground motion. The term “pseudo-acceleration” is frequently used since the value is actually associated with the maximum displacement and not the maximum acceleration, despite the units. The main reason for writing the base shear as function of the mass instead of the stiffness lies in the fact that it is more common to have a better estimate of the weight of the structure than its stiffness before the sections are finalized and does not require previous structural analysis. It is also more intuitive to describe the seismic load as an inertial force. This doesn’t mean that the stiffness doesn’t play a role, as it’s embedded in the value of S_a which depends on the natural period.

Also, if the spectral acceleration is written in units of g , then the mass can be written in units of kip/g to obtain the base shear in units of force. As a result, instead of referring to the mass the concept of seismic weight W (in kip) is used instead.

The function $S_a(T)$ as defined in ASCE 7-16 can be seen in Figure 2.1. This design spectrum is based on doing a uniform risk analysis on 2 periods (0.2 and 1s) and assuming constant acceleration, constant velocity or constant displacement depending on the period range. The value associated with 0.2s or “short periods” is effectively the plateau S_{DS} where constant acceleration is assumed. the value associated with a 1s period, S_{D1} , is assumed to be within the constant velocity portion of the spectrum, and so in its vicinity the spectrum is inversely proportional to the natural period T . Connecting both lines the period at which the plateau ends, T_s , can be found. The value of T_s is typically around 0.5s.

Interestingly, due to their short height, metal buildings tend to fall in the plateau range

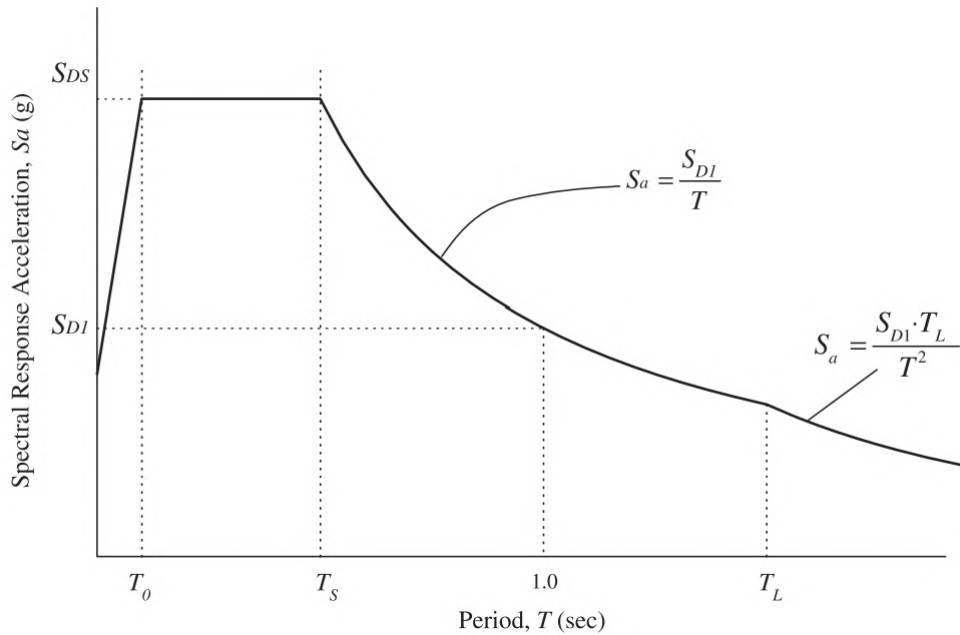


Figure 2.1: Generic Design Response Spectrum ([ASCE/SEI 7-16, 2017](#))

when using ASCE-7's period equation (which will be discussed later), as it results in values in the order of $0.4s$. However, frame analysis would put a typical metal building in the constant velocity range (periods larger than $0.5s$). As a result, as T gets longer S_a becomes smaller, and so the forces the structure would need to resist get smaller as well. Since metal buildings are heavily optimized for economy, this change in loads due to the period used in design could heavily impact fabrication costs.

The Equivalent Lateral Force Method

The design spectrum still only describes the hazard and there are different ways to translate it into seismic demand. For metal buildings, given their relatively simple floor plans and structural behavior, the equivalent lateral force (covered in ASCE-7 Section 12.8) procedure, ELF, is the method of choice, which follows the result from Equation 2.3 for 1-DOF systems.

Assuming we can know the natural period of the building the value of S_a can be obtained, and then the base shear V can be computed as

$$V = W \frac{I_e}{R} S_a \quad (2.4)$$

where I_e is an importance factor according to ASCE-7 Table 1.5-2 and is a function of the building purpose. Note, then, that the force obtained through ELF builds upon the idea that the structure responds exclusively in its first mode of vibration, which is an adequate assumption when the mass participation ratio of the first mode is high enough. For mid-rise buildings this is typically true. However, past studies have put into question the validity of this assumption for Metal Buildings. When looking at the frame itself, Smith and Uang found the mass participation ratio for the first mode could drop to as low as 40% when the ratio between the span and the height of the main frame was higher than 3 (Smith and Uang, 2013). This is because as the span gets longer, the vertical movement of the rafter becomes more important. Meanwhile, Langley and Marshal found that – when modelling metal buildings with hardwalls – the mass participation ratio for the first mode was also below 50% with “hundreds” of modes required to reach even 90% (Langley and Marshall, 2017). The main reason for this is that an important portion of the mass is concentrated in the hardwalls, which are essentially infinitely stiff compared to the moment frames (Langley, 2016). If the diaphragm is assumed to be fully flexible, the connection between the main frames and the hardwall is done through the purlins and girts which are quite flexible, and so the first mode shapes are related to the movement of individual frames.

2.1.2 Estimating the Fundamental Period

Equations in ASCE-7

Going back to Equation 2.4, in order to obtain the base shear V it is necessary to know the fundamental period of the building, since that defines the spectral acceleration. This is why ASCE-7 provides equations in ASCE-7 Section 12.8.2.1 to estimate the fundamental period of buildings. As per ASCE-7 Equation 12.8-7, the approximate Fundamental Period T_a can be found as

$$T_a = C_t h_n^x \quad (2.5)$$

where h_n is the mean roof height, and C_t and x are regression parameters that depend on the structural system and are determined from ASCE-7 Table 12.8-2.

This equation was the result of research done by Goel and Chopra, where they measured the period of vibration of moment frame buildings, 27 built with reinforced concrete and 42 with structural steel (Goel and Chopra, 1997). For the latter, these consisted of typical multi-story buildings with prismatic rolled shapes for the beams and columns. The results can be seen in red (“from literature”) in Figure 2.2, along with the lower and upper bound estimates provided in ASCE-7. The height of these buildings ranged from 2 stories (30ft) to 60 (843.2ft). The period was measured during different earthquakes in California, such as Northridge (1994), San Fernando (1971) and Loma Prieta (1989). During the 1994 Northridge Earthquake, strong ground shaking above 0.15g was measured, and for steel moment frames it was found that the level of shaking had little influence in the period as the buildings still behaved in elastic fashion. Equation 2.5 is meant to be a lower-bound estimate of the natural period so that approximately 15% of the buildings land below the curve.

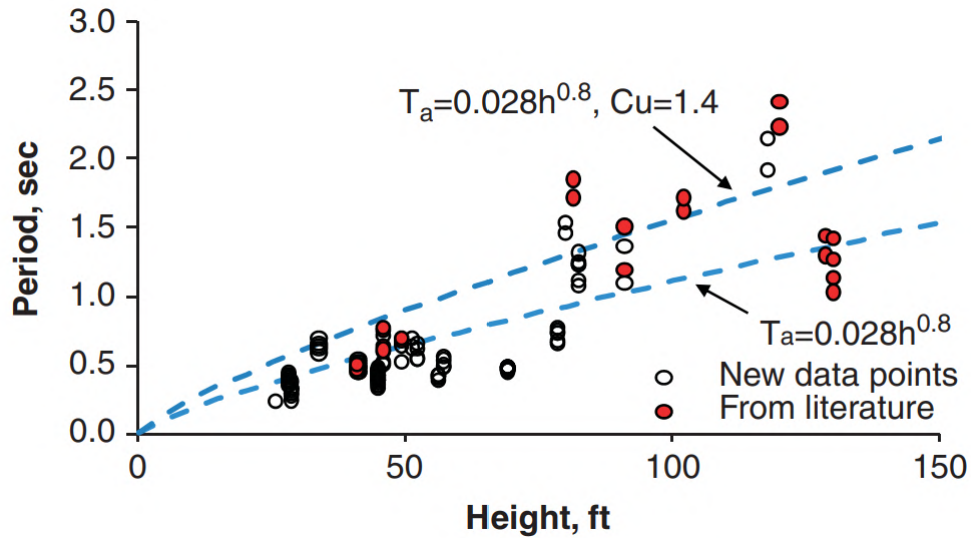


Figure 2.2: Comparison of periods of steel moment frames from records for low-to-medium rise buildings (Kim et al., 2009)

Alternatively, the code allows the computation of the period of vibration via structural analysis in lieu of using the approximate equation. However, generally speaking the longer the period, the lower the Spectral Acceleration will be. In turn, ASCE-7 sets an upper limit on the the computed period in order to prevent unconservative designs due to unreasonable assumptions in modeling, given that a lower Spectral Acceleration results in a smaller design base shear. This upper limit is obtained by multiplying the lower-bound prediction T_a by a factor C_u which is in essence an upper-bound estimate of the period done with the same database (See Figure 2.2).

Looking closely at Figure 2.2, it is noticeable how there is significant scatter for short buildings, implying Equation 2.5 is a poor fit. Scatter is also present for taller buildings, though more important here is that they results do not fall between the lower and upper bounds. This is because the only parameter currently included in the period equation is height, but as buildings become shorter other features may be better at predicting the frame stiffness. Beyond that, the data set is limited when it comes to buildings below $50ft$ and there are

no buildings below 25ft, which is a common height for metal buildings. Also, the equation tends to overestimate the period for shorter buildings, at least those included in the database. Bear in mind the equation was developed for multi-story buildings, far removed from the single-story metal buildings that have not only vastly different loads and mass, but different structural configurations as well. Different attempts have been made to develop an equation that better predicts the period of vibration of single-story buildings in general and metal buildings in particular, which will be covered below.

Alternative equations for single-story buildings

Lamarche et al. developed an equation for single-story buildings with steel concentrically-braced frames on their exterior walls, based on regression analysis of 22 measured buildings using ambient vibration data (Lamarche et al., 2009). These buildings, of course, differ significantly from both the buildings included in Goel and Chopra (Goel and Chopra, 1997) and also with typical metal buildings, where the main resisting system is web-tapered built-up moment frames in the interior bays. However, some interesting conclusions can be taken from this work. First of all, it showed that including new parameters such as the distance between lateral load resisting systems (or bay spacing) improved the fit of the predictive equation significantly for single-story buildings. The proposed formula is

$$T_a = 0.0035 (D_{neff} h_n)^{0.7} \quad (2.6)$$

where D_{neff} is the effective distance between lateral systems and h_n is the same as in ASCE-7. Both dimensions must be in meters. The inclusion of the bay spacing is because the roof diaphragm is flexible and produces a lengthening effect on the fundamental period compared to what would be obtained just by considering the stiffness of the lateral load resisting system.

The lengthening effect of diaphragm flexibility in the natural period of single-story buildings was further studied by Fischer and Schafer, where it can be seen that the natural period of the building T_b converges to the period of the isolated walls serving as the lateral force resisting system, T_w , when the diaphragm is rigid (Fischer and Schafer, 2021). In addition, it can be seen that the mode shape is governed by the deformation of the walls. Similarly, T_b converges to the period of the diaphragm in isolation, T_d , when it becomes fully flexible, with the mode shape being governed by the deformation in the diaphragm. Meanwhile, when the period of the diaphragm and the walls are similar, a significant lengthening effect can be seen, which is a function of the diaphragm mass (Figure 2.3).

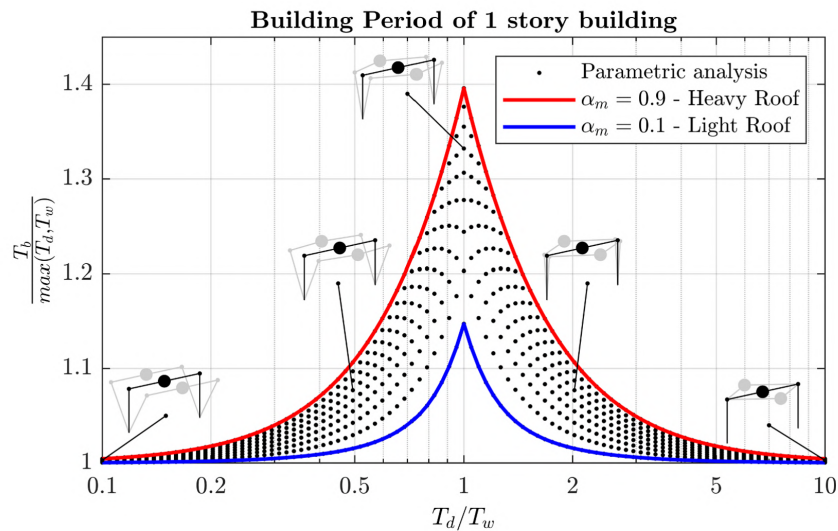


Figure 2.3: Building period for one story building with varying wall and diaphragm stiffness, and mass distribution (Fischer and Schafer, 2021)

Second, data showed that non-structural components had a significant effect on the measured period. Tests were carried out both during construction and in service, and a decrease in period of up to 38% was observed, implying that non-structural walls were adding significant stiffness to the buildings. Tremblay and Rodgers modeled these structures considering only the structural elements and found their predicted periods to be also much longer than those measured in the field once the cladding was installed, even though it provided a good match

during construction ([Tremblay and Rogers, 2011](#)). The authors argue that the discrepancy can be attributed to the low levels of vibration during testing, which is orders of magnitude lower than the ones the structure will be subjected to during an earthquake event and was captured by Goel and Chopra, putting into question the use of ambient vibrations for period estimation. However, it must be mentioned that their models did not include the effect of non-structural components for its period prediction, which has been shown to underestimate the stiffness of structures even for design-level wind loads ([Bajwa, 2010](#); [Bajwa et al., 2010](#); [Gryniewicz et al., 2021](#); [Kim et al., 2009](#)). In any case, looking specifically at roof diaphragms, experimental tests on roof specimens by Rogers and Tremblay show that by increasing the amplitude of vibration, the natural period of the diaphragm quickly reduces quite significantly, most probably due to overcoming internal friction at the connection level, though the repercussions of this were not explored ([Rogers and Tremblay, 2010](#)).

It is also worth pointing out that the dataset from ([Rogers and Tremblay, 2010](#); [Tremblay and Rogers, 2011](#)) had untopped Wide-Rib steel deck for roofing and not standing-seam roofing, the former being known to provide diaphragm action while the latter is assumed not to. This, in turn, means that the results from their work cannot be extrapolated to metal building systems, neither in terms of the effects of cladding and non-structural elements, nor with respect to the natural period itself.

Proposed equation for metal buildings

Compared to the previous equations that were developed based on experimental testing, Smith and Uang derived an expression specific for metal buildings by doing a regression on the analytical computed period of over 100 buildings ([Smith and Uang, 2013](#)). There is precedent to using analytical modeling for the purpose of developing a period equation. For example, the period estimation formula for steel braced-frames within the National Building

Code of Canada (NBC 2015, 2015) was developed based an analytical study by Tremblay (Tremblay, 2005).

For metal buildings, the proposed equation by Smith and Uang was a function of the seismic weight W in *kips*, the span-to-height ratio α and the mean roof height of the building h_n in *inches* given by

$$T_a = \begin{cases} 0.058 (Wh_n)^{0.3} & \alpha \leq 3 \\ 1.58W^{0.16}/\alpha & \alpha > 3 \end{cases} \quad (2.7)$$

As mentioned in the previous paragraph, α is the span-to-height ratio, taken as the maximum ratio between the width of each bay and its mean roof height, which may differ in modular frames. For clear span frames, α becomes the ratio between the main span and h_n .

Figure 2.4 shows how the natural period changes with the span-to-height ratio and the seismic weight for a given mean roof height. First, it can be seen that the ASCE-7 equation stays constant as it does not include any other parameter beyond mean roof height, while the Smith and Uang equation does show variation. More importantly, the latter formula is discontinuous at $\alpha = 3$, which at first glance is unintuitive and would need further revision.

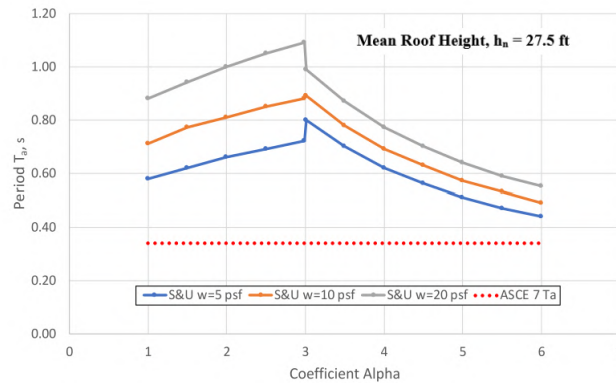


Figure 2.4: Comparison between Smith and Uang formula and ASCE-7 formula for a given mean roof height (Kumar et al., 2020)

However, when compared to Figure 2.2, available test data for low-rise steel moment frame buildings show that the ASCE-7 equation may overestimate the periods at heights below 100ft. Meanwhile, the proposed equation has even longer estimated periods than current provisions. As mentioned before, metal buildings and typical residential moment frame buildings are quite different, and so an experimental validation was carried out by Kumar et al. (Kumar et al., 2020). The fundamental period of 6 metal buildings were obtained via ambient testing, and the results were consistently shorter than those predicted by the Smith and Uang equation and at times even the ASCE-7 formula. In fact, some buildings had a period 3 times shorter than those predicted. The results are summarized in Figure 2.5.

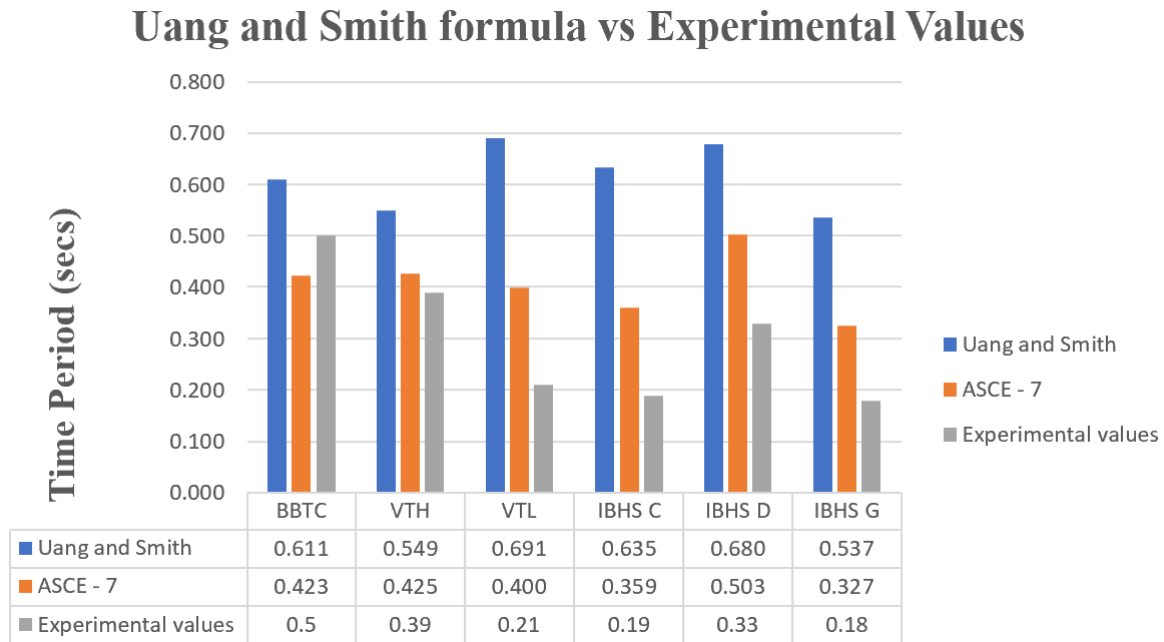


Figure 2.5: Summary of the results of the experimental tests carried out on metal buildings by Kumar et al. (Kumar et al., 2020)

In order to understand possible sources of such discrepancy, the analytical models used by Smith and Uang and their assumptions should be examined more closely. First, the model consisted of an interior 2D-frame, with the building mass assigned according to its tributary areas. This is a common assumption done for the design of metal buildings, as

roof diaphragms of all types are usually treated as flexible – carrying no in-plane stiffness – while neglecting the added stiffness of girts and purlins (MBMA, 2019b). Work by Bajwa et al., who applied point loads one frame at a time in a metal building showed that the frame stiffness was being affected by the constraint added by the secondary framing (Bajwa et al., 2010). This was corroborated by developing a 3D-model of the structure, which provided much better predictions than the 2D-Frame analysis (Bajwa, 2010).

Also, the flexible diaphragm assumption makes it so that the endwalls or endframes do not affect the period of the building at large, as every bay is assumed to work independently.

As for the main frame model itself, the beams and columns were modeled as non-prismatic elements, obtaining the element stiffness matrix by inverting the flexibility matrix (including shear deformations) and lumping masses at nodes distributed along the elements. Despite the low weight of metal buildings, both $P - \Delta$ and $P - \delta$ effects were included in the analysis by use of the Geometric Stiffness matrix and a leaning column to add the second order effects of the walls.

For steel moment frames usually the most important aspects of the model are defining the boundary conditions and modeling the panel zone. In this case, the supports at the base of the columns were idealized as pinned supports which is consistent with industry practice, even if it has been shown that typical connection do offer some kind of rotational restraint (Bajwa, 2010; Verma, 2012). Meanwhile, to account for the influence of panel zone deformations, a new model was developed by introducing a rotational spring where the inside flanges of the beams and columns meet, linked rigidly to their respective centroids. This rotational spring was calibrated for each frame via a 3D Finite Element Analysis of the connection using shell elements. Industry practice usually defaults instead to the use of a centerline model with no rigid end zones due to its simplicity over any explicit modeling of the panel zone MBMA (2019b).

From all of the above it can be concluded then that the Smith and Uang formula was developed using almost every assumption that would increase the flexibility of the building. It must be noted, however, that shear deformations, $P - \Delta$ effects and panel zone deformations are not so much assumptions but actual components of frame flexibility. However, possible stiffening effects (from base fixity, non-structural elements, diaphragm action, global system behavior, etc.) were ignored. These assumptions may explain the overestimation of the natural period of metal buildings when compared to the measured values by Kumar et al. (Kumar et al., 2020).

2.1.3 Force distribution along its members

Another important aspect of the ELF approach is correctly assigning the load carried by each frame of the lateral force resisting system along their height given the computed base shear. In the case of metal buildings, which are typically single-story, the distribution along the height reduces to applying the full equivalent force as point loads at the roof. Though ideally this load should be distributed evenly across the rafter beam to simulate the distributed mass, it's usually recommended to apply the load as two point loads at both beam-column joint nodes (MBMA, 2019b), as shown in Figure 2.6. This results in a less conservative estimate of the axial load in the beam compared to applying the full load at just either one of the joints.

Note that, though the MBMA Guide does mention the possibility of using more refined approximations for the application of the distributed load, it does not provide clear recommendations. In fact, it only mentions the possibility of including applied forces at every beam-column joint, which may somewhat improve the results for modular metal buildings. However, the load should ideally be applied wherever the mass is, and so the actual loading

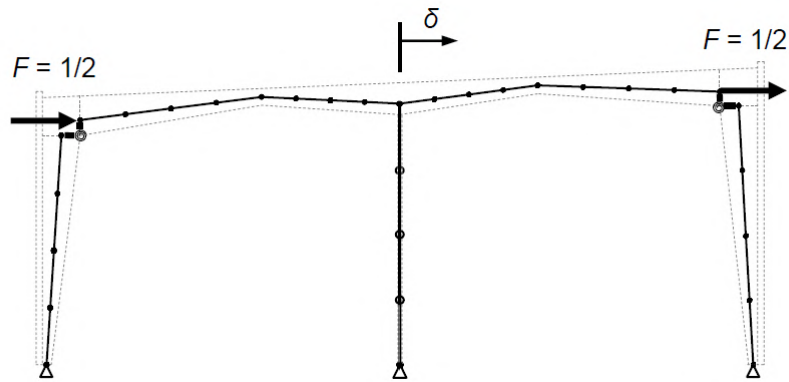


Figure 2.6: Example of loading on a frame for illustrative purposes, taken from Smith and Uang (Smith and Uang, 2013)

condition more closely resembles that of a distributed load at the roof level. This is important not only because it provides a better estimate of the axial force in the beams, but also because it can more accurately capture the bending moment that appears in the beams due to the roof pitch. In gabled, high pitched roofs, the added bending effect due to the distributed horizontal loading (which has a component perpendicular to the roof) could be significant and should be taken into account, especially considering that metal buildings are optimized following the bending moment diagram.

As for how to assign the load to each frame, this would depend on the stiffness of the diaphragm compared to the frames. A flexible diaphragm, assumed to carry no shear, makes it so that the load in each frame is proportional to its tributary mass. On the other hand, a fully rigid diaphragm that forces rigid movement at the roof level would distribute the loads in accordance with the frame stiffness. Most diaphragms usually fall in between, and a full 3D-analysis would be required including the actual diaphragm stiffness. In early design of typical mid-rise buildings, the worst-case scenario of both options can be used to initialize the size of the members.

Implied in the diaphragm classification is that the diaphragm stiffness is measured relative to the stiffness of the lateral system. In turn, ASCE-7 has both prescriptive and analytical ways to classify the diaphragm in ASCE-7 Section 12.3, which depend not only on the type of diaphragm but also on the structural system. ASCE-7 Article 12.3.1.1 provides different structural systems where the diaphragm can be idealized as flexible. If the diaphragm consists of an untopped steel deck, then it can be considered flexible if any of the following is true:

- The main lateral force resisting system consists of Steel-Braced Frames or Shear Walls
- The building is an up to two-story family dwelling
- Specific types of light-frame construction (wood structures)

From the above it follows that metal buildings are not by default included by the provision. In those cases, ASCE-7 Equation 12.3-1 can be used to justify the idealization of the diaphragm as flexible

$$\frac{\delta_{MDD}}{\Delta_{ADVE}} > 2 \tag{2.8}$$

where δ_{MDD} is the portion of the deflection attributed to the diaphragm and Δ_{ADVE} is the portion of the deflection attributed to the frames when a distributed load is applied across the diaphragm.

An example on how to apply this provision can be found in Chapter 9 of Charney et al. (Charney et al., 2020). The structure analyzed, with reinforced concrete shear walls and slab, can be seen in Figure 2.7, which was loaded with a distributed load in the plane of the diaphragm at the diaphragm level (assigned as point loads at each node in of the ends

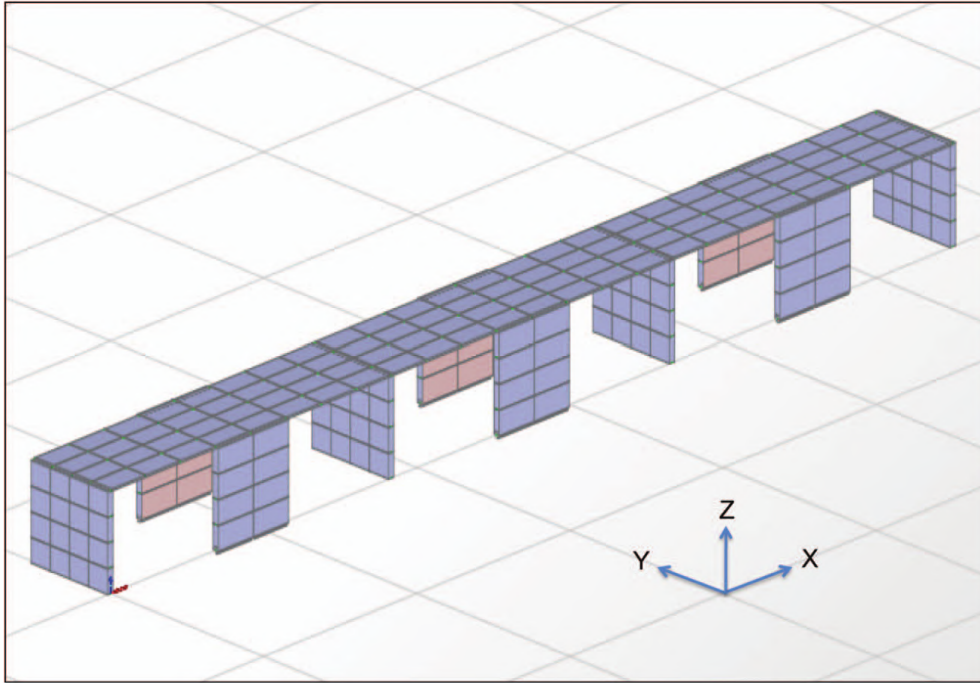


Figure 2.7: Finite-element model for computing diaphragm flexibility ([Charney et al., 2020](#))

of the diaphragm). The results of the example show that the diaphragm deflections are analogous to those of a uniformly-loaded continuous beam with spring supports reflecting the stiffness of the lateral system and no rotational restraints (as the torsional stiffness of a given frame is negligible). The beam properties should include, however, shear deformations and connection slippage which for metal decks is usually modeled with an effective shear stiffness. This approach can be seen in the examples of the Diaphragm Design Manual ([Lutrell et al., 2015](#)). As the example in Charney et al. show, the provision in ASCE-7 is quite restrictive, or at least it makes it very difficult for a diaphragm to be classified as flexible based on analysis ([Charney et al., 2020](#)).

2.1.4 Assumptions Made in Metal Building Design

From the previous sections it becomes noticeable that there are some gaps in the current provisions regarding how to analyze metal buildings, and this is without taking into account discussions on the ductile mechanism of web-tapered moment frames, the appropriate value of R and other details regarding the seismic behaviour of the main lateral load resisting system, which have spurred other research projects funded by the MBMA.

First of all, the classification of the roof diaphragm in metal buildings is not explicitly covered by ASCE-7, which in theory would require to apply Equation 2.8 before proceeding with a flexible diaphragm model. In practice this is not done, and roof diaphragms of all types are considered flexible for the design of metal buildings (MBMA, 2019b).

The two most common types of roof cladding used are of the untopped steel variety: the Standing-Seam Roof (SSR) and the Through-Fastened Roof. Through-fastened roofing is the older of the two (Newman, 2015) and is not much different in essence to the metal sheeting commonly used in walls. It consists of corrugated cold-formed steel panels that are lapped together and fastened to the purlins by self-tapping or self-drilling screws. Meanwhile, Standing-Seam Roofs attach the panels to the secondary framing by virtue of concealed clips. This configuration reduces possible leakage due to drilling while also allowing for more mobility, reducing problems related to thermal expansion. However, due to clip slipping these roofs tend to be a lot more flexible than through-fastened roofing.

Even if through-fastened roofing is known to provide diaphragm action, and recent studies by Wei et al. (Wei et al., 2020) have shown that the SSR does provide some stiffness (which could be used to provide lateral buckling restraint to the purlins), it is still current practice to consider the diaphragm as fully flexible without following ASCE-7 Equation 12.3-1 (MBMA, 2019b).

This leads, however, to some oddities in the design of metal buildings. It is common for the inner bays to consist of web-tapered moment frames, with the endwalls being concentrically-braced frames. Having two different structural systems along the same direction would typically lead into estimating the building period in accordance with ASCE-7 Table 12.8-2 as “other”. However, given the flexible diaphragm assumption above it could be possible to treat each bay as its own independent structure, treating the interior bays as “steel moment frames” and the exterior bays as “other”. This is not what Equation 2.5 was derived for, given that it was the result of measuring the global behavior of buildings with clear and specific structural systems, and there is nothing that would imply that the equations would hold up for individual frames of a given building. This becomes more egregious when considering the equations themselves were derived with data from mid-rise buildings, and – whether the diaphragm could classify as flexible or not – a single period for the whole structure was extracted. Moreover, the results from Kumar et al. imply that that mode shapes of metal buildings are also global in nature, and may not be directly related to the period of each individual bay (Kumar et al., 2020). This also warrants a discussion on the accuracy of the flexible diaphragm assumption.

2.2 Structural modelling of the main lateral resisting system

If an analytical model of a metal building were to be built for the purpose of estimating the natural period, then accurately predicting the stiffness of the primary framing is evidently of great importance. For structural steel, the modulus of elasticity is quite consistent and so most of the uncertainty comes in how the connections are modeled, as well at what assumptions are made in the development of the frame element.

In turn, the focus ends up being placed on whether or not to include shear deformations, how to account for the panel zone deformation and how to correctly model the boundary conditions.

2.2.1 Modeling of web tapered elements

The American Institute of Steel Construction (AISC) has provided guidelines on how to model web tapered members since 2011, with the second edition of the Design Guide coming out in 2021 ([White et al., 2021](#)). Within, two methods are identified for modeling frame elements. The first consists in discretizing the non-prismatic frame into shorter, prismatic elements. This is essentially a finite element approximation, and the results will converge to the true solution as the length of each discretized frame tends to zero.

Alternatively, the element stiffness matrix of the frame can be obtained through the inversion of its flexibility matrix ([Charney, 2008](#); [McGuire et al., 2020](#)). The main advantage of this approach is the the exact solution can always be obtained as long as the variation of the members sectional properties and centroid along the length are accurately described. It also allows for simple, direct inclusion of shear deformations if so desired.

One of the difficulties with modeling web tapered members is that the centroidal axis is no longer linear if the the section isn't symmetric (i.e., the flanges have different thickness). In that case there is an interaction between axial forces and bending moments. Though this can be captured by the formulation described above, in some implementations this effect is ignored, treating the centroidal axis as linear between nodal points ([Smith, 2013](#)). The loss of accuracy due to this simplification is assumed to be small, especially if the member is discretized along its length anyway to obtain a more realistic lumped mass representation or to include $P - \delta$ effects in the analysis.

Finally, a similar difficulty with modeling web tapered members is how to properly account for changes in flange or web thickness in non-symmetric sections. This change would create a discrete jump in the centroid at the location of the discontinuity. For this case, AISC Design Guide 25 proposes two options. The first (and “exact”) solution would be to include a rigid link connecting the centroids at each end of the discontinuity. A simpler, approximate approach would be to ignore this effect and slightly modify the node locations so that rigid links can be avoided. Given that the shift in the location of the centroidal axis is very small in comparison to the depth of the member, this second approach is reasonable and has been used by Smith in the development of the metal building frame models ([Smith, 2013](#)).

As for how commercial software handles non-prismatic elements, the precise formulation is not open-source and so no specific details can be provided. It is assumed, however, that SAP2000 ([CSI, 2021](#)) uses a very similar framework to the one described above assuming a linear centroid, as the only parameters that are input into the program are the start and end cross sections, along with the assumed variation in the moment of inertia along the length.

2.2.2 Shear Deformations

Plenty of research has been done on what the main sources of deformation in steel moment frames are, though most of this work has been done for mid to high-rise buildings. Charney et al. found that shear deformations in the beams and columns could account for 8 to 26% of the total displacement, the massive range being dependent on the clear span of the bays and total number of floors ([Charney et al., 2005](#)). Metal buildings, however, fall out of the range of the study, as they are usually 1-story buildings with a clear span of up to 100 ft , while the study covered bays with 10 to 20 ft spans. Since the influence of shear decreases with span length (as flexural behavior becomes dominant) it would be expected for metal

buildings to be much less sensitive to the inclusion of shear deformations in the analysis.

Smith and Uang analyzed the effect of shear deformations on 192 2D-models of metal buildings designed per current standards ([Smith and Uang, 2013](#)). Results showed that not accounting for the effect of shear deformations would result in an overestimation of the stiffness of about 5% in the worst-case scenario, with the average difference being close to 2%. Considering that the natural period is proportional to the square root of the stiffness, then neglecting shear deformations would result in a 1% underestimation of the period on average.

Based on these findings, the authors conclude that the inclusion of shear deformations is not necessary for metal buildings. However, currently most structural analysis software is able to account for it with no meaningful difference in computational cost. In fact, SAP2000 ([CSI, 2021](#)) has it on by default in their element formulation, and so there is no real reason not to include them.

2.2.3 Panel Zone Deformations

Correctly accounting for panel zone deformations is harder to model than the former case, as it may require a full finite element analysis of the of the panel to find the parameters that need to be introduced into a simplified model of the connection (there are ways to estimate the values given the sectional properties of the connection, and the reader is referred to ([Charney and Marshall, 2006](#)) for more information). Panel zone deformations – a function of panel zone shear and joint flexural deformations – can have a significant effect on story drift.

At the subassemblage level, deformation of the panel zone in shear explains around 25% of the total drift, while flexural deformations can account for 10% of the total drift ([Charney and Pathak, 2008a,b](#)). This last result is significant because flexural deformations at the

joint level is not included in the most common panel zone models such as the Krawinkler or Scissors models (Charney and Marshall, 2006).

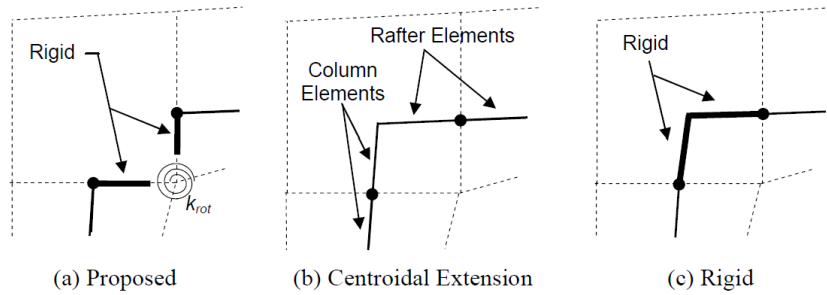


Figure 2.8: Panel Zone Model Comparison (Smith and Uang, 2013)

In their analysis of metal buildings, Smith and Uang (Smith and Uang, 2013) used a custom model that consisted of a rotational spring where the inner flanges of the beams and columns meet, linked to the centerline of each element through a rigid link (Figure 2.8a). As mentioned before, this rotational spring was calibrated based on 3D Finite Element Analysis of the connection using shell elements for its components. The choice in spring placement in the proposed model was to obtain compatible deformations in the panel zone region, whereas the centerline and scissors models assume unrealistic deformed shapes (such as allowing overlap between the column and beam flanges under negative moments) (Smith, 2013). Similar results can be obtained when using the revised Krawinkler model (Charney and Marshall, 2006).

The use of more sophisticated models to compute drift in metal buildings is not standard in the industry, which favors instead using a centerline model, either considering rigid frame elements within the panel (rigid endzones), or simply extending the cross-sectional properties of the beams and columns. The rigid endzone model, though commonly used for concrete moment frames, has been shown to underestimate drift. The centerline model with no rigid endzones, however, provides reasonable estimates for steel moment frames due to offsetting

inaccuracies. On one hand, it underestimates shear deformations at the joint level. On the other hand, extending the beams and columns properties in the endzone regions overestimates the bending moments, and in turn results in larger overall deflections of the frame elements. Charney and Pathak showed at the subassembly level of a typical steel moment frame that the centerline model could underestimate displacements by 10% (Charney and Pathak, 2008a). Smith and Uang arrived to similar conclusions in their own study, with the deflections of the frames modeled with their panel zone model could be up to 15% more flexible than the same frame using a centerline model (Smith and Uang, 2013). However, from a statistical standpoint the models with the centerline model had on average a difference of 0.2% compared to the more sophisticated ones. This result is actually quite interesting as it implies that, even if the results have scatter, the centerline model actually does a very good job of predicting the general behavior of the frames, which justifies its use in practice.

2.2.4 Base Fixity

Explicit modelling of the actual boundary conditions at the column base, similar to the effect of panel zone deformations, is also not usually done in practice due to the cost and complexity associated with it, even if in recent years there have been attempts to streamline the process through automated applications (Verma, 2012). The connection of the columns to the foundation is usually resolved by welding an endplate which is then bolted into place with at least 4 anchor bolts (Newman, 2015). The overall rotational stiffness of the connection is mostly controlled by the size of the column, the size and thickness of the baseplate, and the number and location of the anchor bolts.

The main deflection mechanisms are, then, the bending of the end plate and the deformation under stress of the anchor bolts in tension, with the column pivoting from the extreme

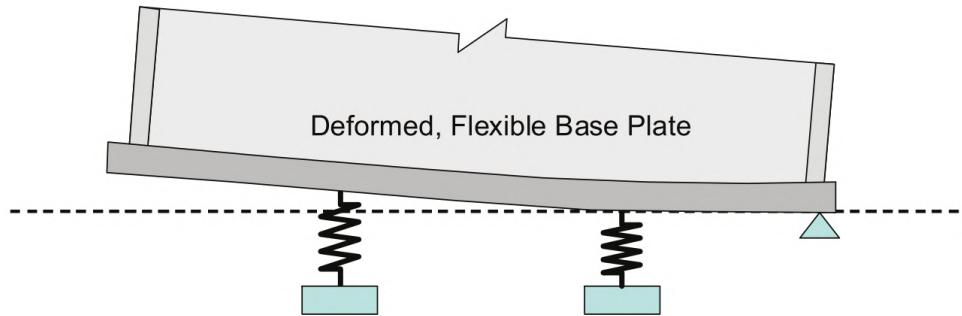


Figure 2.9: Modeling of Column-to-Base Connection when Base Plate is Flexible (Bajwa et al., 2010)

compression fiber of the baseplate (Figure 2.9). Flexibility of the underlying soil can also play an important role, especially if the column has an isolated foundation.

For design purposes, metal buildings forego a detailed analysis of the column connection and are instead designed as either fully fixed or fully pinned. Due to the lower total monetary cost of the design, the pinned solution is the overwhelmingly favored choice (Newman, 2015). Smith and Uang, following this design methodology, did not include the effect of base stiffness in the analysis of 2D-frames (Smith and Uang, 2013). Their modeling approach was justified based on full scale shake table testing of two metal building frames, that showed that, due to the deformation of the base plate creating a dishing effect, there was essentially no rotation stiffness of the column base for rotations smaller than $0.02rad$. The behavior, however, was extremely nonlinear. For larger rotations, contact between the flanges and the base would impede the previous motion and significantly increase the rotational stiffness of the connection (Smith, 2013).

On the other hand, Bajwa et al. studied the effect of the base rotational stiffness in the overall stiffness of a metal building frame and found that, in theory, the stiffness lies somewhere in between the pinned and fully fixed options (Bajwa et al., 2010). This is significant since the

difference in the drift estimation between the two extreme cases was found to be a factor of 2. Similarly, Kumar et al. found that the fundamental period of a metal building in Christiansburg, VA, obtained via a 3D Finite Element Model could decrease by 40% when modeled with fixed supports instead of pinned, with the measured period lying in between the two of them (Kumar et al., 2020).

2.2.5 Discussion

Previous subsections focused on different modelling aspects for the main frame of a metal building, working under the assumption that a 2D-model of the bare frame is enough to fully characterize the stiffness and – in consequence – the natural period. However, previous experiences (Bajwa et al., 2010; Kumar et al., 2020; Lamarche et al., 2009) show that there may be a significant difference in stiffness between the bare frame and the building in service for single-story buildings, and that the Smith and Uang equation, developed using said analytical models, seems to overestimate the natural period.

The effect of non-structural elements has been studied before for different structural systems. Kim et al. performed a literature review of reported differences between modeled and measured periods of vibration, and found numerous cases where – when modeling only the bare frame – the analytical period was overestimated by 40 to 70% in reinforced concrete structures (Kim et al., 2009). He then proceeded to calibrate a sophisticated 3D-FEM of 3 different buildings and found that including the flexural stiffness of the diaphragm and modelling the non-structural walls could reduce the inaccuracy by half, with the rest of the difference explained by the actual modulus of elasticity of concrete compared to the one used in design.

As mentioned before, Bajwa et al. attempted to use a detailed 2D Finite Element Model of the main frame of a metal building with a standing-seam roof to predict drift (Bajwa et al., 2010). As part of an experimental test, a force of a magnitude similar to the design wind load was applied to the different bays of the structure, one at a time, with the deflection being measured at the loaded frames and the adjacent ones. The model, which included shear deformations, panel zone deformations and explicitly modeled realistic boundary conditions still overestimated the drift by up to a factor of 2. It was not until a full 3D-model of the structure was built using shell elements for the primary and secondary framing – and including the added stiffness of the endwall and roof cladding – that better correlation between the measured and tested displacements were reported (Bajwa, 2010). However, even if the displacement on the internal frames was correctly accounted for, there were still significant differences between the measured and predicted values of the displacements for the endwalls, where most of the stiffness is provided by the cladding.

A very similar analysis was carried out by Wrzesien et al. (Wrzesien et al., 2015). In this case, however the test was repeated for two different cases: First, with just the bare frame; second, with the roof cladding installed. The experimental tests were used to validate the full 3D-modeling of two different single-story building with cold-formed portal frames and through fastened roofing. The framing model considered all column bases as ideally pinned and used frame elements for the primary frames instead of using shell elements for the web and flanges, and neglecting the secondary framing. Meanwhile, for the roof diaphragm an equivalent truss element was used. The model generally agreed with the experimental results, which showed the stiffness of the building increased by a factor of 10 due to diaphragm action of the roof, since it in turn made the stiffer exterior frames to participate in the load distribution. Note that, in Bajwa et al., which had a standing-seam roof, only limited diaphragm action was seen, with each bay working fairly independently of each other.

Perhaps the most detailed calibrated model for single-story buildings including the cladding was developed by Gryniewicz et al. ([Gryniewicz et al., 2021](#)). In this case, the structure was quite similar to a metal building with gabled frames for endwalls and a truss beam for a rafter in internal frames. The building was tested by applying a point load of 50% the service wind load for the structure to behave in its elastic range in 3 different phases: The bare frame; the frame with the roof installed and the completed building with the wall sheeting. From the experimental tests it could be seen that the roof cladding increased significantly the combined behavior of the frames, reducing the displacement at the loaded frame by a factor of 3, and evening out the displacements of all the bays, the diaphragm behaving as essentially rigid. Beyond that, the tests on the full building proved that, even if the sheeting was not designed for diaphragm action, it still increased the stiffness of the endwalls significantly, which in turn caused the displacements to drop by a factor of 10. Also, since in the last test the walls were so much stiffer, the building exhibit more of a flexible diaphragm behavior than in the second test, when only the roof was present. Going by the work of Fischer and Schafer ([Fischer and Schafer, 2021](#)), it is fair to assume the stiffness of the walls and roof was relatively close.

A 3D-model of the building was also developed and validated against the experimental tests results ([Gryniewicz et al., 2021](#)). This consisted of frame elements for the main and secondary framing, with its supports idealized as pinned. This is, again, a much simpler and fairly standard approach to modelling framing. Instead, a large focus was put into modelling the cladding. In this case, an orthotropic plate model was used to analyze the panels, but a lot of care was put into its connection to the secondary framing, by using spring supports to the purlins and girts for each of the fasteners in the roof. This level of detail is, of course, prohibitive in design, as it is common for different people and trades to be in charge of the main framing and the cladding respectively. For the wall cladding,

meanwhile, a simpler approach was used by defining a single effective shear modulus for the whole diaphragm. However, the results were remarkable, with a 5% difference between the estimated and measured displacements for the main frame tests, which stayed consistent in the subsequent tests.

All these experiences show that modelling of the steel cladding elements could be essential to adequately describe the behavior and stiffness of single-story buildings, and could even accurately predict their non-linear response and collapse load (Roberts et al., 2021). Though it is true that the the latter two case studies (Gryniewicz et al., 2021; Wrzesien et al., 2015) both had Through Fastened Roofing, whose in-plane stiffness is believed to be significantly higher than SSR, it seems as though 2D-modelling may not be enough for the SSR case either. This puts into perspective the previous look into the main parameters and modelling assumptions that influence the stiffness of metal buildings. If the main frame is relatively only a small portion of the overall stiffness of the building, then it is valid to ask whether it's necessary to put most of the effort into it. Instead, it may be worth looking at the added stiffness provided for cladding and how it can be modeled. Note, however, that the cladding is not designed to carry lateral load.

2.3 Modeling of steel sheeting

Analytical modeling

Defining the stiffness of metal panels used in cladding is not an easy endeavor. First of all, the panels themselves tend to be orthotropic in nature due to their one-way corrugation. In shear, one of the main sources of deformation is the warping or distortion of the sheet due bending of the corrugation, and then pure shear deformation. Given that the most common

way to model panels is by using flat plate elements, properly accounting for the behavior would require finding equivalent rigidities to input to a flat plate model. One of such models was proposed by Xia et al., and it is notable that not even an orthotropic model is able to match all 8 rigidities described in the paper, as an orthotropic model only has 5 parameters compared to 2 for an isotropic model (Xia et al., 2012).

Another significant deformation source of diaphragms is at the connection level. Both the seam-fasteners splicing adjacent panels and the fasteners used to attach the cladding to the girts and purlins create flexible connections that significantly reduce the overall stiffness of the diaphragm in shear. This, in turn, means that the number, type and location of the fasteners play a significant role in the overall behavior of the diaphragm and careful consideration of the boundary conditions is required. In Bajwa (Bajwa, 2010), the boundary conditions were modeled as roller supports in the corners of the panels, which probably underestimates the stiffness provided by the connections. This becomes noticeable when looking at the discrepancy between the measured and predicted displacements of the end-walls. Gryniewicz et al., meanwhile, explicitly modeled each fastener as a spring support connected to the secondary framing (Gryniewicz et al., 2021). The latter approach, though it showed exceptional accuracy, is extremely costly and time consuming as it requires careful modeling of every fastener, including its stiffness, and is not practicable for design considerations.

2.3.1 Developments in the U.S.

The difficulties in predicting the stiffness of diaphragms through analytical procedures for different types of sheeting profiles and connection types led to extensive experimental research both in the U.S. and in Europe. In North America, extensive testing was done by

Larry Luttrell since 1965 (Luttrell, 1965), first as a Graduate Student in Cornell and then as a Professor at the University of West Virginia. The results of his work are summarized in the Steel Deck Institute’s (SDI) Diaphragm Design Manual, which is periodically updated and is now in its fourth edition (Luttrell et al., 2015). The equations have not changed much since they were first published and are now part of AISI S310-16, the North American standard developed by the American Iron and Steel Institute (AISI S310-16, 2016). However, every time a new deck system is developed, experimental tests are needed to create equations to estimate their strength and stiffness in the same fashion. Considering that roof decks are in constant evolution, a large number of tests have been done recently such as for aluminum decks (Avcı et al., 2016), cassette diaphragms, sandwich panels and Standing Seam roofs (Davies and Bryan, 1982; Wei et al., 2020). The special case of diaphragms attached to wood structures can be found in the book A Primer on Diaphragm Design (Luttrell and Mattingly, 2004).

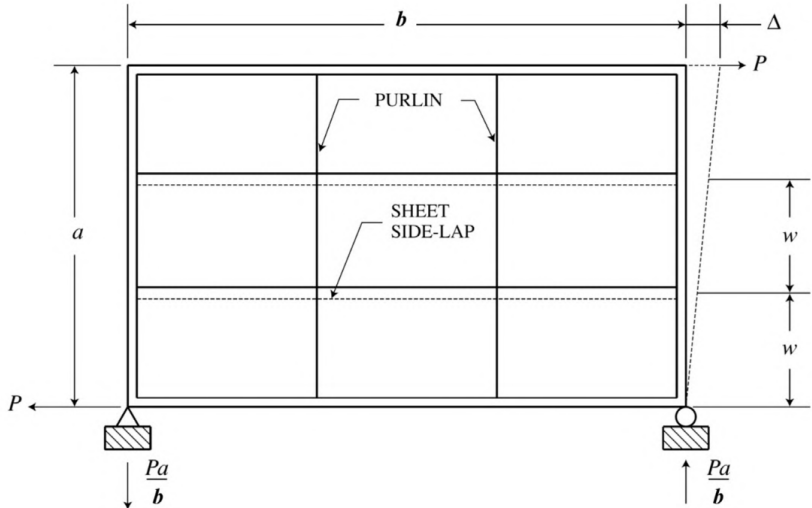


Figure 2.10: Diaphragm distortion for shear strength and shear stiffness calculations (Avcı et al., 2016)

In any case, the stiffness of a roof or wall assembly is obtained by doing a cantilever test. A schematic of the test setup can be seen in Figure 2.10 for a roof assembly specifically, placed

horizontally. It should be noted that, in all these tests the orientation of the panels stays perpendicular to the span (i.e., the panels are fastened to the purlins which are perpendicular to the applied loading), and all four sides are fastened, which greatly increases the stiffness as it allows for the transfer of forces to the edge members in tension compared to when only two sides are fastened. By measuring the force P required to impose a deflection Δ , it is possible to find the distortion $\gamma = \Delta/a$ and the average shear stress $\tau = P/(bt)$, where a and b are the dimensions of the assembly and t its thickness. Then, treating the assembly as an isotropic plate, the effective shear modulus G can be found as

$$G = \frac{\tau}{\gamma} = \frac{P}{bt} \frac{a}{\Delta} \quad (2.9)$$

The result, however, is more commonly reported as a stiffness G' as it is independent of the thickness and can be directly measured during testing as

$$G' = G t = \frac{Pa/b}{\Delta} \quad (2.10)$$

where Pa/b is the reaction at the supports. The predictive equation for the stiffness, as presented in AISI S310-16 is

$$G' = \left(\frac{Et}{2(1 + \mu) \frac{s}{d} + \gamma_c D_n + C} \right) K \quad (2.11)$$

where

- E is the modulus of elasticity of steel
- t is the thickness of the steel plate

- μ is the Poisson's ratio
- d and s are the panel's corrugation pitch and its width respectively
- K is equal to 1 when fasteners are placed at lap-down into steel supports, and to 0.433 if fasteners are placed at lap-up
- D_n is a warping factor which can be taken as D/L , with D calculated as per Appendix 1 and L being the total panel length. The values of D for different typical panel profiles can be found in the Diaphragm Design Manual ([Luttrell et al., 2015](#))
- γ_c is a support factor that considers the number of spans and goes from 1.0 for up to 2 spans to 0.58 for more than 7 spans
- C is a slip coefficient

The slip coefficient C is computed as

$$C = \left(\frac{Et}{w} \right) \left(\frac{2L}{2\alpha_3 + n_p\alpha_4 + 2n_s \frac{S_f}{S_s}} \right) S_s \quad (2.12)$$

where

- w is the cover width of the interior panels
- S_f and S_s are the connection flexibility to the structure and sidelaps respectively and depend on the connection type. For screws into steel, the values are inversely proportional to the square root of the plate thickness.
- α_3 and α_4 are a measure of the distribution of the interior and exterior fastener group across the panel width.
- n_s is the total number of sidelap connections, and n_p is the number of interior supports.

Example

For example, let's apply this to a $0.0295in$ thick cold-formed Wide Rib panel Wall used as a wall diaphragm in a metal building. The length of the panel is $20ft$, and each panel has a width of $36''$ for a total width of $80ft$. For a Wide Rib panel, the ratio s/d can be taken as 1.454, and the warping factor D_n as 53.6 assuming it is fastened at every other valley as found taken from Diaphragm Design Manual (Luttrell et al., 2015). Also taken from the Manual, With a 36-4 fastening pattern, α_3 can be taken as 1.33. The number of spans is 4, and so $\gamma_c = 0.8$ and n_p is 3. n_s is 4 assuming one screw per span. Finally, considering the use of self-drilling screws at lap-down, $K = 1$, $S_s = 0.022$ and $S_f = 0.0097$ as indicated in AISI S310-16 (AISI S310-16, 2016).

Inserting the appropriate information into Equation 2.12 gives out a value of $C = 20$ for the slip coefficient, and finally a stiffness G' of approximately $13kip/in$. Dividing by the thickness gives an effective shear modulus of about $443ksi$, which is only 4% of the shear modulus of steel ($G = 11,500ksi$).

That same wall configuration but used in a $30ft$ wall with 5 spans would result in $G' = 14kip/in$. Similarly, using $15ft$ the value becomes $11.5kip/in$ meaning that the effective shear modulus is not particularly sensitive to building height compared to the configuration itself. For example, simply changing the fastener pattern at the panel edges to each valley (a 36-7 configuration) instead of every other one would result in D_n decreasing tenfold, causing the overall stiffness to shoot up to $36.27kip/in$. Given the sensitivity of D_n , the engineer must be careful in its evaluation. Finally, note that, though the results here presented appear small, the interior frames of metal building systems can have stiffness values as low as $2kip/in$, meaning that cladding could indeed contribute significantly to the building's overall stiffness.

2.3.2 European approach

The European equations for predicting the stiffness of wall and roof diaphragms were the result of research Eric Bryan on stressed-skin design, a design approach for buildings where the sheeting is actively accounted for in the load path as diaphragms (Davies, 2006). The results of his experimental research with J. Michael Davis led to the publishing of the book “Manual of Stressed-Skin Design” in 1982 (Davies and Bryan, 1982). The equations presented there have remained virtually the same since, and were first adopted by European Convention for Constructional Steelwork in the “European Recommendations for the Application of Metal Sheeting Acting as a Diaphragm – Stressed Skin Design” (ECCS, 1995). This document was later adopted by reference by the Eurocode (Davies and Bryan, 1982).

Compared to the approach in AISI S310-16, the equations in the European Recommendations explicitly distinguish the flexibility of each of the components of the cladding, differentiating between profile distortion and shear deformation of the sheeting; fastener deformation for both the seam fasteners and the connections to the girts and purlins; and the axial strain in the edge members. The sum of all the component flexibilities gives out the total flexibility of the system, defined as $c = \Delta/P$

Another difference compared to the equations developed by Larry Luttrell is that the European Recommendations do a distinction between diaphragms connected on all 4 sides vs only 2 sides, the latter being a more flexible. Some components of the flexibility also have different expressions whether the sheeting spans perpendicular to the diaphragm or in parallel.

Revisiting the previous example

This time, let’s look at the equations through an example: the same Wide Rib panels from before. The reader is referred to the appropriate references for more detail for different cases

(Davies, 2006; Davies and Bryan, 1982; ECCS, 1995). The flexibility due to profile distortion is

$$c_{1,1} = \alpha_1 \alpha_4 \frac{ad^{2.5}K}{Et^{2.5}b^2} \quad (2.13)$$

where α_4 accounts for the number panels along the depth of the diaphragm (only applies to sheeting perpendicular to the diaphragm); α_1 accounts for the number of spans (similar to γ_c in the AISI S310-6); a is the dimension of the panel perpendicular to the direction of the corrugation; b is the dimension of the panel parallel to the corrugation; t is the thickness of the metal sheet; d is the pitch of the corrugation; K is sheeting constant that depends on the fastener profile and the properties of the corrugation (pitch and width); and E is Young's modulus.

For sheeting parallel to the span, $a = 80ft$ and $b = 20ft$. For a structural wall, where a single panel covers the depth of the diaphragm, $\alpha_4 = 1$. α_1 becomes 0.70 considering 4 spans as before (5 girts). d is $6in$ and t is $0.0295in$. K , assuming fasteners in every other groove, is 0.779. Replacing in Equation 2.13 (in SI units) gives out a value of $c_{1,1} = 0.182in/kip$.

The flexibility due to shear strain is given by

$$c_{1,2} = \frac{2a\alpha_2(1+\mu)[1+(2h/b)]}{Etb} \quad (2.14)$$

where α_2 is a function of the number of spans; μ is the Poisson's ratio; and h is the height or depth of the corrugation. For the case with 4 spans, $\alpha_2 = 0.67$, and considering a standard $h = 1.25in$ depth the resulting flexibility is $c_{1,2} = 0.012in/kip$ (ECCS, 1995). Note, then, how the deformation of the metal panel is almost exclusively due to distortion of the corrugations.

Next, the fastener deformation needs to be computed. The added flexibility by the fasteners connected to the purlins is

$$c_{2,1} = \frac{2as_p p}{b^2} \quad (2.15)$$

where s_p is the slip per fastener which can be taken as $0.026in/kip$ (ECSS, 1995); p is pitch of the fasteners ($12in$ in the example); As a result, the flexibility is $c_{2,1} = 0.011in/kip$.

As for the seam fastener deformation, the expression to find the flexibility is

$$c_{2,2} = \frac{2s_s s_p (n_{sh} - 1)}{2n_s s_p + \beta_1 n_p s_s} \quad (2.16)$$

where s_s is the slip per seam fastener (taken as $0.044in/kip$) (ECSS, 1995); n_{sh} is the number of sheet widths per panel (for an $80ft$ building, this would be 27); n_s is the number of seam fasteners per side lap (4); n_p the number of purlins, including the edge ones (5); and β_1 is a function of the total number of fasteners per sheet (for 4 fasteners per purlin per width, $\beta_1 = 1.04$). Replacing above, the result is $c_{2,2} = 0.137in/kip$

The flexibility of connection to the end members differs greatly whether all 4 sides are fastened or only 2 sides. Assuming 4 sides fastened, the equation is

$$c_{2,3} = \frac{2S_{sc}}{n_{sc}} \quad (2.17)$$

where S_{sc} is essentially the same as s_p ; and n_{sc} is the number of fasteners per end rafter (108), which results in a value of $c_{2,3} = 0.00049in/kip$.

If, instead, only 2 sides are fastened the expression turns to

$$c_{2,3} = \frac{2}{n_p} \left(s_{pr} + \frac{s_p}{\beta_2} \right) \quad (2.18)$$

where s_{pr} is the flexibility of the purlin-rafter connection, which can be conservatively taken as $0.245in/kip$ (ECCS, 1995); and β_2 is a function of the number of fasteners per sheet width (for 4 fasteners per purlin, the value is 1.11). With these numbers, the flexibility considering 2 sides fastened would be $c_{2,3} = 0.054in/kip$, two orders of magnitude larger than if the panel was fastened on all 4 sides ($0.00049in/kip$).

With all these flexibilities, the total flexibility in true shear can be computed as

$$c' = \frac{b^2}{a^2} (c_{1,1} + c_{1,2} + c_{2,1} + c_{2,2} + c_{2,3}) \quad (2.19)$$

which results in $0.021in/kip$ for the case with fasteners in all four sides ($0.025in/kip$ if connected in two sides). Finally, the total flexibility can be obtained by adding the deformation due to axial strain in the edge members

$$c = c' + c_3 \quad (2.20)$$

with $c_3 = 2b^3/3EAa^2$, where A is the area of the edge element. Assuming a W10x60 column ($A = 17.6in^2$), then $c_3 = 1 \times 10^{-5}in/kip$ and the total flexibility c becomes $0.025in/kip$. In order to be able to compare this number with the G' value obtained using AISI S310-16, it is necessary to remember that¹)

¹The Equation is rewritten acknowledging a and b are inverted in the European Recommendations compared to Figure 2.10

$$G' = \frac{P b}{\Delta a}, \quad c = \frac{\Delta}{P} \quad (2.21)$$

from which follows that $G' = b/ac$. Using the values from the example the European Recommendations estimate a stiffness of $11.7kip/in$, which is quite similar to the result obtained before ($14kip/in$). It's also notable that accounting for only 2 sides fastened would drop the value to $10kip/in$. Though not a significant change in this particular example, the effect is more notable with the increase in number of fasteners, as the flexibility due to profile distortion becomes less of a factor compared to the added flexibility of having only two sides fastened.

2.3.3 Limitations of current empirical equations

As mentioned before, the cladding industry is constantly coming up with new systems and sheet profiles that differ greatly from the original setups that were tested, and research can't keep up. One such example is the patented metal sheeting developed by Strukuroc (US Patent 7,661,235 B2), which is essentially a flat plate with hidden fasteners and a male-female sideclip creating a friction connection between adjacent panels (Figure 2.11). No stiffness data is publicly available for this system. It could be argued that these panels resemble a cassette profile. In that case, Davies argues that European Recommendations can be used while neglecting the added flexibility due to profile distortion (i.e.: assuming $K = 0$) as the panel is flat (Davies, 2006). Also, since the system does not make use of seam-fasteners, the flexibility may be greatly increased similarly to a standing-seam roof and bear no real structural strength or stiffness.

Similarly, there is little information on the stiffness standing-seam roofs despite their popularity. Given their limited diaphragm action, as shown by Bajwa et al. (Bajwa et al., 2010),

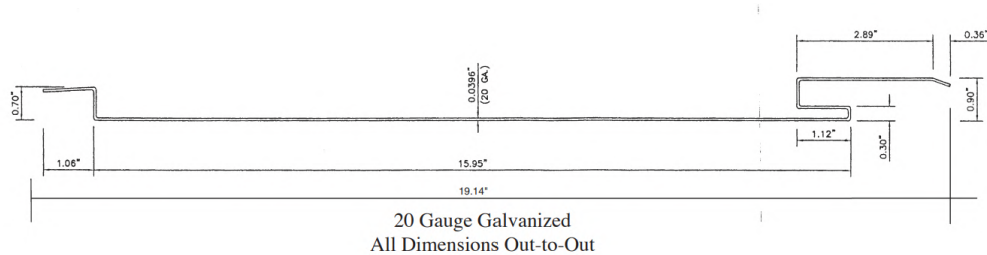


Figure 2.11: Profile of the Strukturoc system (Strukturoc, Inc.)

both AISI S310-16 and the European Recommendations neglect their stiffness altogether (AISI S310-16, 2016; ECCS, 1995). Knowing the stiffness, however, could be important to obtain an accurate estimate of the natural period that can capture what is measured in the field. Work by Wei et al. found small values of stiffness K – measured as the deflection at midspan of a “simply supported” diaphragm due to a point load in the longitudinal direction (See Figure 2.12) – that could vary from $0.087kip/in$ to $8kip/in$ with a median value of about $0.5kip/in$ depending on the clip and panel profile type (Wei et al., 2020). Most of the deformation seemed to be explained by the deformation of the clips.

To convert the K stiffness values to a shear stiffness G , the solution to a simply supported beam to a point load (including shear deformations) needs to be analyzed. For the purpose of this analysis and just to get an approximate number, the portion of the displacement due to flexure will be ignored. Given a point load P at midspan, the absolute value of the shear in the deep beam remains constant at $V = P/2$. From there it follows that the displacement δ at midspan is

$$\delta = \int_0^{a/2} \frac{V}{bG'} dx = \frac{V}{2} \frac{a}{bG'} = \frac{Pa}{4bG'} \quad (2.22)$$

Then, considering that $K = P/\delta$, the stiffness G' can be obtained as $G' = Ka/4b$. Considering the tests had a length a of $22ft$ and a width b of either $9ft$ or $6.5ft$ depending on the

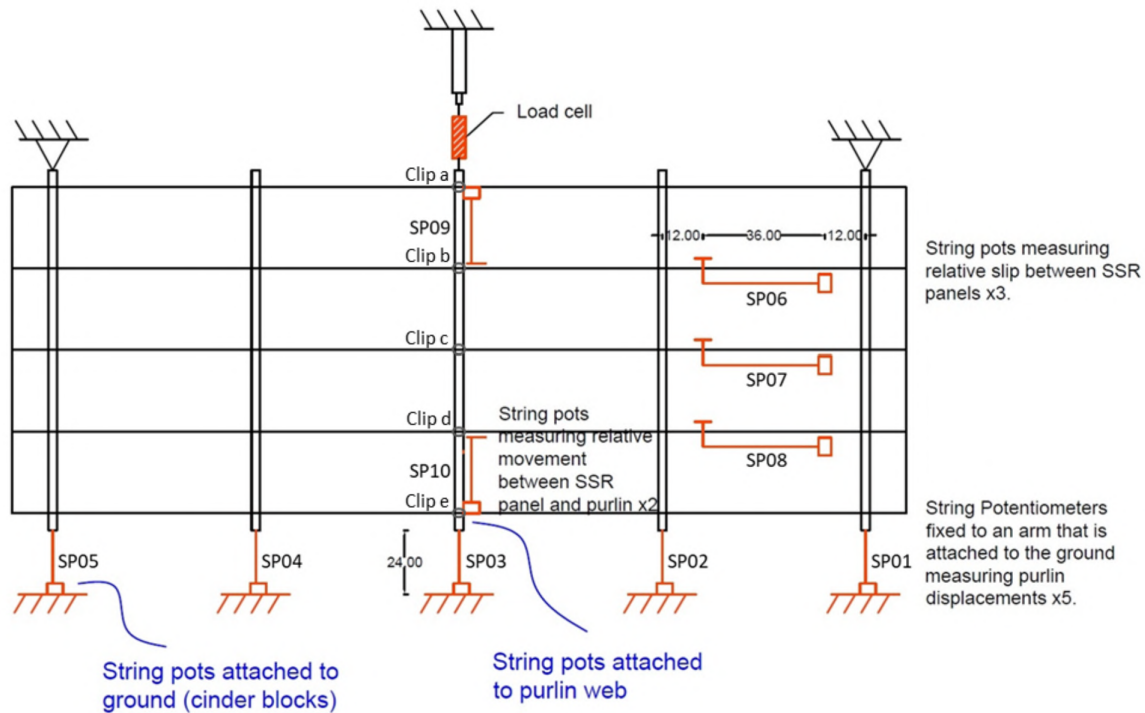


Figure 2.12: Schematic view of instrumentation layout (Wei et al., 2020)

panel width, the value of G' for the SSR may be around $0.3kip/in$ which is indeed orders of magnitude smaller than typical through fastened roofing and virtually negligible. However, the tests had significant scatter, with some specimens reaching $2kip/in$ (No. 5 and 6) and, in one case (No. 4), reaching a stiffness upwards of $7kip/in$. This later number is closer in range to what through-fastened roofing, not designed for diaphragm action, could provide. It should be noted as well that most of the deformation in these tests was due the deformation of the clips, which were working in the minor axis. However, the expected diaphragm action between frames would find the clips acting in their major axis. Moreover, extrapolating the results from tests to roof assemblies proves challenging as the connection of the roof to the eaves can significantly increase the stiffness of the diaphragm, but the effect is dependent on scale. Also, any test setup that does not include this connection would underestimate the stiffness, as argued by Fisher and Nunnery (Fisher and Nunnery, 1996). In fact, the authors

recommend measuring the stiffness with a cantilever test with the purlins opposed. All this means that the measured stiffness by Wei et al. may not be representative of the behavior in the transverse direction for the purposes of evaluating the diaphragm action and inclusion in a 3D-model.

In the end, the limited amount of information available for newer metal building construction makes it extremely hard to predict their natural period through analytical models since the current available equations mostly do not apply to many types of common cladding. Parameter calibration and narrowing down the potential stiffening effects of cladding via experimental testing is then necessary before trying to extend the results to synthetic structures.

2.4 Experimental Testing for Period Extraction

Throughout this chapter it's been brought up repeatedly how current methods of structural analysis seem to fall short in correctly capturing the behavior of metal buildings, and the importance of doing experimental testing to obtain a realistic value of the natural period. One of the reasons the work by Goel and Chopra ([Goel and Chopra, 1997](#)) is so valuable is that created a dataset of buildings excited with large amplitudes of shaking (even above $0.15g$) with the structures remaining in the elastic range. This was possible because it is reasonably common for tall buildings in California to be instrumented with accelerometers and monitored during the lifespan, and even then it took years to capture medium-magnitude seismic events.

For metal buildings, which are not usually instrumented, carrying out a similar study would be more costly if even feasible. Another option is to purposely excite the structures to increase the level of shaking using actuators or a rotating eccentric mass system. In recent

years it has become popular to perform system identification (extracting dynamic properties of structures) by using ambient vibrations instead of actively exciting the structure, which can sometimes be difficult and/or expensive to do. In fact, recent period estimation formulas around the world have been obtained via ambient testing (Lamarche et al., 2009; Pan et al., 2014). However, it is fair to wonder if the properties at low amplitudes of vibration captured during ambient testing correlate well with those during a significant earthquake. Some argue that the influence of non-structural elements and cladding reduces with the amplitude of vibration, as most of the added stiffness can be attributed to friction at the connection level such as sidelaps, which disappears during stronger shaking (Rogers and Tremblay, 2010). It is then worth looking at how significant this effect has been in past experiences.

Maybe the first hint available for this is provided in the work by Goel and Chopra (Goel and Chopra, 1997). The authors reported that the tested steel moment frames did not show any significant change in natural period with the amplitude of shaking (such was not the case for concrete moment frames due to cracking). Since then, plenty of articles have compared the results from ambient analysis to those during seismic or other extreme events. In Kohler et al., measurements in a 17-story steel moment frame building showed a 12% reduction in period during ambient excitation compared to the period captured during the 2003 Encino Earthquake ($M_L = 2.9$), and virtually no difference during the 2002 Yorba Linda Earthquake ($M_L = 4.7$) (Kohler et al., 2005). In Liu and Tsai (Liu and Tsai, 2010), the difference between ambient testing and the period during the 1999 Chi-Chi Earthquake ($M_w = 7.6$) was of about 9% for a 30-story steel building (again the value during ambient vibrations being shorter). Meanwhile, when compared to a Typhoon event, the shortening effect was found to be of about 1%. A study of reinforced concrete buildings in China by Shan et al. found that the natural period of buildings changes through the years and different testing conditions (Shan et al., 2013). In fact, in one of the buildings the change in natural

frequency between ambient vibration tests 2 years apart was larger than the one during an aftershock event.

As for forced vibration experiments, Trifunac found no significant difference in a 9-story reinforced concrete building compared to ambient vibration tests, even if the change in vibration amplitude from ambient to forced vibration was of 6 orders of magnitude (Trifunac, 1972). However, a difference of about 4% was observed on a mid-rise structure with a mixed system.

No comparison has been made for metal buildings or low-rise construction in general. However, from previous modeling attempts (Bajwa, 2010; Gryniewicz et al., 2021; Wrzesien et al., 2015) there is evidence that including diaphragm action with values taken from the literature can lead to much improved estimates of deflections to service horizontal loads. This is notable because it gives credibility to the point that cladding could provide stiffness even when the structures are subjected to significant displacements, and that it is not an artifact of low level of vibration.

Perhaps the most compelling case can be seen in Sparks and Sockalingam (Sparks and Sockalingam, 1988). Looking into the potential of stressed skin design, a metal building was tested by a rotating, eccentric mass placed in different bays (Sockalingam, 1988). Modeling the structure as a simple N-DOF system with springs representing both the roof and endwall stiffnesses, after calibration to the experimental results, stiffnesses G' of $11.5kip/in$ and $9.1kip/in$ were found for the walls and roof respectively. These values are reasonable and in-line with what could be obtained analytically through the equations studied in previous sections. It's important to note as well that the measured period was $0.22s$, which is much smaller to what both the Equation in ASCE-7 or Smith and Uang would predict.

Consequently, the results by Kumar et al. ([Kumar et al., 2020](#)) are indicative of the natural period for larger levels of vibration, and ambient vibration testing is a viable way to not only obtain the dynamic properties of metal buildings, but also to calibrate and evaluate the actual stiffness of different cladding systems. The measured period could be at most 10% shorter than during a seismic event in a worst-case scenario, which is still small (and conservative for design purposes), especially compared to current predictive equations.

Chapter 3

Methodology

3.1 Introduction

In the previous chapter we discussed the common assumptions made when modeling metal building systems, and in particular how Smith and Uang developed their synthetic data set that led to a new period estimation equation. Given that the tests by Kumar et al. seem to put some of these assumptions into question, it was decided to run a new set of experimental tests that – coupled with analytical modeling of the structures – could lead to a better understanding of what contributes to the natural period of these buildings and whether our assumptions are accurate. As mentioned in the previous Chapter, ambient vibrations have been used before to characterize structures, and so it was deemed appropriate to do the same in this project. Of particular interest was whether non-structural elements (i.e.: roof and wall cladding) was contributing to the measured stiffness.

With this in mind, it was decided to do ambient vibration test during different stages of construction, in order to be able to isolate the behavior of the different components: primary and secondary framing on one side, and wall and roof cladding on the other side. Comparing the results obtained during each construction stage could then provide valuable information on how non-structural elements are affecting the response.

In order to assess the accuracy of the assumptions made for design, for each test in each stage

an associated analytical model was developed in SAP2000 and then updated. If necessary, this model could be procedurally calibrated after each test in order to better quantify the accuracy of our bare frame modeling approach, and also the contribution of the cladding to the stiffness of the fully built structure.

This Chapter then focuses on describing in more detail the required tools needed to perform this evaluation. First, the methods used to extract modal information from ambient vibration tests (Operational Modal Analysis) will be discussed. Then, an overview of the test setup will be discussed describing the equipment and the data gathering approach. This is followed by a detailed description of how the buildings were modeled in SAP2000. Finally, a description of the tested buildings is provided, along with an overview of which stages of construction were tested for each of them.

3.2 Operational Modal Analysis

3.2.1 Background and Justification

As a significant portion of this work is devoted to experimental testing and system identification using ambient vibrations, the purpose of this section is to provide an overview of the method used to extract natural periods and mode shapes of the tested buildings¹. This method falls under the umbrella of what is called Operational Modal Analysis (OMA), as it doesn't require any external excitation. Instead, the response of the structure to the natural source of vibrations it is subjected to during service (e.g.: wind, traffic, human activity, etc.) is used by itself. Since the input isn't given or measured, the methods can also be referred to as Output-Only.

¹This chapter borrows heavily from *Santiago Bertero, Pablo A. Tarazaga and Rodrigo Sarlo, "In Situ Seismic Testing for Experimental Modal Analysis of Civil Structures"* (Under Review).

This is possible under the assumption that ambient vibrations take the shape of a white noise, whose main characteristic is carrying the same energy across the whole frequency band. Working in terms of the Power Spectral Density (PSD) of a signal, this means that the PSD of the input $G_{xx}(i\omega)$ is constant for every frequency ω . Then, the PSD of the output $G_{yy}(i\omega)$ is related to G_{xx} via the Transfer Function $\alpha(i\omega)$

$$G_{yy}(i\omega) = \|\alpha(i\omega)\|^2 G_{xx}(i\omega) \quad (3.1)$$

The Transfer Function is what defines the structural response to any input, and it is defined (for a 1-DOF system) as

$$\alpha(i\omega) = \frac{1}{\omega_n^2 - \omega^2 + 2i\zeta\omega_n\omega} \quad (3.2)$$

where ω_n is the natural frequency of the structure and ζ is its damping ratio. Note that, if damping is small, the above expression reaches its peak when $\omega \approx \omega_n$. Then applying the white noise assumption it follows that

$$G_{yy}(i\omega) \propto \|\alpha(i\omega)\|^2 = \frac{1}{(\omega_n^2 - \omega^2)^2 + (2\zeta\omega_n\omega)^2} \quad (3.3)$$

which means the the response of a structure to white noise shares the same poles as the transfer function, and would have peaks at the same frequencies (the natural frequencies of the structure). Then, by looking at the response of a structure to ambient vibrations in the frequency domain (G_{yy}) it is possible find the natural frequencies of a structure as the peaks in the PSD. Figure 3.1 shows an example from the testing carried out by Kumar et al. (Kumar et al., 2020). In the plot the first two peaks at $2Hz$ and $2.5Hz$ can be identified,

which based on the result above are then the first two natural frequencies in the direction of analysis. Other peaks can also be seen which are related to higher order modes, which we won't discuss here. Also, note that sensors 1 and 3 (S1 and S3)) do not peak along with the rest of the sensors at $2.5Hz$. This would imply that the sensors were placed at nodal points. It is possible, then, to obtain a rough estimate of the mode shape by looking at the ratio between the values of each sensor at a given peak or natural frequency.

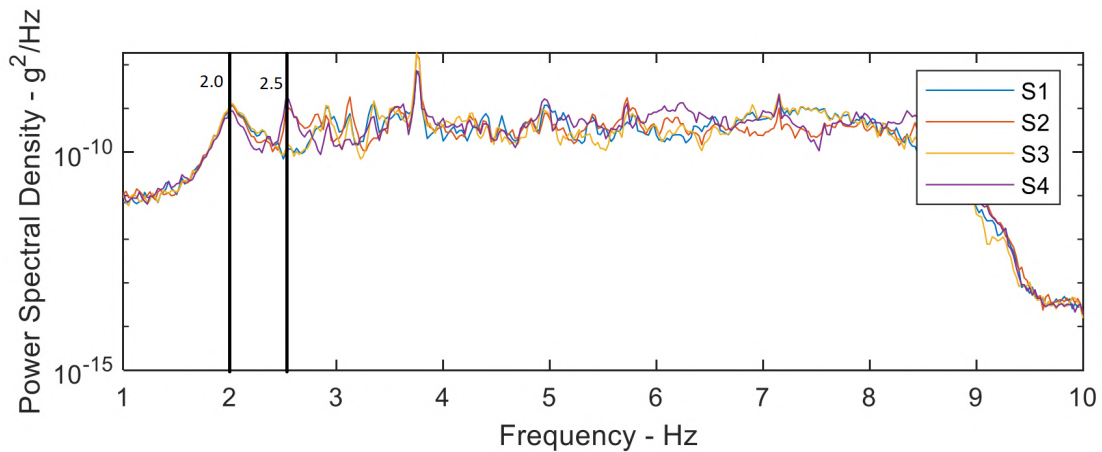


Figure 3.1: Example Power Spectral Density, obtained via ambient vibrations, showing peaks at $2Hz$ and $2.5Hz$: the first two natural frequencies of the structure (Kumar et al., 2020).

Given that the Power Spectral Density is related to correlation ($R_{yy}(\tau)$) through the Fourier Transform (Brinker and Ventura, 2015), it is possible to identify the natural frequencies in the time-domain as well, a methodology that will be explained in the following subsection.

3.2.2 State-Space Representation and Subspace Identification

One of the most popular algorithms, the Subspace Identification (SSI) method, is one of such time-domain techniques and has been implemented successfully in many civil structure case studies. It is popular due to superior performance with noisy measurements and complex systems (e.g.: those with closely-spaced modes). In the most general case, SSI algorithms

assume a physical system can be represented by the state-space form

$$\begin{aligned}\mathbf{x}_k &= \mathbf{A}\mathbf{x}_{k-1} + \mathbf{B}\mathbf{u}_k + \mathbf{w}_k, \\ \mathbf{y}_k &= \mathbf{C}\mathbf{x}_k + \mathbf{v}_k.\end{aligned}\tag{3.4}$$

The first equation describes a vector of system states \mathbf{x}_k which, at time instance k , is determined by the states at the previous instance plus contributions from deterministic and stochastic input sources, \mathbf{u}_k and \mathbf{w}_k . The second equation defines the measurement output vector \mathbf{y}_k as a transformation of system states plus stochastic measurement noise \mathbf{v}_k . The transformation matrices \mathbf{A} , \mathbf{B} , and \mathbf{C} are referred to as the system, input, and output matrices, respectively. The stochastic components \mathbf{w}_k and \mathbf{v}_k are both stationary, ergodic, and gaussian random processes. The reader is directed to ([Overschee and De Moor, 1996](#)) for more details.

Variations in SSI implementations are distinguished primarily by the definition of the subspace matrix of system measurements. In addition, by removing the deterministic inputs (i.e. $\mathbf{B} = 0$), most implementations can be adapted from input-output (EMA) to output-only identification (OMA). Below, the *covariance-driven* SSI approach (SSI-Cov) will be discussed briefly.

Covariance-driven Stochastic Subspace Identification (output-only)

As the name suggests, SSI-Cov works with correlation functions or covariances. One feature of its formulation is that it lends itself well to estimating modal parameter uncertainties, which are useful tools for judging the performance of the algorithm. The output-only SSI-Cov algorithm was taken from Peeters and De Roeck ([Peeters and De Roeck, 1999](#)). In this case, no deterministic inputs are assumed, so the underlying state space model in equation

3.4 can be simplified by setting \mathbf{B} to 0. The output covariance matrix can be estimated as

$$\hat{\mathbf{H}} = \mathbf{Y}^+(\mathbf{Y}^-)^T, \quad (3.5)$$

where

$$\mathbf{Y}^+ \equiv \frac{1}{\sqrt{j}} \begin{bmatrix} \mathbf{y}_{s+1} & \mathbf{y}_{s+2} & \cdots & \mathbf{y}_{s+j} \\ \mathbf{y}_{s+2} & \mathbf{y}_{s+3} & \cdots & \mathbf{y}_{s+j+1} \\ \vdots & \vdots & \ddots & \vdots \\ \mathbf{y}_{2s+1} & \mathbf{y}_{2s+2} & \cdots & \mathbf{y}_{2s+j} \end{bmatrix} \in \mathbb{R}^{l(s+1) \times j}, \quad (3.6)$$

$$\mathbf{Y}^- \equiv \frac{1}{\sqrt{j}} \begin{bmatrix} \mathbf{y}_s & \mathbf{y}_{s+1} & \cdots & \mathbf{y}_{s+j-1} \\ \mathbf{y}_{s-1} & \mathbf{y}_{s-2} & \cdots & \mathbf{y}_{s+j-2} \\ \vdots & \vdots & \ddots & \vdots \\ \mathbf{y}_1 & \mathbf{y}_2 & \cdots & \mathbf{y}_j \end{bmatrix} \in \mathbb{R}^{ls \times j}, \quad (3.7)$$

where \mathbf{y}_k is a vector of l sensor outputs at time step k , s is a user-defined number of block rows, N is the total number of samples and $j = N - 2s - 1$.

The matrix $\hat{\mathbf{H}}$ can be decomposed into the product of observability and controllability matrices, $\hat{\mathbf{O}}$ and $\hat{\mathbf{C}}$, approximated via singular value decomposition (SVD) as

$$\hat{\mathbf{H}} = \hat{\mathbf{O}}\hat{\mathbf{C}} = \mathbf{U}\mathbf{S}\mathbf{V}^T \approx \begin{bmatrix} \mathbf{U}_n & \mathbf{0} \end{bmatrix} \begin{bmatrix} \mathbf{S}_n & \mathbf{0} \\ \mathbf{0} & \mathbf{0} \end{bmatrix} \begin{bmatrix} \mathbf{V}_n^T \\ \mathbf{0} \end{bmatrix}. \quad (3.8)$$

It is assumed that singular values greater than the true model order n are zero. Since n is unknown, however, it must be selected by the user. The truncated singular value and left singular vector matrices, \mathbf{S}_n and \mathbf{U}_n , yields an estimate of the observability matrix, given by $\hat{\mathbf{O}} = \mathbf{U}_n\mathbf{S}_n^{1/2}$.

The state-space matrices can be solved from the observability matrix

$$\mathbf{A} = \hat{\mathbf{O}}^\dagger \hat{\mathbf{O}} = \begin{bmatrix} \mathbf{C} \\ \mathbf{CA} \\ \vdots \\ \mathbf{CA}^{s-2} \end{bmatrix}^\dagger \begin{bmatrix} \mathbf{CA} \\ \mathbf{CA}^2 \\ \vdots \\ \mathbf{CA}^{s-1} \end{bmatrix} = \mathbf{IA} \in \mathbb{R}^{n \times n}, \quad (3.9)$$

$$\mathbf{C} = [\mathbf{I}^{n \times l} \quad \mathbf{0}^{n \times ls}] \hat{\mathbf{O}} \in \mathbb{R}^{l \times n},$$

where \dagger denotes the pseudo-inverse and the symbols $\bar{\cdot}$, $\underline{\cdot}$ denote that the last and first block rows have been removed, respectively. Note that the output matrix \mathbf{C} is simply obtained from the top block row of the observability matrix. Neither the observability matrix nor the state-space matrices are unique, but are invariant under linear transformations, always yielding the same eigenvalues and eigenvectors. The system's discrete-time poles are the eigenvalues of the system matrix \mathbf{A} and can be converted to continuous time poles for calculating the natural frequency, damping and mode shapes. It is important to note that implementation of the SSI-Cov requires the user to specify the measurement period (the number of samples N), Hankel matrix block rows s , and number of singular values n .

Uncertainty Estimation

The modal parameter uncertainty was estimated numerically using the algorithm described by Döler and Mevel ([Döhler and Mevel, 2013](#)). The algorithm performs a first order perturbation analysis to estimate how variations in the output Hankel matrix \mathcal{H} propagate to the estimated modal parameters. This requires an empirical variance estimate of this matrix, which is called \mathcal{H}_v . It is calculated using the standard variance from the sample mean formula

(assuming zero mean)

$$\Sigma_{\mathcal{H}} = \frac{1}{n_b(n_b - 1)} \sum_{j=1}^{n_b} (\text{vec}(\hat{\mathcal{H}}_j) - \text{vec}(\hat{\mathcal{H}}))(\text{vec}(\hat{\mathcal{H}}_j) - \text{vec}(\hat{\mathcal{H}}))^T, \quad (3.10)$$

where $\text{vec}(\cdot)$ converts a matrix to a vector. In this case, \mathbf{y} is divided into n_b equal segments and the subspace matrix observation $\hat{\mathcal{H}}_j$ is computed from the j th segment as described in equations 3.5 through 3.7, with $N_b = N/n_b$ total number of samples. From \mathcal{H} , the standard deviation estimates for each of the modal parameters (σ_f, σ_ζ , and $\sigma_{\mathbf{u}}$) can be computed (Döhler and Mevel, 2013). The number subspace matrix observations n_b are chosen by the user and must be small enough to ensure that the observations of $\hat{\mathcal{H}}_j$ are statistically independent, yet large enough to yield an accurate sample variance. It has been observed in literature (Reynders et al., 2016; Sarlo et al., 2018) that the standard deviation estimates are not particularly sensitive to the choice of n_b . The formulation above assumes that the n_b segments of \mathbf{y} are statistically independent realizations of white noise excitation to the system.

3.2.3 Process Automation

From the previous section it follows that the algorithm is parametric in nature and, in particular, it is impossible to know what model order n to use. Then, the method requires extracting the poles assuming different model orders. It is expected that structural modes would be systematically identified with little variation along a wide range of selected values of n . On the other hand, non-structural or spurious modes would not be consistently identified as the model order changes. With this in mind, the selection of identified structural modes is usually done through a stabilization diagram, where the identified poles are plotted for different model orders and are classified as stable or unstable depending on the change

compared to the previous estimate. Figure 3.2 shows an example of such stabilization diagram. Poles classified as stable can be seen as blue dots; Poles classified as unstable (change in frequency compared to previous order model larger than 1%) can be found as red crosses; and Poles classified as “damping unstable” (when the change in damping ratio is larger than 5%) are shown as blue circles.

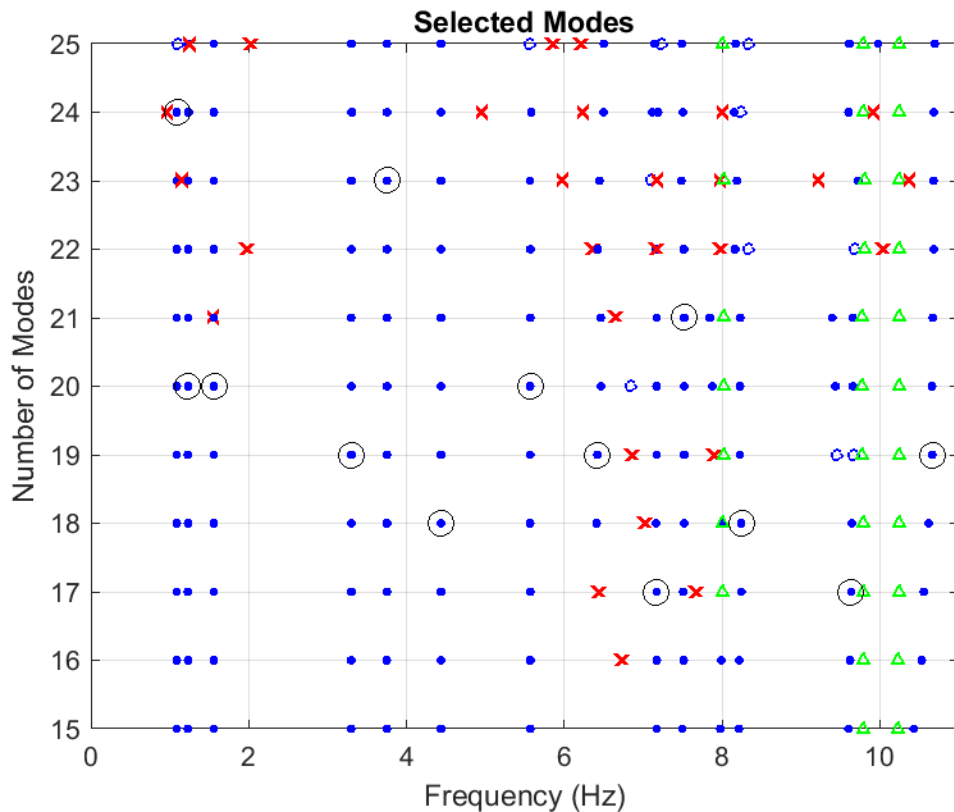


Figure 3.2: Example Stabilization diagram.

The stabilization diagram is a great visual tool for identifying which modes are likely to be structural, but it would still require manual identification and selection of the of the final natural frequency and damping (at which model order the values are taken). Sarlo et al. developed an automatic feature extraction algorithm based on work done by Reynders et al. (Reynders et al., 2012; Sarlo et al., 2018). This method is based on a clustering approach. First, the stabilization diagram is cleared by setting “hard validation criteria”

which separates likely structural modes from spurious mode. This can include, but is not limited to, modes with very low or negative damping ratio (which are the result of noise and not structural properties) or those that stem from an unidentified harmonic load. The latter can be measured by using the Spectral Kurtosis (K_Y) as done by Antoni ([Antoni, 2006](#)).

Then, a set of “soft validation criteria” is defined by creating a distance measure between mode estimates, accounting for both the difference in frequency and the Modal Assurance Criterion Value (MAC) ([Allemang, 2003](#)). Those estimates close together can then be clustered in hierarchical fashion, by grouping clusters until the distance between clusters reaches a user defined value. Then, after discarding outliers (identified due to their large variance in their frequency and damping estimates) a new clustering approach is followed, after which the largest clusters (which have within different estimates of the same mode) are chosen as representative of the structural modes. From those clusters, the estimate with median damping is chosen for the final frequency and damping values of a given mode.

If following this algorithm, then the stabilization diagram is only used as a visual aid, and “unstable” modes may be selected as mode estimates. However, results generally agree between both methodologies, while expediting the process.

3.3 Testing Procedure

Having described the algorithms used to extract modal information from data, this section will discuss the instrumentation setup and the process in which acceleration data was obtained for the different buildings tested. Since the main goal of this research was validating the modeling approach adopted by Smith and Uang to develop their fundamental period formula, the focus was placed on finding the modes of metal buildings in the transverse direction (that is, in the direction of the main frames).

The set up itself did not differ significantly from the one use by Kumar et al. (Kumar et al., 2020). In order to obtain the modes of vibrations in the transverse direction, uniaxial sensors where utilized. This, in turn, means that longitudinal modes nor roof breathing modes were able to be captured.

Compared to the previous work, where sensors were sometimes placed on both columns of a given frame line, in all tests in this research the sensors were all placed on the same side. Given the limited number of sensors available, this maximizes the number of frames that can be measured in a single test, increasing the spatial resolution and providing more information for mode shape extraction. This was possible as Kumar’s work showed that, for the modes that were able to be captured, there was no significant difference in amplitude between each column of a given frame line.

Another difference with previous work is that several buildings were tested in different stages of construction. Though this will be discussed in more detail later, the objective was to see whether the dynamic properties of metal buildings change as cladding is installed, whether the roof is providing significant diaphragm action, and whether the assumptions made for modeling of the primary and secondary framing was adequate *before* including the non-structural elements. This last step is crucial, as reducing the uncertainty in the modeling of the framing would provide greater confidence in the calibrated value the stiffness of the non-structural components when updating the model to account for the final, operational stage of metal buildings.

3.3.1 Equipment

Kummar et al. also showed that a wireless setup was as accurate and less expensive than wired equipment, and so the same sensing system was used for this set of tests. Each sensing

location was instrumented with the following

1. A PCB Model 393B04 accelerometer
2. A PCB Model 489E09 signal conditioner
3. An XNode wireless transmission node developed by Embedor Technologies

The different components can be seen in Figure 3.3. The accelerometer is effectively the measurement equipment, converting structural accelerations into a continuous electric signal. The PCB sensor has a high sensitivity of $1000mV/g$ while weighting only $1.80z$, making it ideal to place in difficult to reach places. The sensor has to be connected to a signal conditioner, which both powers up the sensor and also filters the signal. This particular model is capable of amplifying a signal if required to stay within the voltage limitations of the acquisition system. However, for all the tests in this research a 1:1 scale was used. Finally, the conditioned signal is read by the XNode, which contains a 24bit analogue to digital converter, translating the analogue voltage provided by the accelerometer into discrete values at user defined intervals (described by the sampling frequency).

3.3.2 Sensor Placement

In total, up to 5 nodes (understanding by node the full sensing system including the accelerometer, signal conditioner and transmission node) were available. However, most metal buildings have more than 5 frame lines. In order to capture as much information as possible, it was decided to perform more than one measurement per test. For multiple measurements to be able to be merged together, it is required to have a reference sensor that is common to both measurements. This was achieved by keeping at least one sensor in the same location (frame) in between measurements. For example, in a 9 frame building, a full test consisted



(a) Mounted accelerometer (b) Signal conditioner (c) XNode transmitter

Figure 3.3: Typical instrumentation of a frame.

of two different sets of measurements. Frame lines 1 to 5 were instrumented for the first measurement, and frame lines 5 to 9 were instrumented for the second one, as shown in Figure 3.4. This leaves one sensor (Sensor 5 in measurement 1, which is Sensor 1 in measurement 2) working as reference, which is vital for mode shape extraction.

For each measurement, the sensors were placed as close to the beam-column panel zone as possible (See Figure 3.3a). Whenever a scissors lift wasn't available and a ladder had to be used, the sensor could only be placed as high as the topmost girt of the structure. In any case, all sensors were magnetically attached to the frames on the inside of the outside flange. The main reason for mounting the sensors on the outside flange was to keep the sensing direction as horizontal as possible, given that the columns were usually web tapered members with the outside flange standing perfectly upright and the inside flange slanted to the inside of the building. From the mounting location it follows as well that the sensors were measuring accelerations in the transverse direction as mentioned before. No measurements were taken in the longitudinal direction as the period in such direction does not affect the design of metal buildings' interior moment frames, but that of the sidewall frames and bracing

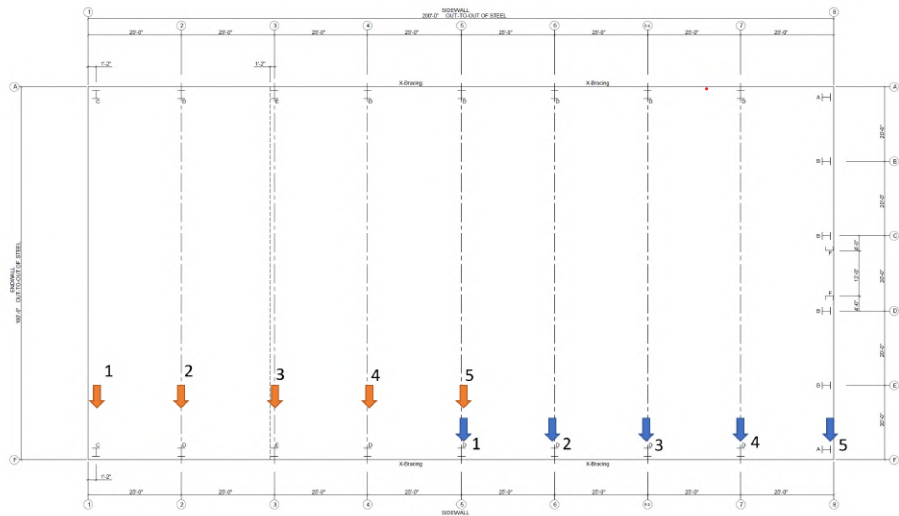


Figure 3.4: Example instrumentation scheme for metal building testing. In orange, sensor locations for the first measurement. In blue, sensor locations for the second measurement.

elements which are out of the scope of Smith and Uang’s formula.

Similarly, the XNodes were also magnetically attached to the frames in each case, as wireless transmission works better when off the ground (Figure 3.3c). The main benefit of using a wireless system was two-fold. One, the lack of wiring to a central system made it simpler to quickly set up the instrumentation of the tested buildings. This was particularly important for buildings that were already in operation, as it reduced the total testing time and – in consequence – the amount of time normal operations were disturbed. Also, since many tests actually consisted of more than one measurement, the lack of significant wiring made it easier to switch sensor locations in timely manner so that the environmental conditions didn’t change significantly from one measurement to another. For reference, the total time inside a building during a typical deployment that required two sets of measurements was on average around *90min*.

Finally, a wireless system permitted setting up tests in buildings with a significant number of partitions, where wiring would not have been possible due to the large distances between

frames (around $25ft$) and the obstructions provided by the walls.

3.3.3 Data gathering, pre and post-processing

A typical measurement time was $300s$, or $5min$ with a sampling rate of $50Hz$. The total time was kept short as the capturing data from as many frames as possible was prioritized over minimizing the uncertainty in the frequency and damping estimations, as that would offer more information in terms of the mode shapes. The accelerometers used are prone to drifting, and so the collected data had to be high-pass filtered before running the system identification algorithms, Since filtering is done via convolution, the start and end of the filtered data has to be cropped out. In the end, approximately $250s$ of data was used to extract modal information at any given time.

Going back to the 9-frame structure mentioned before, the results from running the system identification algorithms need to be merged into a single set of parameters. For the frequency and damping, this was done by taking the average between the frequency obtained by the measurements. The use of reference sensors comes into play when trying to combine mode shape information. Essentially, the mode shape from the first measurement (frame lines 2 to 6) is scaled so that the mode shape value at the reference sensor (in this case, taken as the sensor placed on frame line 5) is equal between measurements. Then, the two 5 by 1 vectors can effectively be merged into a single 9 by 1 mode shape. Note that, for smaller structures where more than one sensor location was repeated, only one of them (typically the one with largest recorded amplitudes) was taken as reference, and for merging purposes the average of the mode shape values after scaling was adopted for the other sensors shared between measurements.

3.4 3D Modeling of metal buildings

Along with the experimental testing carried out, all tested buildings were also modeled in SAP2000 (CSI, 2021) in order to try and predict the experimental results. This model, if necessary, could also then be calibrated and used to explain the discrepancies, if any, between the predicted and measured dynamic properties, from which the different assumptions made in design could be evaluated. SAP2000 was chosen due to its integration with AutoCAD, which streamlines the process of generating a model by importing a 3D-line file, as well as its structural analysis capabilities, especially when it comes to the stiffness formulation of non-prismatic elements and its eigenvalue analysis to obtain natural frequencies, mode shapes and mass participation factors.

Since the work by Kumar et al. and Bajwa on metal buildings with standing seam roofs showed that these buildings exhibit global behavior (Bajwa et al., 2010; Kumar et al., 2020), it was decided to develop full 3D-models for each structure, including the primary and secondary framing, as well as the cladding, as shown in Figure 3.5. Given the low weight of the structures tested, only a first order analysis was performed.

3.4.1 Main framing

The primary framing consists of web tapered beams and columns. Instead of using 2D-shell elements that explicitly model the flanges and web of the frame elements, a linear frame element was used instead (Figure 3.6a). To account for the variable moment of inertia, the non-prismatic formulation from SAP2000 was used. The main advantage of this formulation is that it can handle both discrete changes in section (for example, when either the web or flange thickness changes), as well as the change due to a variable web depth. For the latter, an assumption has to be made regarding the rate of change of the sectional properties (area

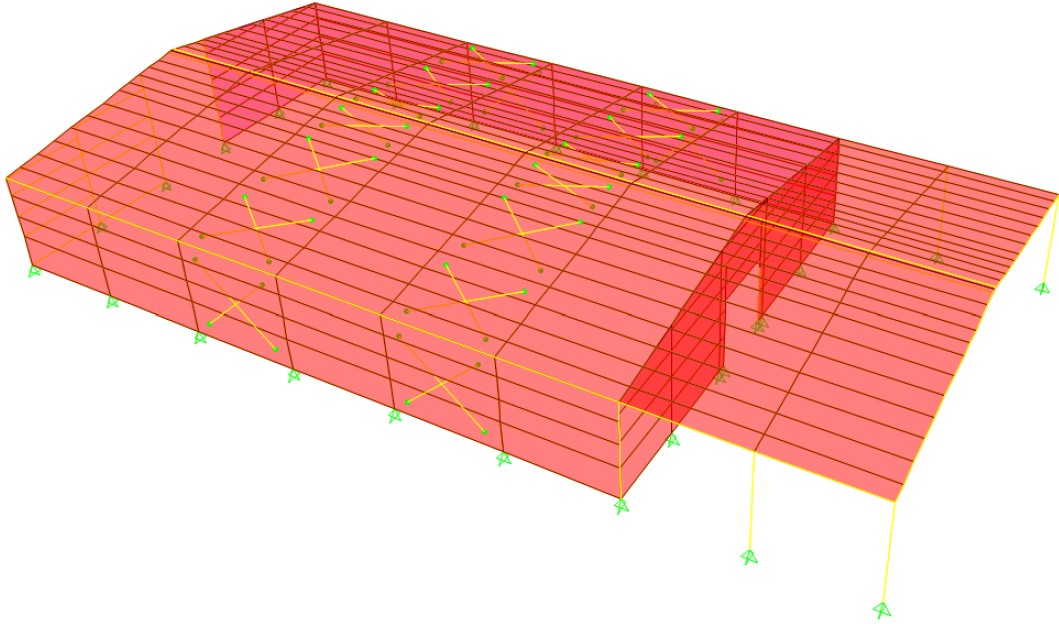


Figure 3.5: Typical 3D model used for analysis of a metal building in its operative stage.

and moment of inertia) in between the specified ends. In the case of metal buildings, where the depth changes linearly, it was decided to use a parabolic function to obtain the moment of inertia along the length, and a linear function for the area.

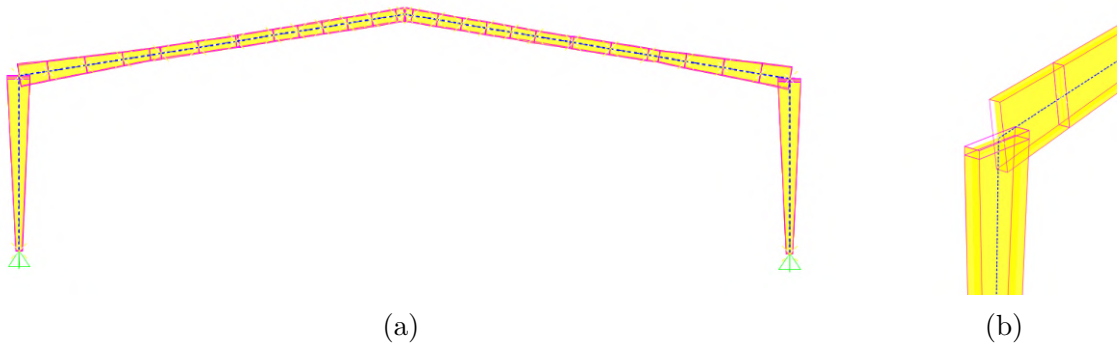


Figure 3.6: Main frame modelling. Left: 2D View of extruded frame. Right: close up view of the beam-column connection.

As discussed before, several modeling options are available for the panel zone at the beam-column joint. For the purpose of this research, it was decided to use a centerline model,

extending the properties of the beams and columns up to the intersection between the “centerline” of the elements (Figure 3.6b). Given that Smith and Uang showed that, on average, the centerline model caused only a 2% difference in the the stiffness of metal building frames (Smith and Uang, 2013), it was decided to forgo a more detailed modeling of the joint. Note, however, that SAP2000 sets by default a rigid endzone of 0.5 times the size of the panel zone, defined as the length in which the extruded frame elements overlap. This value was set to 0 in our analysis.

It’s also worth mentioning that SAP2000 does have some limited capabilities when it comes to modeling panel zones, though not as involved as its building-specific companion ETABS. Essentially, SAP2000 has the option to automatically model the panel zone of a given joint using the scissors model. However, in SAP2000 frame elements are only treated as columns if they are perfectly vertical, and as beams if the reside in the horizontal plane. Given that the rafters in metal buildings are sloped, it is not possible to use SAP2000’s panel zone model directly, which is another reason why it was decided to go ahead with a centerline model. It would be possible to explicitly model the connection, as done by Langley, though in said case the rotational stiffness came from a full Finite Element Analysis of the connection in Abaqus (Langley, 2016).

Finally, some of the simplifications made regarding the geometry should be made. First of all, it is known that when the thickness of the flanges changes (if the thickness of the inside and outside flanges are different), then a shift in centroid occurs. This could be modeled by splitting the frame element at the location of the centroid change, each element following its actual centroid and the connecting the 2 offset nodes with a rigid link. Though said small change in centroid may have some influence on the force diagrams of the beams and columns, it was assumed in this work that its impact on the overall stiffness of the structure was negligible. Ignoring this change results in a significant reduction in the number of nodes

that need to be explicitly model and reduce as well the total number of DOFs in the structure. The main simplification came, however, in the overall geometry of the structure. Since the beams and frames are tapered members, the line connecting the centroids at their ends is not parallel to the overall geometry of the structure. In metal buildings, the outside flanges of the the columns and beams follow the vertical/wall plane and the slope of the roof respectively, even though their centroids do not. It was decided for this research to simplify the geometry and make the non prismatic elements follow the overall geometry of the walls and roofs, as shown in Figure 3.6a. Small changes in geometry should not have significant impact in the stiffness of the frames, as the difference in node location is of at most a few inches when the span can be as long as 100ft. In turn, the prediction should not be negatively impacted. Note that this modeling assumption can be seen in the examples in MBMA's *Seismic Design Guide* (MBMA, 2019b). Also, this simplified geometry eliminates the need of introducing rigid links in the connection of all secondary elements and cladding to the main frame, as they are all now essentially in the same plane.

Finally, for the purpose of making an initial prediction, the columns were assumed to be fully pinned at the base, in line with previous work (Langley, 2018; Smith and Uang, 2013). This assumption was used for an initial estimate, though for some buildings it had to be modified. However, no explicit modeling of the connection or its rotational stiffness was done, unlike the work by Bajwa et al. and Verma (Bajwa, 2010; Verma, 2012).

3.4.2 Secondary framing and bracing

The secondary framing, consisting of cold-formed sections (typically Zee sections for the purlins and girts, and Cee sections for door jambs and other opening were also included in the 3D modeled as continuous prismatic elements. For the purpose of this project, all joints

were modeled as rigid, similarly to the model used by Langley (Langley, 2018). However, in this case it was decided to not model the true location of the secondary elements (e.g., purlins placed on top of the rafters) and avoid the use of rigid links. Modeling offsets can be useful or even necessary when designing a system acting compositely, or when trying to obtain accurate reactions due to an eccentric connection. Note that Langley’s model was built to perform nonlinear response history analyses, and so the level of detail required was higher than for our case, where only the fundamental period of vibration is of interest. Given the relatively low stiffness of the girts and purlins, and that the offset would mainly activate either the low torsional stiffness of columns and beams, or their moment of inertia along the weak axis, the effect of the eccentricities was assumed to be negligible and subsequently ignored. The result of this assumption can be seen in Figure 3.7.

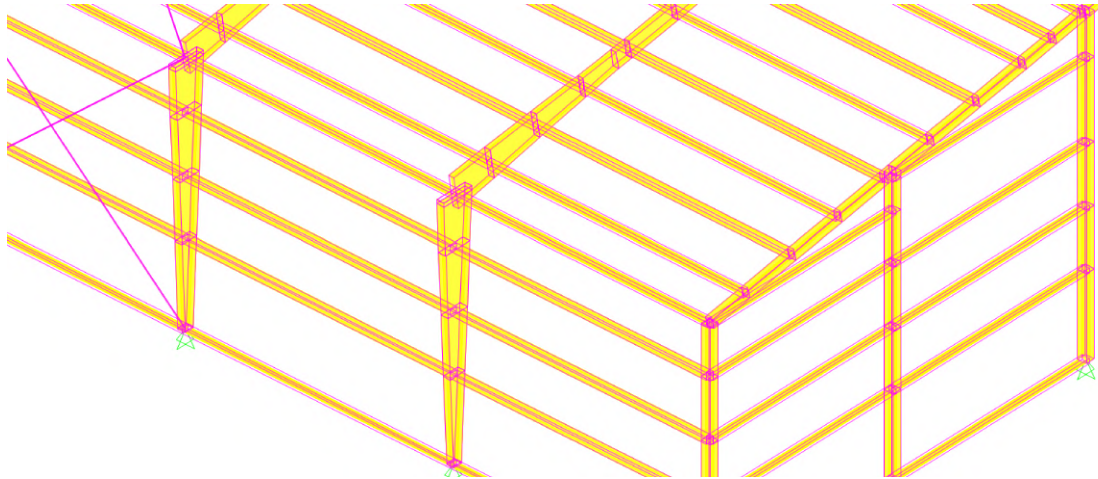


Figure 3.7: Isometric view showing the connection of secondary framing elements to the main frame.

As for the bracing elements/rods, these were modeled to work only along the axis by introducing flexural and torsional releases. Since the model was linear, they were not set up to act only in tension. Instead, it was decided to use a stiffness modifier to account that only one of the 2 crossing braces would be acting at a time. In any case, a sensibility analysis showed the stiffness of the bracing was a not a significant factor in the transverse modes of

vibration of these buildings.

3.4.3 Cladding

Based on the discussion within the previous chapter, it was decided to explicitly model the metal cladding in order to evaluate its potential effect on the structural response. Both the European and American provisions calculate an equivalent stiffness that allows to model the cladding as either an equivalent flat plate, or even as an equivalent truss member (Lutrell et al., 2015). Since using an equivalent flat plate makes it easier to introduce and distribute the dead load across the structure, it was decided to use shell elements for the cladding model. Note that the values provided in the reference are for the full roof assembly (cladding and girts/purlins), while our model explicitly models the secondary framing, and so the values are not directly applicable.

In particular, a thin shell element, which has both membrane and flexural behaviour was chosen. The shell elements had a constant thickness equal to the plate thickness of the metal panels. However, this meant that stiffness modifiers had to be used to more precisely account for the in-plane and out-of-plane stiffness. For the in-plane stiffness, the membrane properties were significantly reduced. For typical walls, based on values available in the literature and the examples showed in the previous chapter it was decided to use – for a first estimate – a effective stiffness that was between 2 – 3% that of the cladding if it were a thin shell with no seams and perfectly connected on all four sides. For the roofs, the initial assumption was that it provided no additional stiffness due to diaphragm action, and so a very small value of $1 \cdot 10^{-5}$ was adopted (this does not mean the roof diaphragm is zero, but that it's fully explained by the purlins given the low values reported by Wei et al.). Meanwhile, their out-of-plane stiffness was increased in such a way that local breathing

modes of the cladding did not interfere with the modal analysis of the main frames. Again, a sensitivity analysis was performed and showed that the first mode of vibration was not sensitive to the change in bending stiffness of the cladding, even when using modification factors of 100.

As for how the cladding was incorporated into the structure, the shell elements were rectangular whenever possible, with triangular elements used when the geometry did not allow for the former. The nodes used were the intersections between the main framing and the secondary framing. This created coarse elements, given that the spacing between frames is usually around $25ft$, as shown in Figure 3.8. Due to this, an automatic shell mesh was used that refined the mesh further. After some sensitivity analysis, prioritizing mostly the time it took to run the models, a subdivision into 8 elements was chosen. However, no real difference was observed in the first mode shapes or natural frequencies of the structure with mesh size, namely when it comes to the deflection of the interior frame elements.

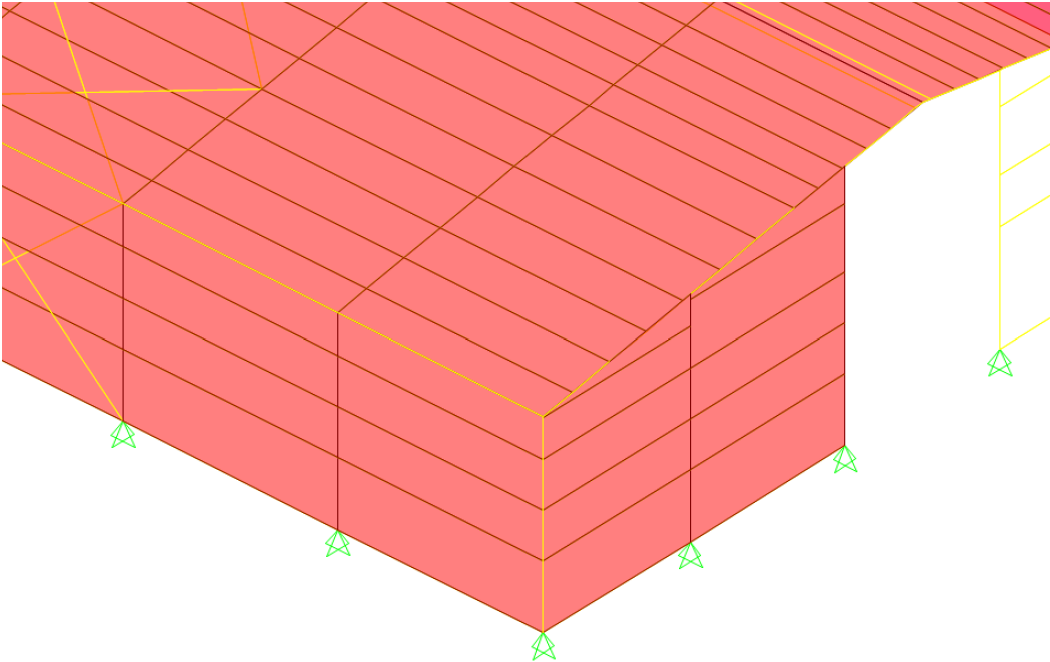


Figure 3.8: Isometric view showing the introduction of cladding as thin shell elements

3.4.4 Other considerations

As mentioned before, the 3D modeling approach described includes effectively the main, web tapered frame elements; the secondary, cold-formed girts, purlins and other framing; the rod bracing when present, and the shell elements representing the cladding. By a process of elimination, it then follows that the bracing elements meant to restrict buckling were not included in the model. It was assumed that they provided no additional stiffness. Also, given the model was kept linear and was built only for the purposes of obtaining dynamic properties and not strength checks, their inclusion would not have had an effect.

Again, the main objective of the models, updated through the different construction stages of each building, was to try and predict their modal properties, and evaluate if they change throughout and why in the case they do. To that end the modal analysis capabilities of SAP2000 were utilized. In order to get the most accurate results possible, the eigenvalue solutions were utilized over the Rayleigh-Ritz method, which is an approximate solution based on the adoption of a shape function for the mode shape.

Another point of interest in this research is whether the assumptions made by Smith and Uang – namely, the flexible diaphragm assumption and the feasibility of obtaining the first mode by using only a 2D model of the main frame – are valid for the purpose of developing a predictive formula for the fundamental period. It becomes valuable, then, to compare not only the experimental results to the prediction given by a 3D model, but also the prediction obtained using a 2D model and two different methods.

A 2D Model of the main frame can easily be recovered from the 3D model by isolating one of the frames, as seen in Figure 3.6a. The mass of the cladding and secondary framing can be assigned to the frame as a linear added mass based on tributary areas, before running an eigenvalue analysis on just the 2D frame.

Similarly, the “refined” approach developed by Smith and Uang (Smith and Uang, 2013) can be followed. This method, which was a calibration based on Rayleigh’s Method, involves measuring the lateral stiffness of the frame by virtue of applying a unit load at the rafter level and looking at the generated displacement at that level, which is the flexibility or the inverse of the lateral stiffness k_{lat} . A schematic example of how the unit load is applied and where to measure the displacement can be seen back in Figure 2.6. In any case, knowing the aspect ratio of the frame, α , the seismic weight tributary to the frame W and the measured k_{lat} , the fundamental period can be estimated as (Smith and Uang, 2013)

$$T_2 = 2\pi \sqrt{\frac{W/g}{k_{lat}}} \left(1 + \frac{\alpha^{2.5}}{425} \right) \quad (3.11)$$

where g is the gravitational constant.

Finally, it should be mentioned that not all the elements mentioned in this section are present in every metal building modeled. Some were measured during construction, before cladding was installed, sometimes even before the secondary framing was complete (mainly the girts). Other oddities were also present at times, such as added masses on top of the purlins, or temporary bracing before the sidewalls were finished. All these things had to be considered on a per case basis, and will be described in more detail when the results for each building are presented.

3.5 Tested Buildings

Up until this point the methodologies used to obtain modal properties from test data, how to perform said tests, and how to model metal buildings to do a prediction have been discussed. In this section, the buildings in which tests were performed will be identified and described

to provide an overview of the kind of structures that were within the scope of this project. Seven buildings were selected in total, five of them identified by MBMA plus two buildings that were being erected in Blacksburg, VA, close to Virginia Tech’s campus. Structural drawings for all seven of them were available, courtesy of Chief Buildings and Varco Pruden respectively. From a review of the design documents it can be concluded that none of the buildings tested had a design snow load above $30psf$, and so snow should not be included in the seismic weight as per ASCE-7. Also, all the buildings were designed for an $R = 3$, implying buildings not specifically detailed for seismic. Given the location and small weight, all building would fall under the “Low Seismic” classification in (Smith and Uang, 2013), and seismic did not governed the design for any of the buildings. Similarly, the design wind speed was between $115mph$ and $120mph$, which is essentially the basic wind speed in ASCE 7-16. Doing a conversion to the ASCE 7-05 wind speeds used by Smith and Uang, all buildings could be grouped in the $85mph$ or low wind speed classification. Finally, Chief Buildings confirmed that no special drift limits were imposed for the design of their frames, and generally speaking wind loads did not control in the design.

Having mentioned some of the common design aspects of the tested buildings, in the following subsections a short description for each of these buildings will be presented. Note that the naming convention throughout this document was chosen by the author.

3.5.1 Building VA-1

Building VA-1 is a standard clear span metal building with a gabled roof located in Blacksburg, VA (Figure 3.9). Intended for storage, its $100ft$ by $55ft$ floor plan was to remain completely open in service. The building had 3 internal frames spaced $25ft$. with an aspect ratio $\alpha = 2.39$ and a mean roof height of $23ft$. The lateral force resisting system in the

longitudinal direction was mixed, with bracing rods in the back sidewall and a portal frame in the front sidewall, the latter allowing for the door openings that can be seen Figure 3.9. The building was tested twice. First on September 24, 2021, once the main framing was completed. Due to disruptions in the supply chain, at the time of testing several girts had not yet been installed, and the temporary bracing was present to provide stability to the endwalls (Figure 3.10). The second test was carried out on February 12, 2022, once the cladding was fully installed and the building was essentially complete.

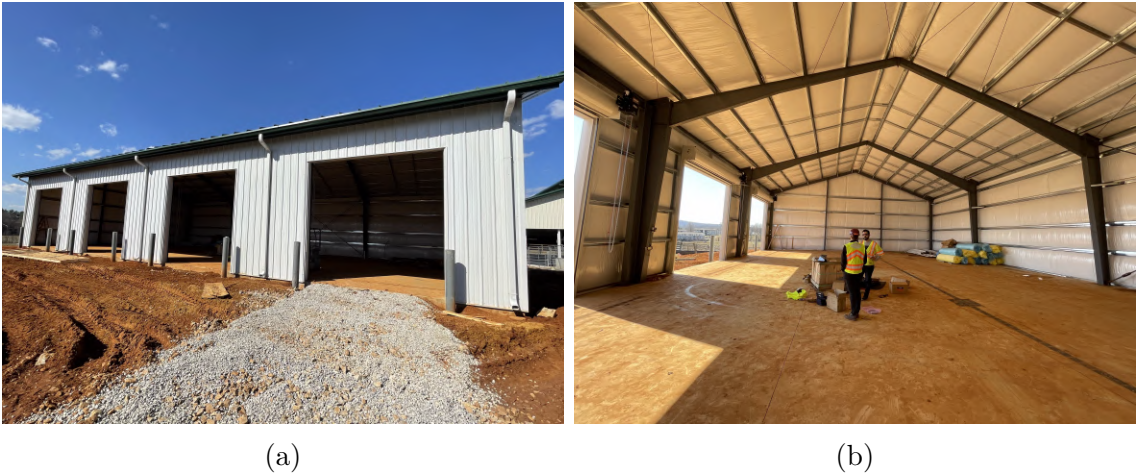


Figure 3.9: Building VA-1 after completion of the cladding installation.



Figure 3.10: Building VA-1 during the the first test on September 24, 2021.

3.5.2 Building VA-2

Across the road from the previous metal building, Building VA-2 is a fairly unique building as it was erected to serve as a barn. As such, the main framing, with a clear span of $78ft$ and a mean roof height of $20.8ft$ ($\alpha = 3.77$) has an almost $6ft$ clerestory on top. If the clerestory is accounted in the mean roof height, a value of approximately $300in$ would be reached. Also, while the main building has a fairly open space of $148ft$ by $78ft$ provided by 7 frames with no partitions connected to the structure, the building has an appendix with office floor space. As a results, all the interior frames could actually be thought of as two bay frames, with one bay having a much larger span (and height) than the other. The reader is referred to the appendix for an elevation view of a typical interior frame.

Building VA-2 was also tested twice. It was not possible to perform tests on the bare frame, the first test on November 11, 2021 occurring instead once the back sidewall and roof panels were installed, but before the endwalls' cladding was put in place (Figure 3.11b). From the figure it's also apparent that a significant number of girts were still missing from the endwalls at this time.

The second test took place on December 16, 2021, after the cladding had been installed on the endwalls of the main building. As shown in Figure 3.11a, at the time of testing the cladding on the appendix had not yet been installed, as they were still installing its interior partitions.



(a) Exterior during the second test.

(b) Interior during the first test.

Figure 3.11: Building VA-2 across different tests.

3.5.3 Building WV-1

Building WV-1 is a clear span metal building with single-slope roof built as an expansion to an existing masonry building in order to serve a storage room for a food services company (Figure 3.12). The building was located in Buckhannon, WV and was fully operational at the time of testing on March 1, 2022. The building has 6 interior frames with prismatic columns, a span of 80ft and a mean roof height of 31.5ft ($\alpha = 2.54$), spaced 26ft , for a total open space of 181ft by 80ft with no interior partitions.



Figure 3.12: Outside view of Building WV-1

The building was tested during normal working hours, and vehicles were driving back and forth across the aisles seen on Figure 3.13a. However, compared to buildings VA-1 and VA-2, which were located in a mostly rural area, building WV-1 is on a relatively small shopping center in Buckhannon, and little to no wind was present at the time of testing. It should be noted as well that this was an extension to an existing masonry building. Though the building is not structurally connected to it, this may still affect the overall stiffness of the structure (Figure 3.13b).



Figure 3.13: Interior of building WV-1

3.5.4 Building WV-2

Only a few minutes away from building WV-1, WV-2 is a clear span, gabled roof metal building spanning $100ft$ ($\alpha = 3.7$), with 9 frame lines distanced $25ft$ from each other with no partitions. The building was located in the outskirts of Buckhannon, WV, at a higher elevation and with no surrounding buildings. Though the building was tested on the same day as building WV-1, the difference in wind speed was apparent.

An interesting feature of this building is that the interior space of the building is actually only 150ft as the endwall on one the sides is located two frame lines in. In turn, two of the frames had no cladding attached to them beyond the roof (Figure 3.14b). At the time of testing the main framing had been fully erected and the cladding installed on the roof, sidewalls and back endwall. However, the front endwall was not finished, missing girts and cladding, in order to allow for construction equipment to get inside the structure (Figure 3.14a). Similarly, the grade slab had not been cast yet.



Figure 3.14: Building WV-2 at the time of testing.

3.5.5 Building NC-1

Building NC-1, located in Maiden, NC, is the main building and storefront for a construction equipment rental company and one of three buildings tested at the site. It's a mono-slope roof building with a clear span of 80ft and a mean roof height of 21.6ft ($\alpha = 3.7$). The building has a total of 7 interior bays with variable spacing, ranging from 16ft to 25ft in the center. Three main characteristics differentiate this building from others tested. First of all, the cladding included a stone veneer at the front endwall. Second, the structural had appendices on several frame lines, sometimes on both sides of the main frame (Figure 3.15). However,

unlike Building VA-2, these were not present at every frame line. Similarly, this building has the most partitions out of the set, with either metal panel or plaster walls spanning the width of the building along 3 different interior frame lines. It is then an interesting case to see the effect non-structural components may have on the modal properties of metal buildings.



Figure 3.15: Building NC-1 during the second (Top) and first (Bottom) tests.

The building was first tested on November 5, 2021, when the framing was already up and and some cladding had been installed on the back endwall. Interestingly, at the time of testing the metal panels that would comprise the roof were bundled on top of the purlins, so the structure already had nominally almost its full dead load mass (Figure 3.15). It then could have provided an interesting case study as the effect of the roof being installed could

be explored.

Due to fire safety detailing requirements, it was not possible to test the structure with the roof installed, as the roof, wall cladding and partitions had to be built simultaneously. The second test took place on February 2nd, 2022, once the building was essentially complete. All the cladding and partitions were up, and most of the work seemed to be focused on architectural aspects.

3.5.6 Building NC-2

Building NC-2 is the second of three buildings in the Maiden, NC site tested. This building was quite standard, with a 150ft by 60ft open floor plan, possible due to five clear span, interior frames with a single slope roof spaced 25ft from each other (Figure 3.16). The most interesting aspect of this building is that was possible to test in three different opportunities, all of them having essentially the same total mass. The first test, on November 5, 2021, was performed once the framing was completely erected. The back sidewall had been installed already, and worked had started on one of the endwalls. Otherwise the structure was free of other non-structural elements. Similar to Building NC-1, at this time the roof panels were bundled on top of the purlins.

The second test was carried out on December 13, 2021, after the wall cladding was completed. These two tests make it possible to evaluate how the change in endwall stiffness could affect the fundamental period. Finally, the third test, done on February 10, 2022, took place once the roof cladding had been installed. With these three tests it was possible to see how the roof and wall cladding affects the dynamic properties, and especially for the former get a better understanding on the diaphragm stiffness provided by standing seam roofing, if any.



Figure 3.16: Building NC-2 during different stages of construction.

3.5.7 Building NC-3

The last building on the set, Building NC-3, is a small metal building intended for storage in Maiden, NC. It's an open metal building with a 100ft by 20ft footprint. 5 frames with a short 20ft span and a mean roof height of 14ft ($\alpha = 1.43$) compose the lateral force resisting system in the transverse direction. The building had a single slope configuration and straight columns, similar to Building WV-1. In this case, the rafters were also prismatic elements (Figure 3.17). The test was performed on December 13, 2021.



Figure 3.17: Building NC-3

3.5.8 Summary

A summary of the main properties of each building can be found in Table 3.1, identifying the main parameters needed to predict their natural period as per the Smith and Uang formula. The seismic weights were calculated on a tributary area basis considering a $1.2psf$ load for the metal roof and cladding, a $3.37lb/ft$ load for each purlin, and the weight of the frame (taken as the total weight of the rafter plus half the weight of each column) as provided in the structural drawings. No snow was included as the design snow loads were below the threshold of $30psf$ set by ASCE-7. This, in turn, makes the comparison between the measured tests and the period used for design easier, as well as resulting in very small seismic weights.

Comparing these seismic weights with the information provided by Kumar et al., it was found that the seismic weights of the buildings in this new set are much lower. However, the estimated load from the deck and purlins was approximately equal (around $2psf$), which means that the disparity is largely explained by the difference in the weight of the main frames. For example, Building IBHS D in Kumar et al. had similar dimensions to Building NC-2 in this report, yet had an estimated seismic weight of $8.3kip$ in large part due to an

Table 3.1: Summary of properties of the buildings tested – design parameters

Name	Length [ft]	Mean Roof Height [ft]	Aspect Ratio α	Seismic Weight W [kips]
VA-1	55	23	2.39	5.3
VA-2	78	20.8	3.74	11.5
WV-1	80	31.5	2.54	9.5
WV-2	100	27	3.70	11.4
NC-1	80	21.6	3.70	7.0
NC-2	60	21	2.86	5.2
NC-3	20	14	1.43	1.8

estimated frame load of $2psf$ (Kumar et al., 2020). From the drawings for Building NC-2, its frame contributed $1.1psf$ to the seismic weight, leading to a much lower value $5.2kip$.

Another important note is that the total load shown here effectively represents a best guess estimate of the situation at the time of testing. However, the load used for design differs and is generally larger. For example, Smith and Uang used a roof dead load of $5psf$ to generate their models (Smith and Uang, 2013). Also, going through the design documents for the buildings tested in this report it was found that collateral loads ranging from $2psf$ to $7psf$ were added, sometimes to account for future installations. MBMA’s *Seismic Design Guide* (MBMA, 2019b) uses a reference value of $4psf$ for the total roof load, plus $2psf$ for an estimate of the main frame weight for an initial design, which would double the estimated seismic weight of these buildings.

Having said that, the set exhibits a good range of clear spans, from $20ft$ to $100ft$, and mean roof heights from $14ft$ to $31.5ft$. Table 3.2 shows as well that there was a good mix of roof types and different partition and appendix situations that allowed the field test to cover a wide range of cases. However, all the buildings are of the clear span type, with no modular buildings in the set. Also, as mentioned before, all buildings were designed for low wind speeds and seismic loads. Since the design was controlled by gravity loads, it would be expected for the buildings to be more flexible than buildings in regions with higher wind or seismic loads.

Table 3.2: Summary of properties of the buildings tested - structural classification

Name	Cladding	Type	Roof	Partitions	Comments
VA-1	Metal Panels	Clear Span	Gabled	None	N/A
VA-2	Metal Panels	Clear Span	Gabled	None	Appendices in every interior frame, Clerestory
WV-1	Metal Panels	Clear Span	Monoslope	None	Expansion to existing building
WV-2	Metal Panels	Clear Span	Gabled	None	Endwall at an “interior” frame
NC-1	Metal Panels	Clear Span	Monoslope	Heavy	Appendices several frames
NC-2	Metal Panels	Clear Span	Monoslope	None	N/A
NC-3	Metal Panels	Clear Span	Monoslope	None	N/A

Chapter 4

Results

In the previous chapter we have gone over the metal buildings that were chosen for this project, as well as the methodology and justification behind both the experimental analysis of the buildings and their 3D modeling with the goal of identifying and predicting the fundamental period. This chapter will focus on presenting the results for each of the tests carried out. In total, 12 tests were carried out, as several buildings were tested during different stages of construction. The order in which they are presented was selected in order to streamline the analysis and extract important partial conclusions in an organized fashion.

Given the heavy number of figures required to properly describe each test (sensor locations, collected data in the time and frequency domain, stabilization diagrams) and the finite element models, only those that were deemed of importance to fully understand the procedures will be presented. As a consequence, some tests will be covered in more detail to explain the common steps taken in all tests and the main conclusions that can be taken from them, while others will simply show the results that are of interest to the project.

4.1 Building VA-1

4.1.1 Bare Frame Test

Experimental Results

The first test on Building VA-1 was carried out after most of the framing had been erected. At the time of testing, several girts were still missing, and temporary bracing was present to stabilize the end walls before the cladding went up. Given that the structure had only 5 frames, a single measurement was performed. A schematic of the sensor locations is shown in Figure 4.1. Note that the figure indicates which frames were instrumented and their numbering. As mentioned before, the sensors were magnetically attached on the inside of the outside flanges, on level with the topmost girt of the building. As one sensor malfunctioned, only those for which data was able to be collected are shown for clarity.

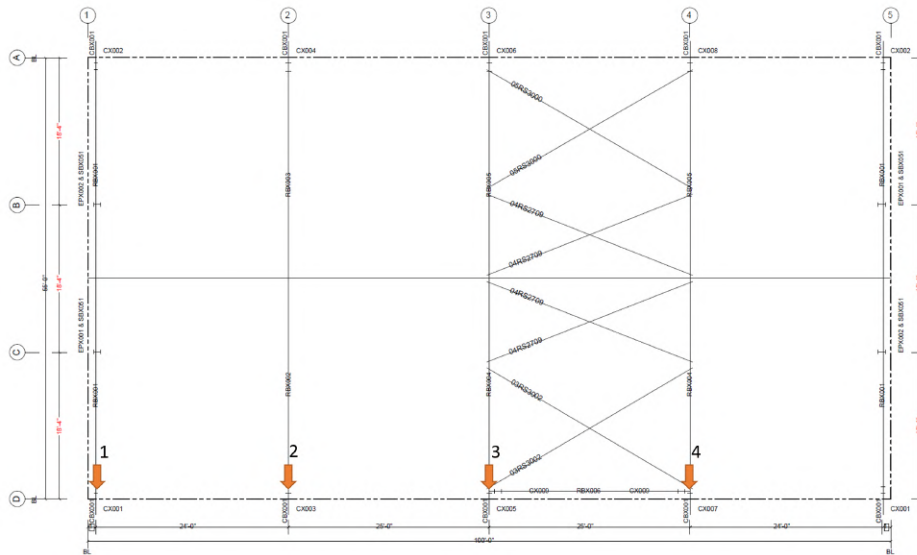


Figure 4.1: Sensor locations for Test 1 in Building VA-1

Figure 4.2 shows the recorded time history after applying a high-pass filter at 1Hz to eliminate low frequency noise, as well as the associated Power Spectrum Density for each sensor. The first thing to notice is the low amplitude of the accelerations in ambient vibration. As mentioned before, the database in Goel and Chopra included buildings with peak accelerations of $0.15g$ (Goel and Chopra, 1997), where here it's below $0.005g$, 30 times smaller. Moreover, it can be seen that the amplitude does not stay constant across the entire test length. From approximately 60 to 150s, there is a noticeable increase in acceleration amplitude, most probably due to larger sustained winds.

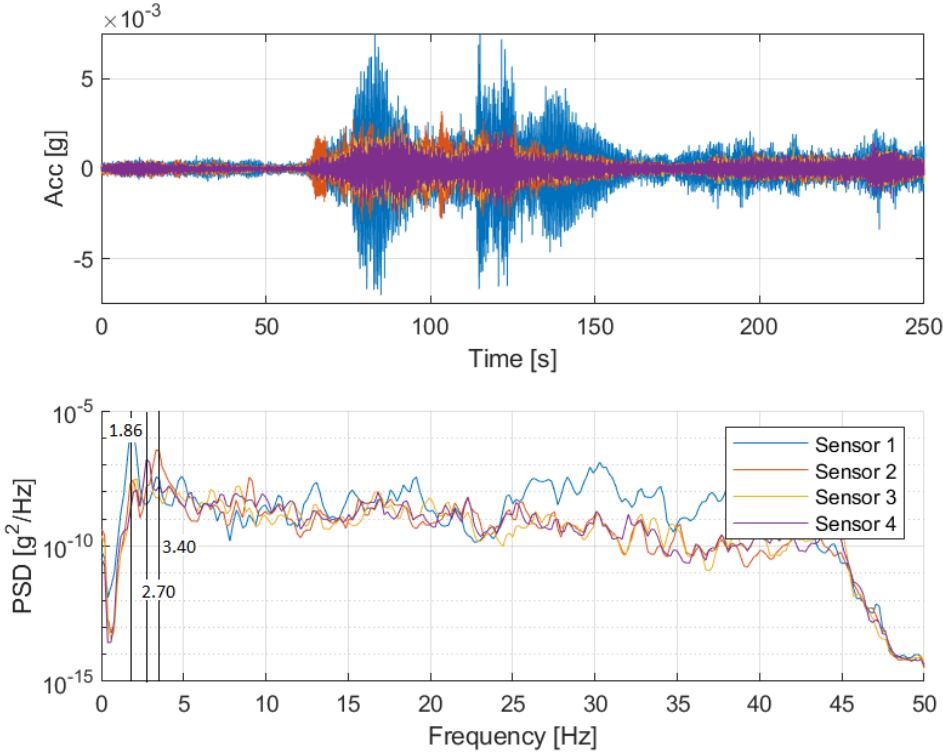


Figure 4.2: Collected data for the first test in Building VA-1

The effect of acceleration amplitude in the response can be seen in what is called a spectrogram, a plot that tracks the frequencies carrying the most energy (shown in red) in time. It can be thought of a time dependent version of the PSD shown in the previous figure, which

is an average or global result for the whole test. Figure 4.3 shows the spectrogram for sensor 3. Two clear horizontal red lines can be seen at around $2Hz$ and $3Hz$, implying that the PSD is peaking at those frequency values (which can be corroborated by looking at the PSD on Figure 4.2). However, the most significant detail is how the line at $2Hz$ is not visible throughout the whole test. Up to the 60s mark the frequency does not stand out. This is an example of how some modes may not be excited strongly enough to obtain a measurable response, especially during short tests.

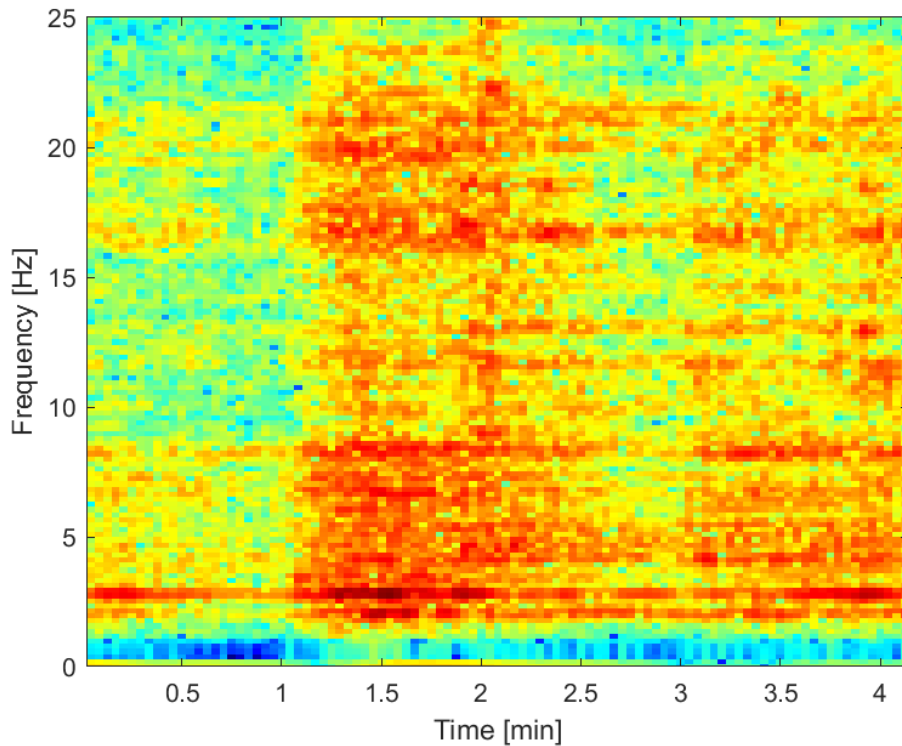


Figure 4.3: Spectrogram of the acceleration data recorded by sensor 3 on the first test in Building VA-1

In any case, going back to Figure 4.2, three peaks can be clearly identified by inspection at around $2Hz$ ($0.5s$), $2.5Hz$ ($0.4s$) and $3.5Hz$ ($0.29s$). Following what was seen in the previous chapter, these would then be 3 natural frequencies of the structure. Some information about the mode shapes can also be identified via inspection. At $2Hz$ ($0.5s$), sensor 1 (located at

the endwall before the cladding went up) shows a much higher peak than the rest of the sensors. Then, it can be assumed that the deflections for this mode are largely concentrated in the endwall. Similar considerations can be made for the mode shapes at around $2.5Hz$ ($0.4s$) and $3.5Hz$ ($0.29s$), which will most probably be dominated by sensors 3 and 4 in the former, and sensor 2 in the latter.

So far the results have only been discussed qualitatively in order to provide some intuition behind the dynamic properties the stochastic subspace algorithm will identify. For reference, in Figure 4.4 the stabilization diagram is shown, where the poles of the system (the natural frequencies) can be seen for a range of model orders n . This stabilization diagram, as mentioned before, is used for visualization purposes only, as a clustering algorithm is used instead to select the final modes.

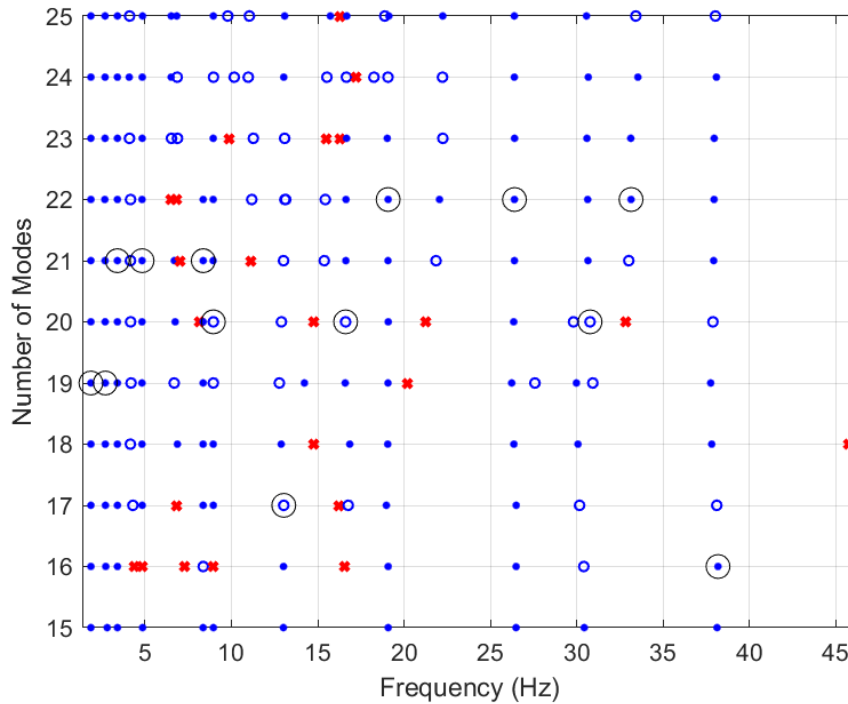


Figure 4.4: Stabilization diagram for test 1 in Building VA-1. Blue dots represent stable poles. Red crosses represent unstable poles, and small blue circles represent unstable modes in terms of damping. The selected modes are circled.

Though several modes can be identified, the limited number of sensors means that reliable mode shape data can only be recovered for a few of them (the lower order ones) before encountering spatial aliasing issues. But, in any case, the 3 frequencies previously mentioned clearly show up as straight vertical lines of stable poles, indicating the these are likely structural in nature. The final estimated natural frequencies for the first three *identified* modes are $1.86Hz$, $2.70Hz$ and $3.40hz$. Note the use of the word *identified*. It's important to remember that due to sensor placement and orientation some modes cannot be captured, such as longitudinal or roof modes of the building. Similarly, given that the right endwall wasn't measured, it is not possible to know from the test data whether it was exhibiting an isolated modes shape similar to what was discussed for the left endwall.

As mentioned before, the algorithm uses a clustering approach to automatically select the natural frequencies and at which model order to select the dynamic properties. The final clusters of the method can be seen in Figure 4.5.

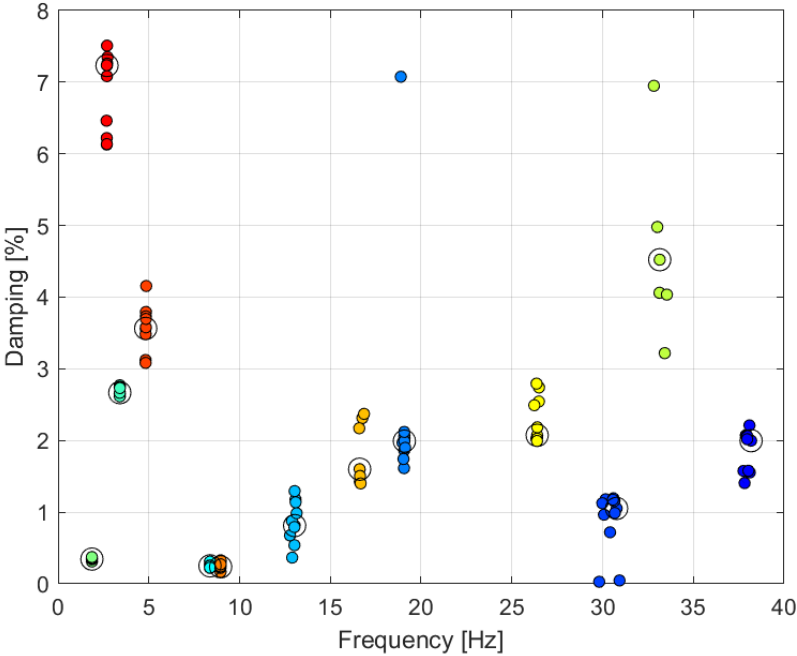


Figure 4.5: Final clusters from test 1 in Building VA-1

In any case, what is important to take away from the procedure is that the first three modes that were extracted from the test had natural periods of $0.54s$, $0.37s$ and $0.29s$. The mode shapes, meanwhile, are plotted in Figure 4.6. Note, then, how the results match the previous analysis based on the PSD of the measured signals. It's important to remark here that Figure 4.6 is only plotting known values of the mode shapes at the measured degrees-of-freedom. First, the black dots at certain beam-column joints indicate locations where sensors were placed. In this test, for example, no sensor was located in the right endwall. Similarly, the mode shape shown is limited by the degrees of freedom measured. Since only uniaxial sensors were used in the direction of the main frames, only said transverse motion can be captured (and drawn). As such, there could be motions in the longitudinal directions that are not being captured by test nor shown in the modeshapes, though results from the analytical models can confirm these are predominantly transverse modes. Finally, it was decided to only show values in measured locations instead of interpolating or assuming a deformed shape for frame lines without sensors. As a result, in Figure 4.6 the right endwall is drawn assuming it does not participate at all in any of the modes. All these considerations apply generically for every experimental mode shape extracted in this chapter.

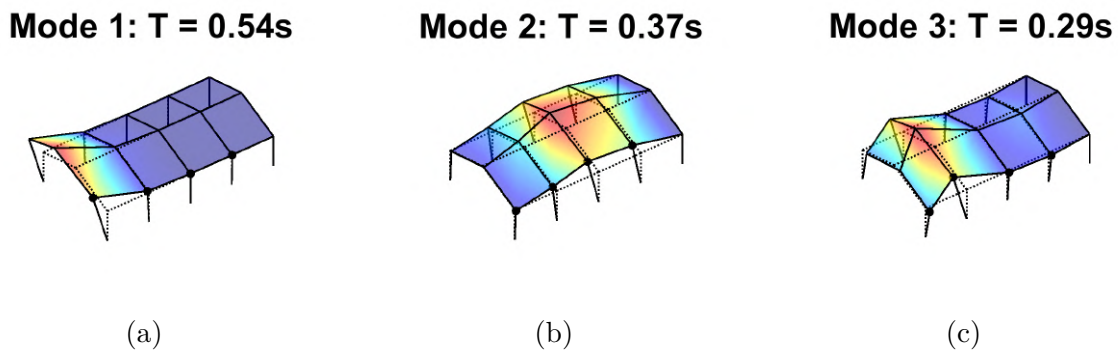


Figure 4.6: Experimental modes from test 1 in Building VA-1

3D Model prediction

In order to identify the effect of nonstructural elements, it is necessary to first reduce the uncertainty in the bare frame model. Otherwise it becomes harder – if not impossible – to know what should be calibrated to match the results, if the frame stiffness or the cladding. Figure 4.7 shows the SAP2000 model for the building, which attempts to match the conditions at the time of testing, accounting for the missing girts and temporary bracing on display in Figure 3.10.

Other than that, the results shown here come from the initial prediction, without any modification of the mechanical properties of the materials. In summary, no calibration was done.

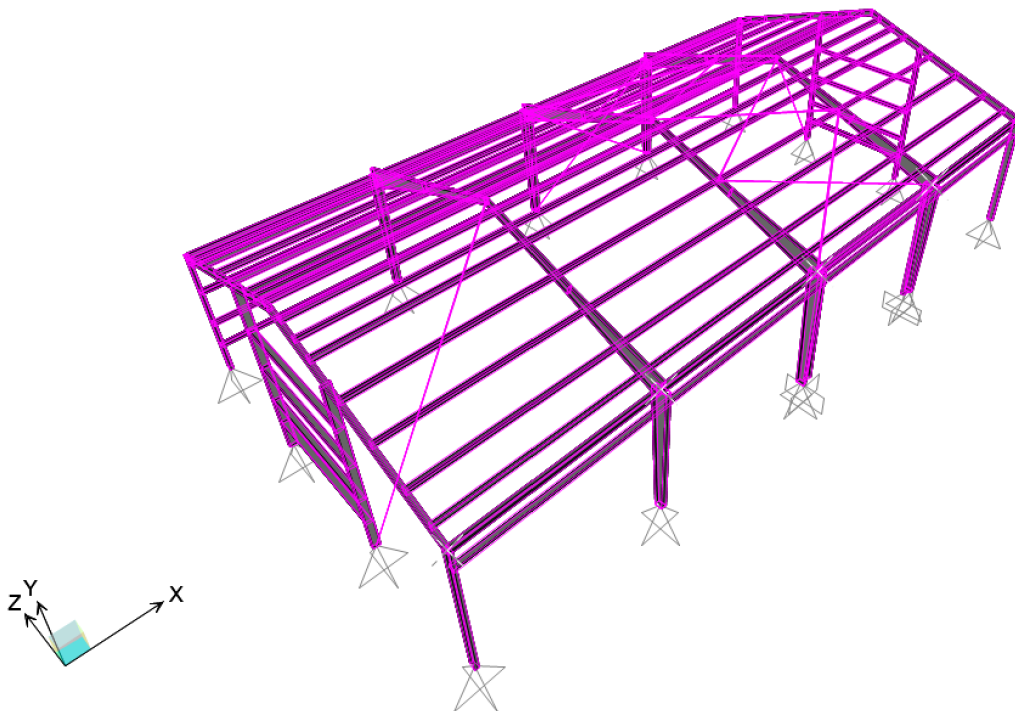


Figure 4.7: SAP2000 model of building VA-1 for test 1

The results from the modal analysis are shown in Figure 4.8, with T being the estimated period and ΔT the percent difference with the experimental results. Only the first modes whose predominant motion is in the transverse direction are presented, but that does not necessarily mean they are the first modes of the structure. In this particular case, the *actual* fourth mode corresponded to the first longitudinal mode with a period of $0.31s$. In any case, four modes are shown, with periods of $0.51s$, $0.50s$, $0.35s$ and $0.29s$.

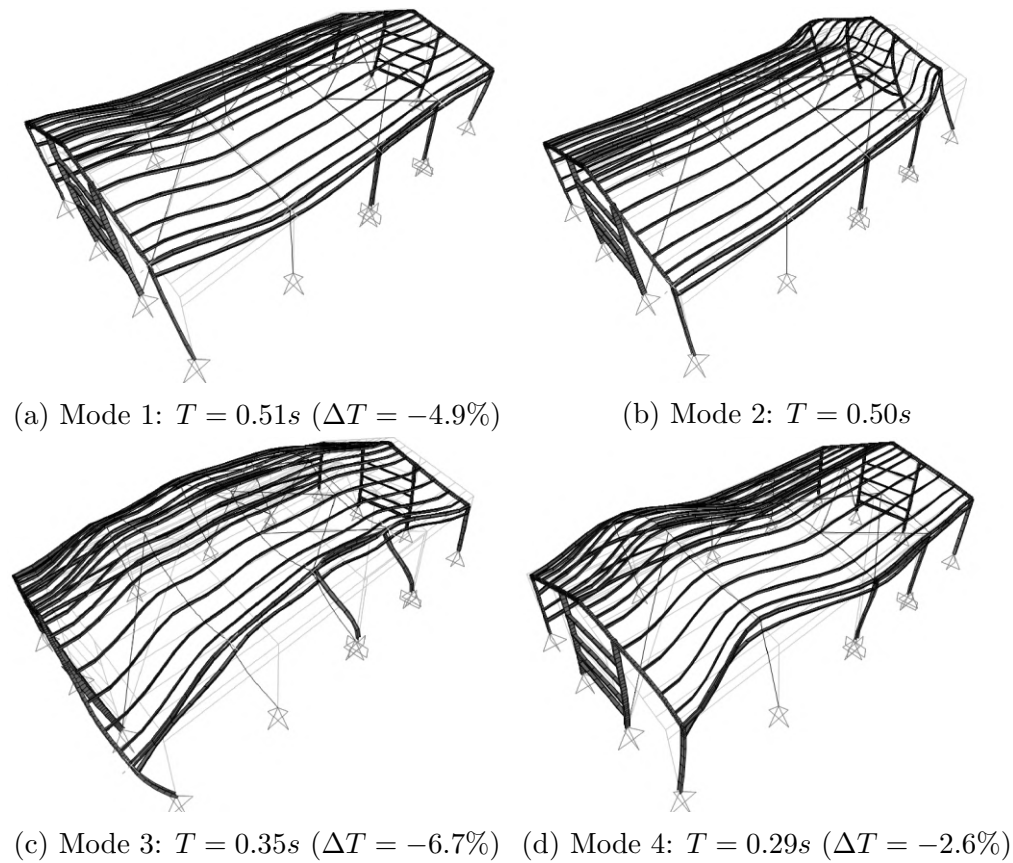


Figure 4.8: Mode prediction from SAP2000 for test 1 in Building VA-1

Comparing the results of the model to the analytical results, a very good match is observed. Mode 1 of both the model and the test have a very similar mode shape dominated by the left endwall, and the difference in period ΔT is 4.8% . Similarly, Modes 3 and 4 for the model are very close in shape to the Modes 2 and 3 obtained via ambient vibrations. The difference

in period was 6.7% and 2.6%. In all cases the model underestimated the period, implying it was stiffer than the actual structure. The results were considered good enough to justify not going through a calibration process.

It must be mentioned, however, that Mode 2 of the model, which consists on the displacement of the right endwall, was not seen during testing. Considering that the mode is localized to a particular frame line, and that there was no (working) sensor located there, it is more likely than not that it wasn't identified by the rest of the sensors as they would have less energy content at this frequency. The mode shape would not have been able to be recovered anyway as the maximum value would be at a place that was not measured. In summary, that mode is believed to exist, but wasn't identified during testing due to limitations of the instrumentation.

Finally, it was discussed before that the modes were found to be very similar in shape between the model and the test data. This usually is a more convincing proof that the structure and the model are behaving similarly, as the frequencies could be similar even if the mode shapes are not. In order to quantify the assertion that these shapes are similar, the Modal Assurance Criterion (MAC) is used. In this case, it's referred to as a crossMAC, as what will be evaluated is the MAC between two different sets of mode shapes. The results can be seen in Figure 4.9.

Each cell in the plot is color coded, with dark red meaning a crossMAC of 1 and dark blue a crossMAC of 0. Ideally, the crossMAC should return approximately the identity matrix. That would mean that the mode shape given by the model and the experimental test are equal to each other, while different modes have no correlation or are approximately orthogonal to each other. Usually, a value of 0.7 is considered good enough for two modes to be considered the same, with values above 0.9 implying a very good correlation.

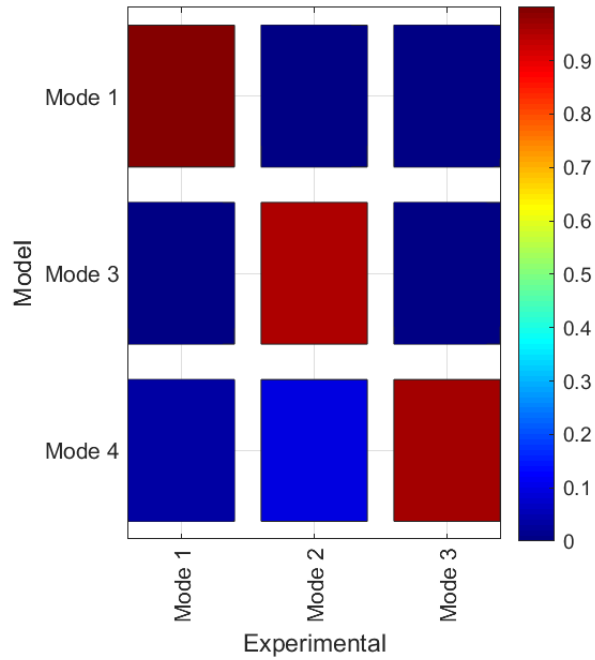


Figure 4.9: crossMAC for building VA-1 – test 1

In this case, it follows from Figure 4.9 that the modes predicted by the model correlate very well with the experimental results, with the lowest value being 0.96 for the second experimental mode. In conclusion, the bare frame model accurately captured what was measured on the field, and could be used for the next stage in the analysis.

4.1.2 Completed Building Test

Experimental Results

The second test took place once all the framing was erected and the cladding on the walls and roof was installed. The sensor locations can be seen in Figure 4.10. It should be noted that for this test there is available data for both end walls as well as the inner frames, which will allow to see the effect the cladding had on the stiffness of the endwalls.

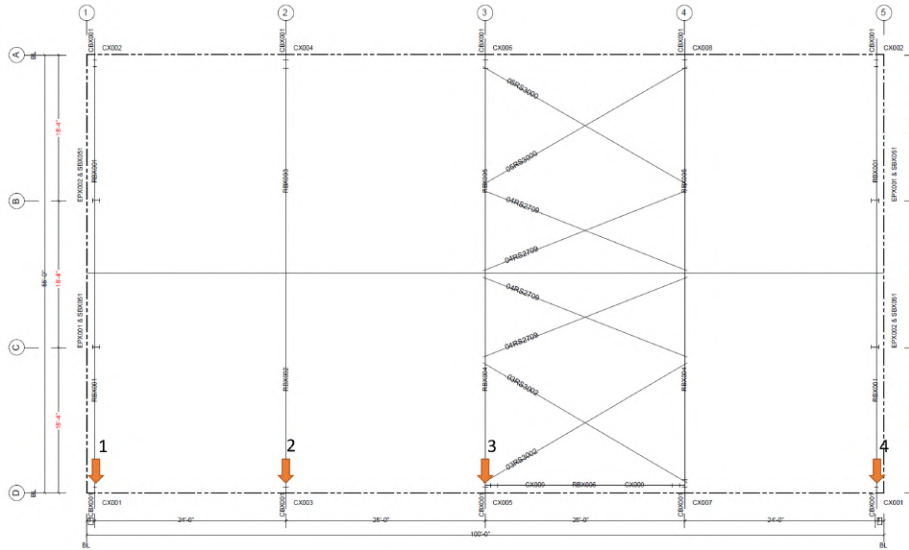


Figure 4.10: Sensor locations for Test 2 in Building VA-1

Figure 4.11 shows the recorded accelerations in each location. Compared to Figure 4.2, the amplitude stays within the same order of magnitude as the previous test, and the same variability with time can be seen. More importantly, looking at the PSD, only a single peak can be seen in the previous range between 0 and $4Hz$. Specifically, when looking at sensors 1 and 4, related to the endwalls, it can be seen that they no longer show a peak around $2Hz$, and generally speaking their energy content is much lower, implying that the endwall cladding added a significant amount of stiffness.

In the end, only a single mode could be confidently identified from the test data, with a natural frequency of $2.35Hz$ ($0.43s$). The associated mode shape can be seen in Figure 4.12. Note that, since frame line 4 was not measured the displacement value for that frame is set to 0, but that does not necessarily represent the actual value. Setting it to 0 over finding an interpolation was a conscious decision made to avoid introducing personal bias into the mode shape estimation. Instead, measured frames can be identified by the black circle at the beam to column connection.

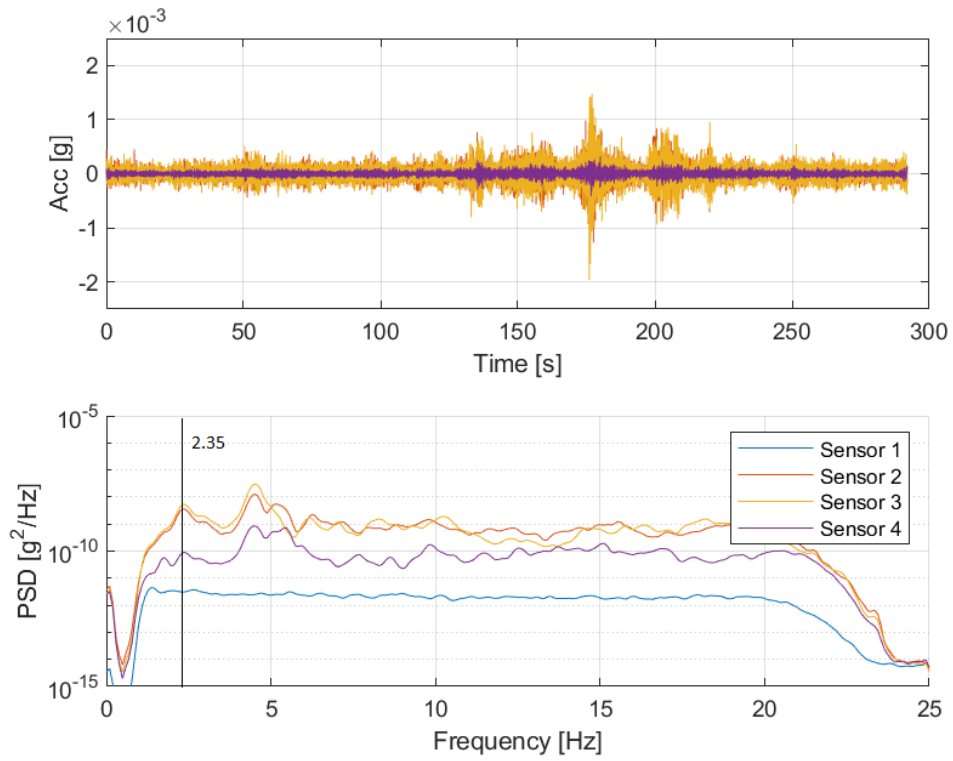
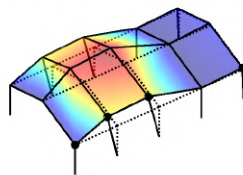


Figure 4.11: Collected data for the second test in Building VA-1

Mode 1: T = 0.43s



(a)

Figure 4.12: First mode from test 2 in Building VA-1

3D Model prediction

Following from the results in test 1, the 3D SAP model was updated to fully represent the structure at the time of testing, by removing the temporary bracing, and adding the originally missing girts. The cladding for the roof and walls was included as well in the form of shell elements as explained in the previous chapter. Following the assumption that Standing Seam Roofs provide little to no diaphragm action, its membrane properties were reduced by 10^5 . Note that this does not mean that there's no diaphragm action at all. The G' value given by the Diaphragm Design Manual (Luttrell, 1965) includes the effect of the purlins in its formulation as what is tested is the complete roof assembly. As such, reducing the stiffness of the shell elements to effectively zero does not imply that there is no diaphragm stiffness, but that almost all the stiffness is being provided by the purlins. As later shown in this Chapter, as well as in Chapter 7, the stiffness of the purlins alone is already around $1kip/in$, which is consistent with the stiffness taken from Wei et al. (Wei et al., 2020). In turn, since the stiffness of the purlins already reasonably agrees with the limited experimental data available, it was considered appropriate to neglect any additional stiffness due to the sheeting alone, which is what is needed for the SAP model.

For the walls, meanwhile, the effective stiffness was considered to be 2% that of a flat plate of identical thickness. The full model is shown in Figure 4.13.

After performing a modal analysis, the most notable difference compared to the previous model was that the modes associated with the endwalls were no longer the ones with longer period. In fact, it would take hundreds of modes for them to appear in SAP, mostly because of several local modes related to the shell elements and the secondary framing. In the end, however, given that experimental modal information did not provide any hints regarding the stiffness of the walls, no real calibration can be done. All that can be said is that the

endwalls are significantly stiffer than the interior framing once the cladding is installed.

Second, as can be seen on Figure 4.14, the structure was predicted to have a fundamental period of 0.42, less than 2% off from the experimental result. The computed crossMAC for the first mode was 0.98, showing an excellent correlation. Thus, for building VA-1 the roof was found to provide no diaphragm action, and the model predicted the response very well.

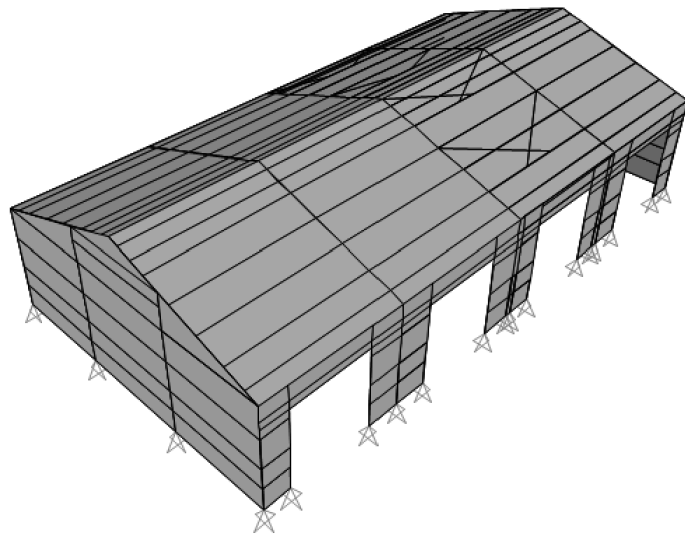
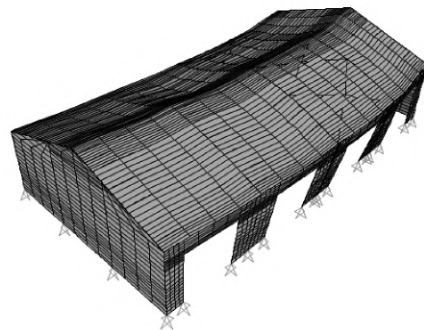


Figure 4.13: SAP2000 model of building VA-1 for test 2



(a) Mode 1: $T = 0.42s$ ($\Delta T = -1.8\%$)

Figure 4.14: Mode prediction from SAP2000 for test 2 in Building VA-1

4.2 Building NC-2

4.2.1 Bare Frame Test

Experimental Test

Building NC-2 was the only metal building for which it was possible to perform tests in all three relevant stages of construction. The first test was carried out after all the primary and secondary framing had been erected. Work had also started on the cladding, with the back sidewall finished and about half of the left endwall installed. As mentioned before, at the time of testing the roof panels were bundled together and sitting on top of the purlins, which means that almost the full weight of the building was already in place. This provided an excellent opportunity to isolate the effect of cladding, as the mass would remain essentially the same for each test, unlike the building VA-1.

Given that the building had 7 total frames, the test consisted of two different measurements linked by reference sensors that stayed in place for both measurements. The sensor locations can be seen on Figure [4.15](#).

Given that measurement 2 includes measurements on an endwall before the cladding was installed, it was chosen to show the collected response from said measurement in Figure [4.16](#). Similar to building VA-1, the first peak at around $1Hz$ ($1s$) for sensor 4 (the right endwall) is orders of magnitude larger than for the rest of the sensors, showing the great flexibility of these walls before the cladding went up. Meanwhile, the interior frames are showing peaks at around $2Hz$ ($0.5s$). These latter peaks were also present in the first measurement, while the peak at $1Hz$ ($1s$) was not.

The identified modes can be found in Figure [4.17](#), with the first mode dominated by the

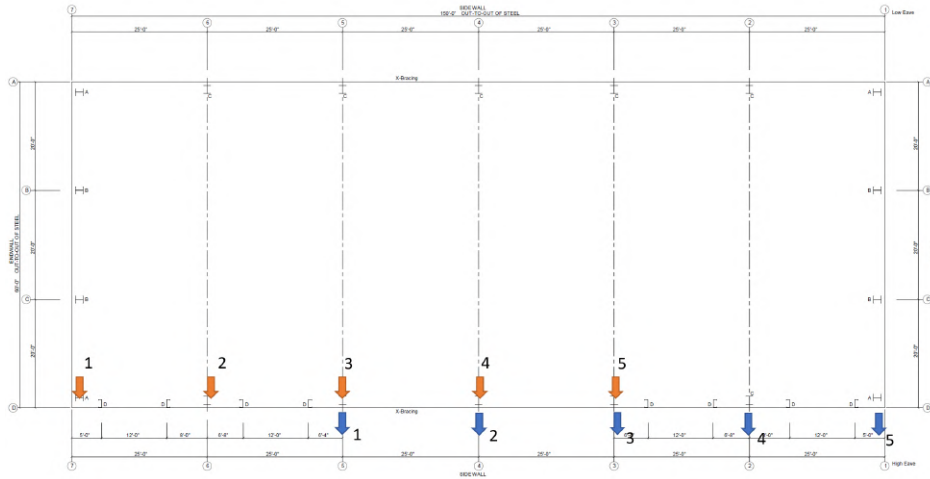


Figure 4.15: Sensor locations for Test 1 in Building NC-2. In orange: measurement 1. In blue: measurement 2.

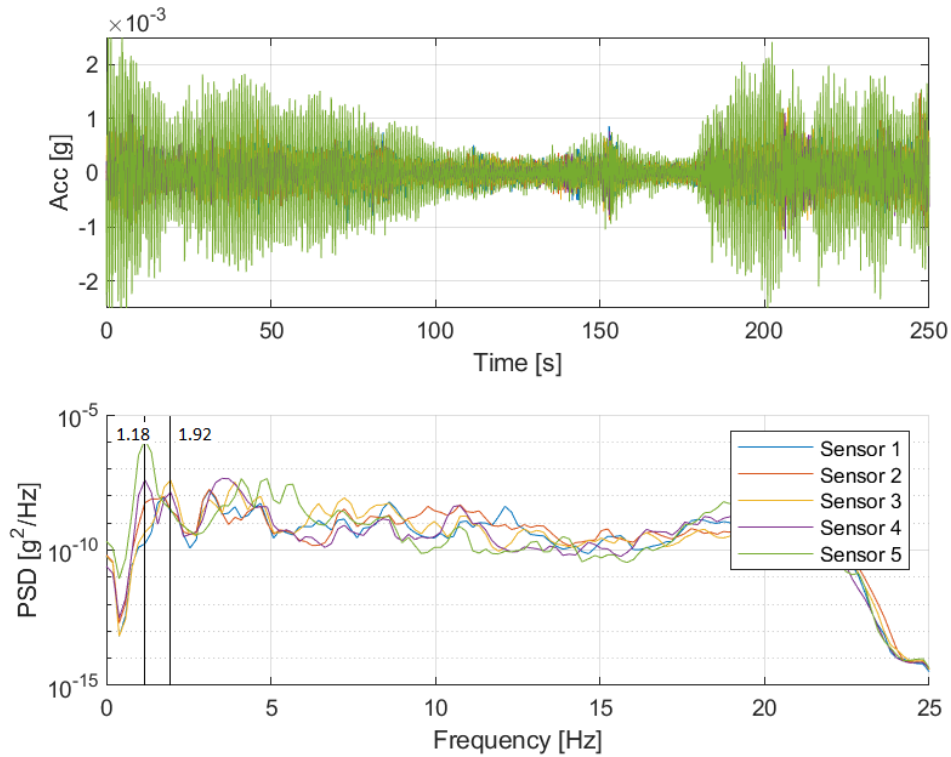


Figure 4.16: Collected data for the second measurement of the first test in Building NC-2

individual movement of the right endwall, and the other two appearing to be representative of a more global, system behavior. Note that in this case a mode shape related to the displacement of the left endwall was not identified, most probably because the partial cladding was already providing a significant amount of stiffness.

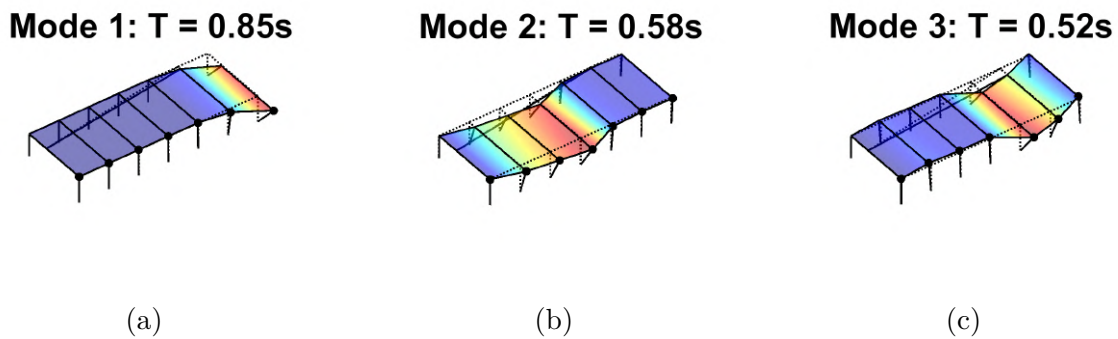


Figure 4.17: Experimental modes from test 1 in Building NC-2

3D Model Prediction

An isometric view of the 3D model can be seen in Figure 4.18, showing the inclusion of the back sidewall and the partial construction of the left endwall. To account for the added mass of the bundled roof panels, an equivalent linear mass was added to the main frame rafters, using the lever rule (i.e., assuming the purlins to be pinned between main frames, solving for the reactions dof a simply supported beam with a concentrated load where the roof panels were bundled provides the distribution factor) to assign distribution factors on an approximate basis given photographic evidence. The choice of modeling the mass directly on the frames instead of the purlins was to avoid introducing irrelevant modes at the purlin level that would make discerning the overall behavior of the structure more difficult.

The resulting mode shapes from the model can be seen in Figure 4.19. The first mode, which is the right endwall mode, did not show the same accuracy as the others, with a 12% overestimation of the period. However, the second and third modes which are the most

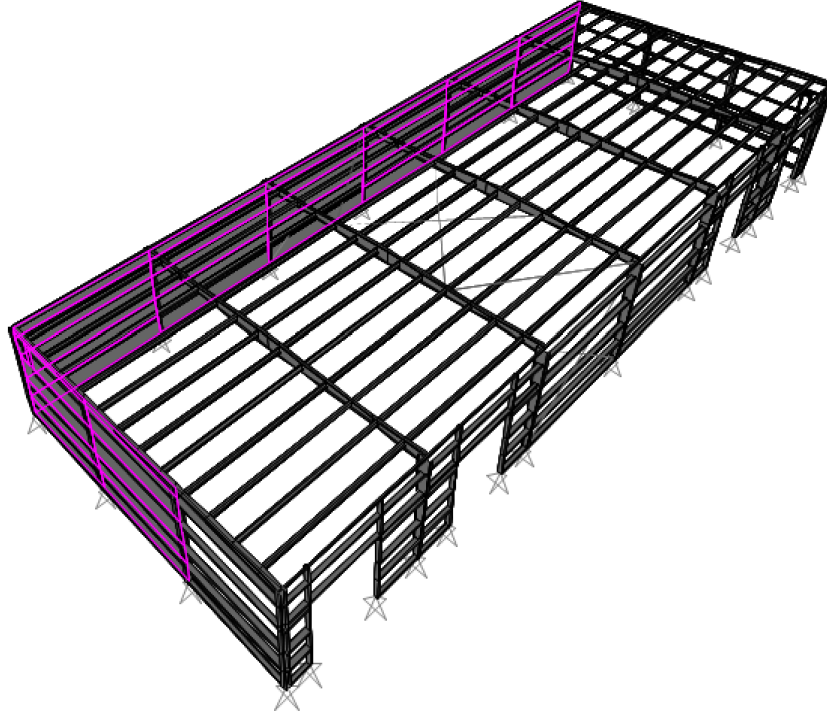


Figure 4.18: SAP2000 model of building NC-2 for test 1

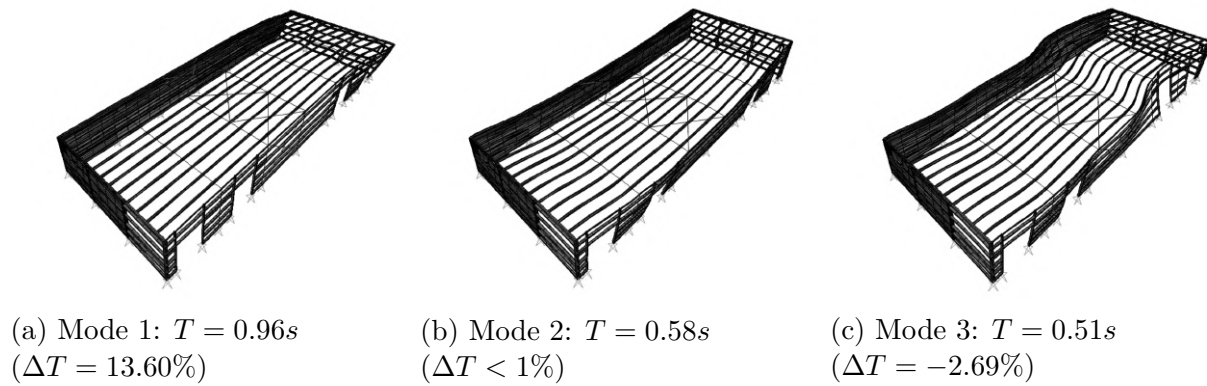


Figure 4.19: Mode prediction from SAP2000 for test 1 in Building NC-2

significant ones as they are associated with the stiffness of the main interior frames showed excellent correlation, within 3% of the measured response.

Again, the mode shapes can be compared by plotting the crossMac values, presented in

Figure 4.20. The results were excellent, with lowest crossMAC value in the diagonal being 0.86. In summary, the bare frame model seemed to be adequate without the need for any calibration, especially considering that the actual distribution of the roof mass was not known.

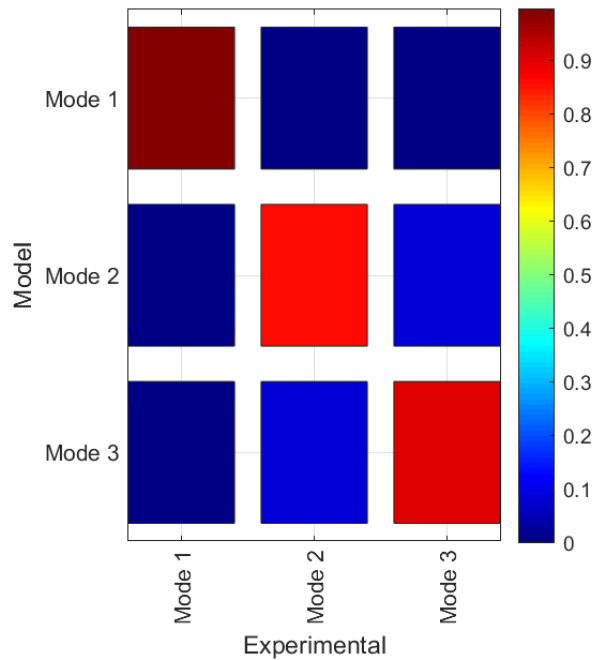


Figure 4.20: crossMAC for building NC-2 – test 1

4.2.2 Test with Walls installed

Experimental results

The second test was performed once the installation of the metal panels in every wall was completed. At the time of testing, the roof panels were still bundled on top, so the only significant difference between tests was that the endwalls now had the sheeting in place. Figure 4.21 shows the acceleration recordings during the second measurement, with the naming convention being equal to that of the first test.

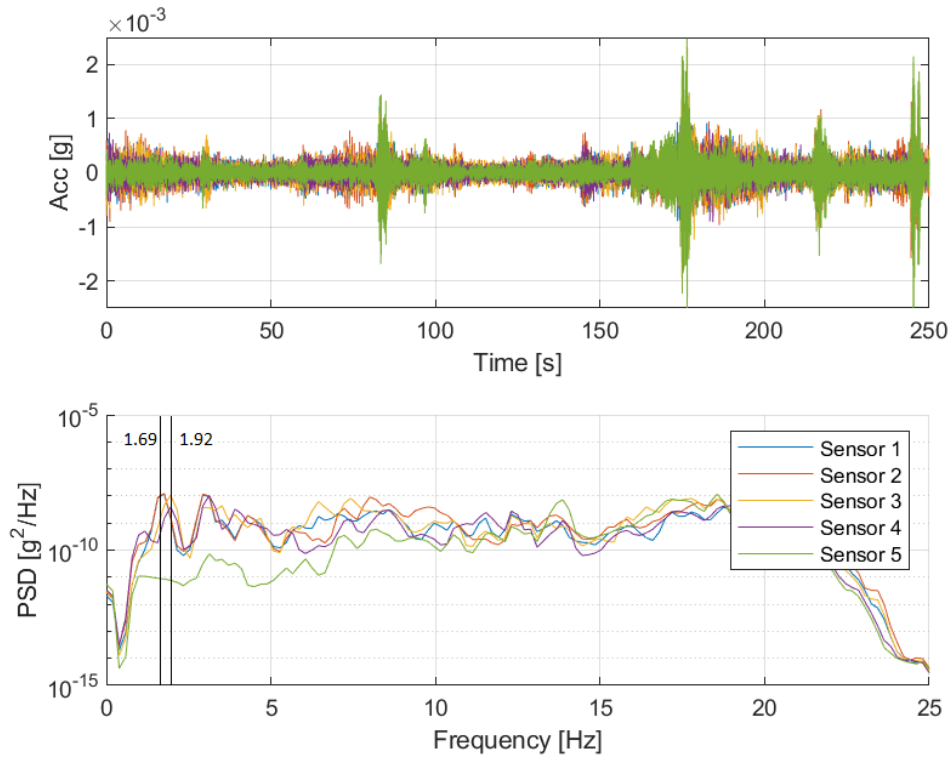


Figure 4.21: Collected data for the second measurement of the second test in Building NC-2

Note that – when compared to the results of the first test in Figure 4.16 – the response from the inner frames (sensors 1 to 4) has not changed. However, the right endwall (sensor 5) exhibits much smaller acceleration amplitudes, and the peak at $2Hz$ ($0.5s$) not present anymore. This is evidence of the stiffening effect of the endwall cladding, though it does not seem to affect the main frames or the overall response of the structure, at least while the roof isn't in place.

Since the endwall mode is no longer present (for the frequency range studied at least), the two modes identified by the SSI algorithm are presented in Figure 4.22. Note that these are virtually unchanged from modes 2 and 3 of test 1.

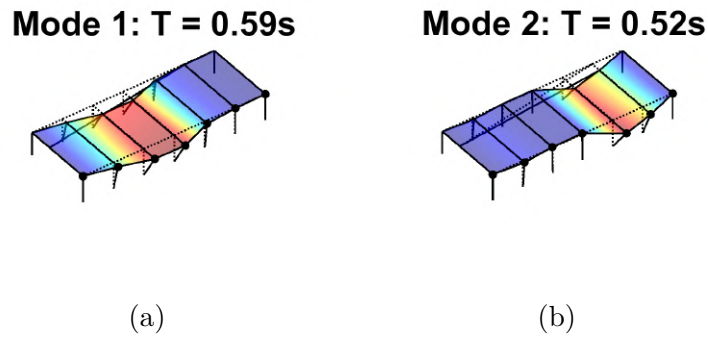


Figure 4.22: Experimental modes from test 2 in Building NC-2

3D Model Prediction

The previous model was updated to reflect the new testing conditions, mainly incorporating the rest of the cladding with the same properties as before. Given its similarity to the previous model, the model won't be shown. The first two modes in the transverse direction can be seen in Figure 4.23.

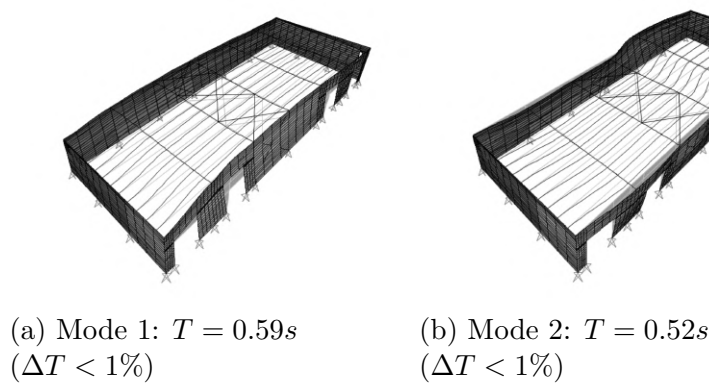


Figure 4.23: Mode prediction from SAP2000 for test 2 in Building NC-2

The periods for both modes matched almost exactly with the experimental results. The mode shapes however weren't as accurate, though still satisfactory, with the lowest value being 0.72. The crossMAC plot is presented in Figure 4.24

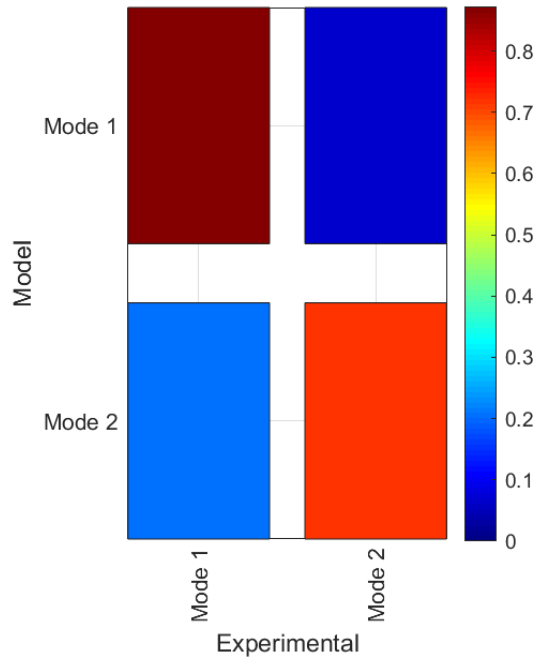


Figure 4.24: crossMAC for building NC-2 – test 2

4.2.3 Test on completed building

Experimental results

The third and final test on building NC-2 was carried out after the roof panels were installed. Given that the panels were already sitting on top of the purlins before, this test can help to directly compare the behavior of the building before and after the roof is in place, and evaluate whether diaphragm action is observed or not. The acceleration records are shown again for the second measurement, which included mainly the frames on the right side of the building (Figure 4.25).

The most significant difference is that now a single peak was present in the $1.5Hz$ ($0.67s$) to $2Hz$ ($1s$) range. Similar to building VA-1, despite experiencing similar levels of vibration, the installation of the roof seems to make the identification of higher order modes more difficult.

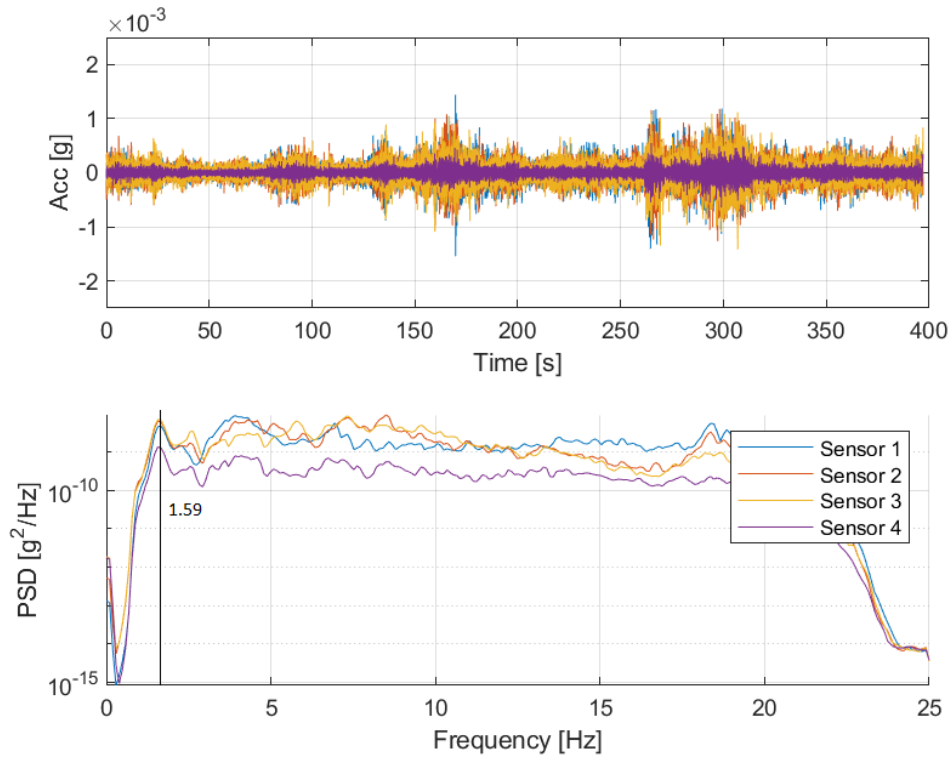


Figure 4.25: Collected data for the second measurement of the third test in Building NC-2

One possible explanation for this, as Rogers and Tremblay ([Rogers and Tremblay, 2010](#)) showed, is that the stiffness of decks can be very sensitive to amplitude. Higher order modes tend to create greater distortions at the roof level due to the relative movement between frames, and so they would be more sensitive to any added friction stiffness only present at low level vibrations compared to the fundamental mode. However, it is not possible to draw any definite conclusions from the test results, as no measurements exhibited larger amplitudes to test this hypothesis.

In the end, only the fundamental mode was able to be identified from the data, presented in Figure 4.26a. Note that no displacement is shown for frame line 3, as the sensor malfunctioned.

3D model prediction

The last update to the 3D model was removing the linear mass in each frame line and include the roofing as shell elements. Working under the assumption that it provided no stiffness and all diaphragm stiffness is explained by the purlins, its in-plane stiffness were reduced by 10^5 . The first mode taken from the model can be seen in Figure 4.26b, again showing a very good correlation in terms of period ($\Delta T < 5\%$) and crossMAC (0.80).

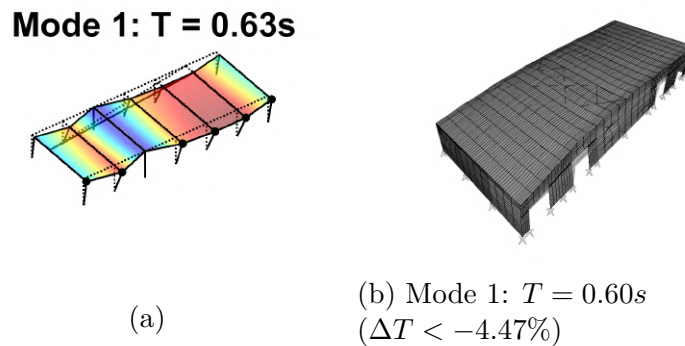


Figure 4.26: First mode from test 3 in Building NC-2. Left: experimental. Right: predicted

4.3 Building NC-1

4.3.1 Test on Bare Frame

Experimental Test

The first two buildings shown up until this point were characterized by their regular geometry and open floor space, with no partitions. Building NC-1 is an interesting case study due to the presence of appendices in several frame lines, as well as including (in its final configurations) either plaster or cladding walls that extended onto the roof and across the whole span of certain frames.

The first test on building NC-1 took place after the erection of the main and secondary framing, including the appendices. Some cladding, mainly on the near the base of the columns, had already been installed on the perimeter. The sensor locations for both measurements comprising test 1 can be seen in Figure 4.27.

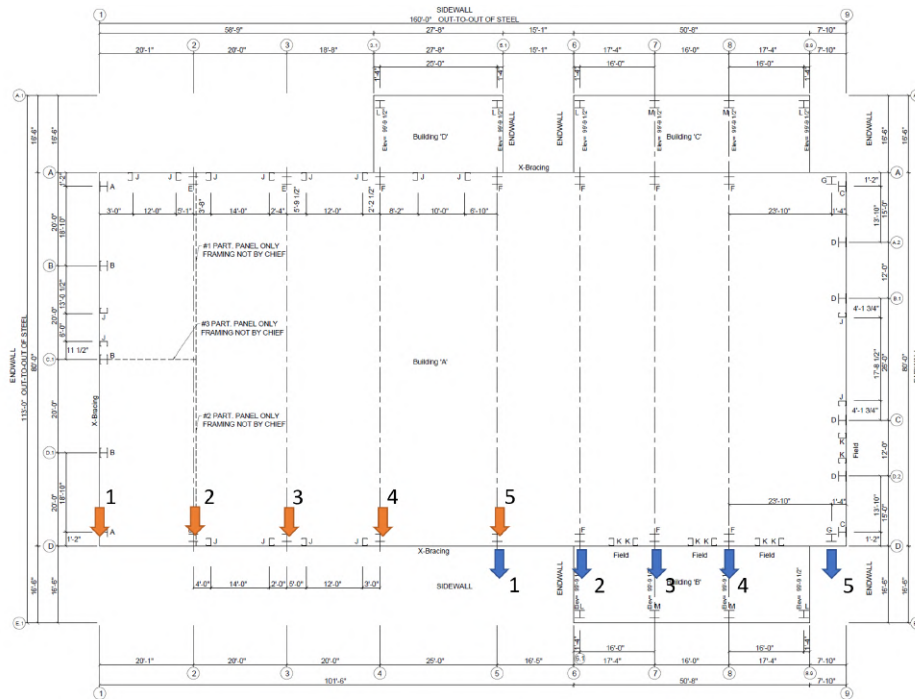
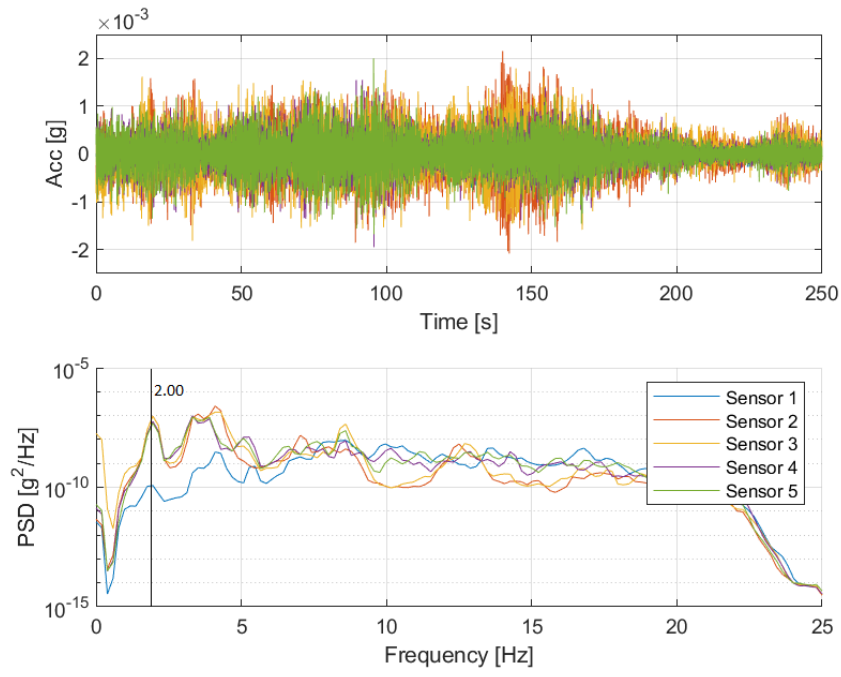
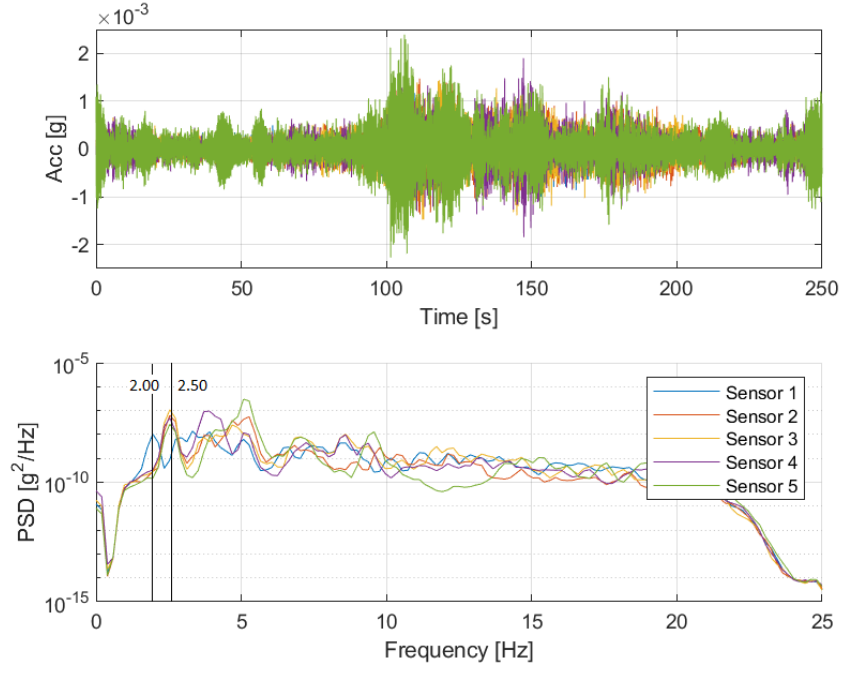


Figure 4.27: Sensor locations for Test 1 in Building NC-1. In orange: measurement 1. In blue, measurement 2.

The recorded data for both measurement 1 and 2 are shown in Figure 4.28. Looking closely at the frequency domain data, it can be seen that the sensors in measurement 1 all tend to peak at around $2Hz$ ($0.5s$). Meanwhile, the sensors in measurement two peak at a higher frequency of $2.5Hz$ ($0.4s$). The exception to this is Sensor 1 (the reference sensor). It looks as though the structure is essentially behaving as two different buildings. The left side of the building, with fewer appendices being more flexible than the right side of the building with appendices on both sides. The fact that such disjointed behavior can be observed is indicative of the low stiffness provided by the purlins interconnecting each frame line.



(a) First measurement.



(b) Second measurement.

Figure 4.28: Collected data for both measurements of the first test in Building NC-1

This analysis can be confirmed by looking the modes obtained from running the SSI algorithm, which are shown in Figure 4.29. Three modes were identified in total, the first being similar in shape to the first two modes of a simply supported beam spanning from frame 1 up to frame 6 (where appendices on both sides appear), and the third mode similar to a simply supported beam in the right side of the building.

Compared to previous tests, the endwalls in this case seemed to already be stiffer than the interior frames even without the cladding installed. This is most probably due to the fact that in the previous buildings the endwalls consisted of simply portal frames, while in building NC-1 the left endwall was braced on its middle bay and the right endwall actually consisted of a web tapered frame in similar fashion to the interior frames plus the framing required to install the veneer facade in the future.

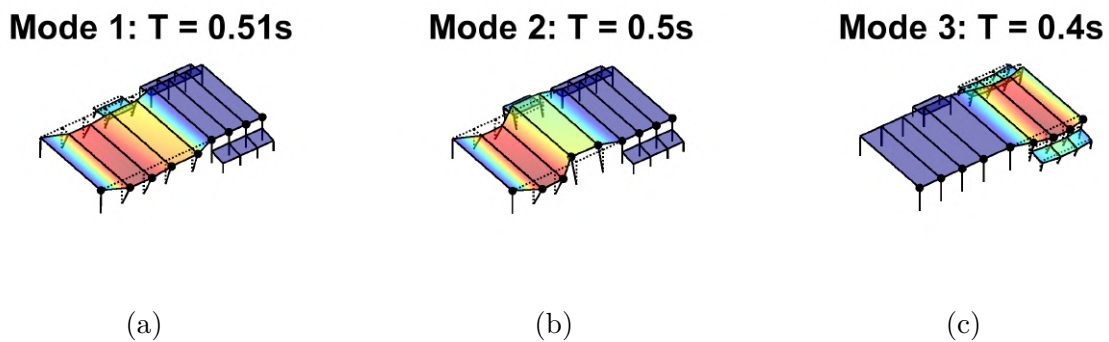


Figure 4.29: Experimental modes from test 1 in Building NC-1

3D Model prediction

Figure 4.30 shows the first three mode shapes in the transverse direction obtained in SAP2000. The model was created using the same assumptions and following the same steps as in previous cases. Similarly to building NC-2, since the roof mass from the panels was already in place – bundled on top of the purlins – at the time of testing, these were explicitly included as a linear mass.

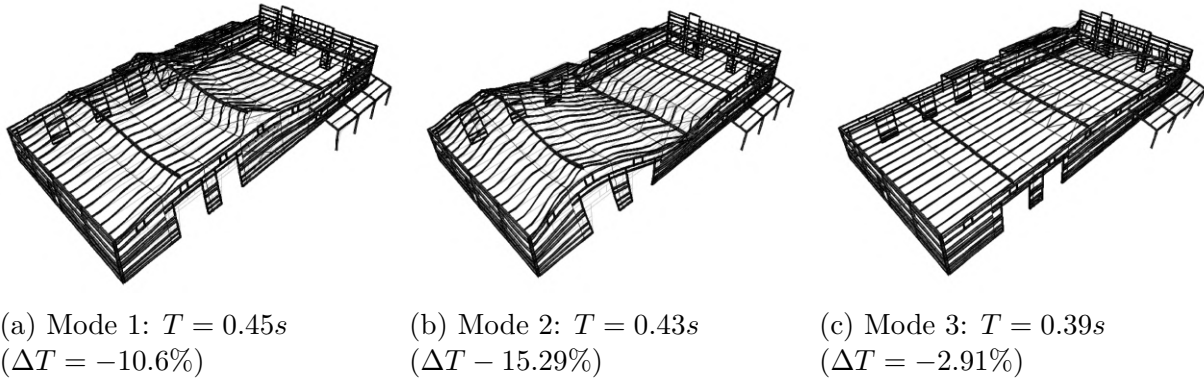


Figure 4.30: Mode prediction from SAP2000 for test 1 in Building NC-1

Comparing the periods with the results from the experimental data, it can be seen that the model tends to overestimate the stiffness of the inner frames. Since the modes are exhibiting global behavior, this could also be related to an overestimation of the purlin stiffness, as the connection was modeled as rigid. The effect of purlin stiffness will be discussed in later sections.

Finally, Figure 4.31 shows the crossMAC evaluation, which shows the the model mode shapes are remarkably similar the ones obtained via ambient vibrations. the lowest value being 0.90 for the first mode.

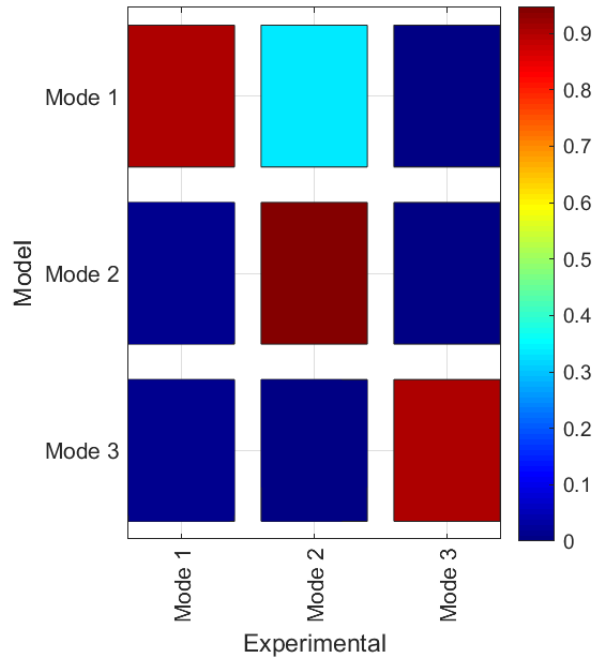


Figure 4.31: crossMAC for building NC-1 – test 1

4.3.2 Test on fully clad building

Experimental results

The second test on building NC-1 took place once the cladding was installed and interior partitions had been built. These partitions (shown back in Figure 3.15) were located in frame lines 2, 6 and 7 of the building, starting from the left. For reference, these correspond to sensor 2 of measurement 1, and sensors 2 and 3 of measurement 2 (See Figure 4.27).

Measured data was only available for frame lines 1, 2 5 and 9 of the building. Since frame lines 1 and 9 correspond to the endwalls, and frame line 2 had a metal panel wall attached to the frame, these sensors did not pick up any significant acceleration records. However, this shows that the interior partitions in this case were introducing significant stiffness to the frame the were attached to. The acceleration record from sensor 5 along with its associated

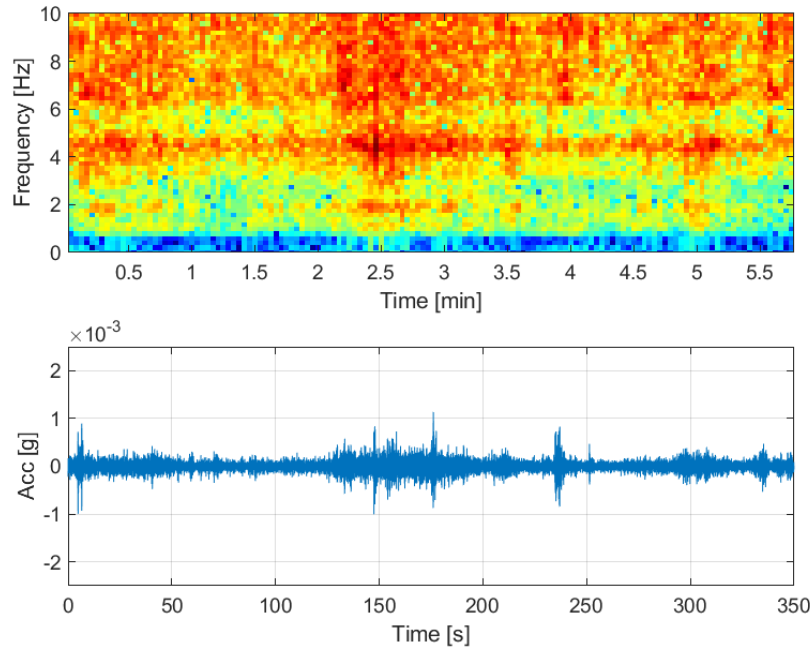


Figure 4.32: Acceleration record for sensor 5 during measurement 1, test 2 for building NC-1

spectrogram is shown in Figure 4.32.

Comparing the amplitudes to those seen in Figure 4.28, it's clear to see that during the second tests the amplitudes were smaller, by at least a factor of 2. This translated into the structure's lower frequency not being excited consistently during the test. The spectrogram shows that only when there was an increase in amplitude up to around $0.0005g$ the first mode of the structure was participating in the response, as noted by the red line around $2Hz$ ($0.5s$) from the 90s up to approximately the 120s mark. Again, obtaining full modal information of the fully clad buildings using ambient vibrations is a challenge.

The SSI algorithm was capable of identifying the fundamental mode of the structure, which only had significant displacements where sensor 5 was located. Due the lack of spatial information the mode shape is not shown, but the fundamental period of the fully clad building was $2.0Hz$ ($T = 0.5s$). This is a small, largely insignificant change in the period,

though it's not possible to take further conclusions from this without having mode shape information.

3D Model prediction

The full model for building NC-1 including the cladding and partitions can be seen in Figure 4.33. Up until this point it has been show that the stiffness cannot be calibrated with the available data. The reason is mainly that endwall cladding and partitions effectively act as infinitely rigid elements relative the main frames. With this in mind, it was decided to include the partitions in the model as restraints in the transverse direction. This simple approach was only taken for the purpose of finding the mode shape information in the frequency range of interest, and should not be taken as a definitive statement on the amount of stiffness introduced by the partitions (e.g.: for deflection calculations or load transfer).

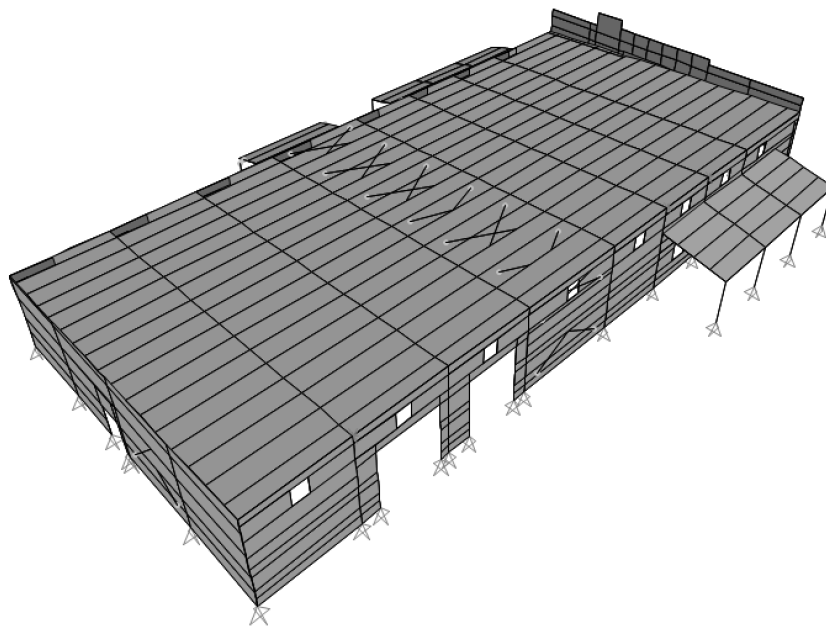
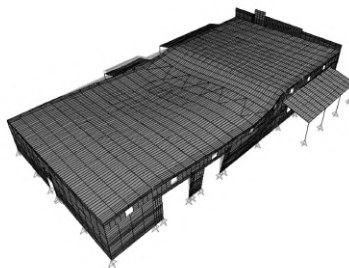


Figure 4.33: SAP2000 model of building NC-1 for test 2

The first mode obtained in SAP200 is shown in Figure 4.34. Note that the added restrictions due to the partitions does not affect the natural period of the structure, which stayed at $0.45s$ in the model. This is consistent with the experimental results, that showed no change in the period from the test 1 to test 2. However, the mode shape was affected, as now frame 2 exhibits no movement. This is a manifestation of the low stiffness provided by the roof system and negligible effect of the standing seam roof. The frames that were not restrained by partitions (in this case, frame lines 3 to 5) are still able to deform almost freely, explaining why the period does not change from one case to the other.

Note that three consecutive frames are partition free in this case. The structure could be imagined as three interior frames with stiff walls at the ends. This is essentially the configuration for building VA-1, which also showed no interference of the endwall cladding in the response of the inner frames.



(a) Mode 1: $T = 0.45s$
($\Delta T = -10.0\%$)

Figure 4.34: Mode prediction from SAP2000 for test 2 in Building NC-1

4.4 Building VA-2

4.4.1 Test with roof installed

Experimental results

Building VA-2 was the other building in this set (along with building NC-1) that had appendices attached to its frames, though in this case they were present in every interior frame. The first test was performed after most of the framing had been erected, and the roof and back sidewall panels installed. At the time of testing the endwalls had not been fully built yet, with several missing girts and door jambs missing. Also, since the endwalls are the only frame lines without appendices, it was expected for them be more flexible than the inner frames before the cladding was installed.

The building then provides a good opportunity to see if endwall-only modes are present or if the roof cladding introduced some diaphragm action, and how the inclusion of cladding affects the dynamic properties of the completed building.

The sensor locations can be seen in Figure 4.35. Note there was no reference sensor across measurements to generate mode shape data. The recorded acceleration data can be seen on Figure 4.36. At the time of testing, there was active construction in the clerestory section, which is reflected in the larger vibration amplitudes seen during the test,

Again, it wasn't possible to reliability identify mode shapes, but the structural modes were obtained from the SSI algorithm, with frequencies of $1.97Hz$ ($0.50s$), $2.67Hz$ ($0.37s$) and $3.51Hz$ ($0.28s$).

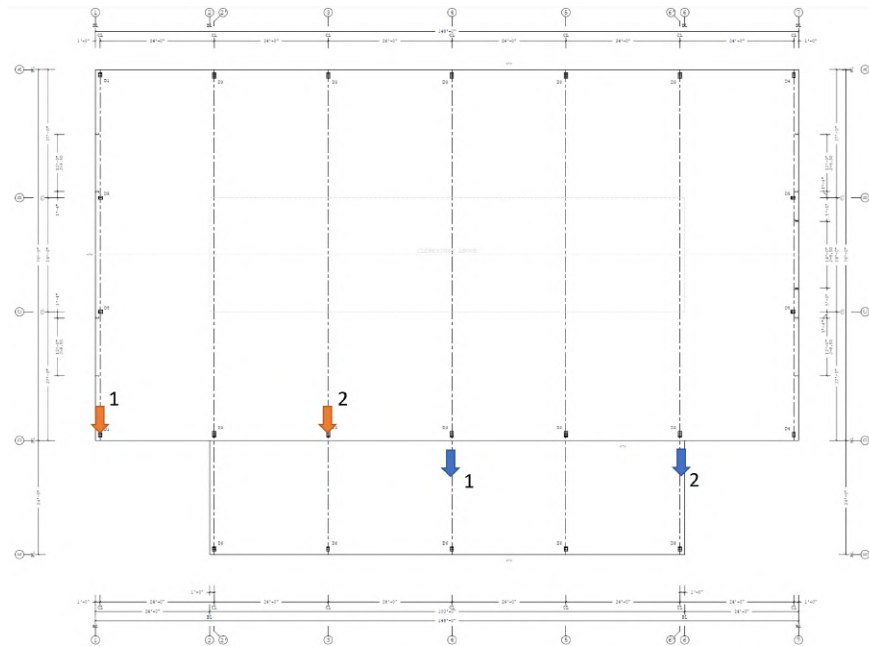


Figure 4.35: Sensor locations for Test 1 in Building VA-2. In orange: measurement 1. In blue: measurement 2.

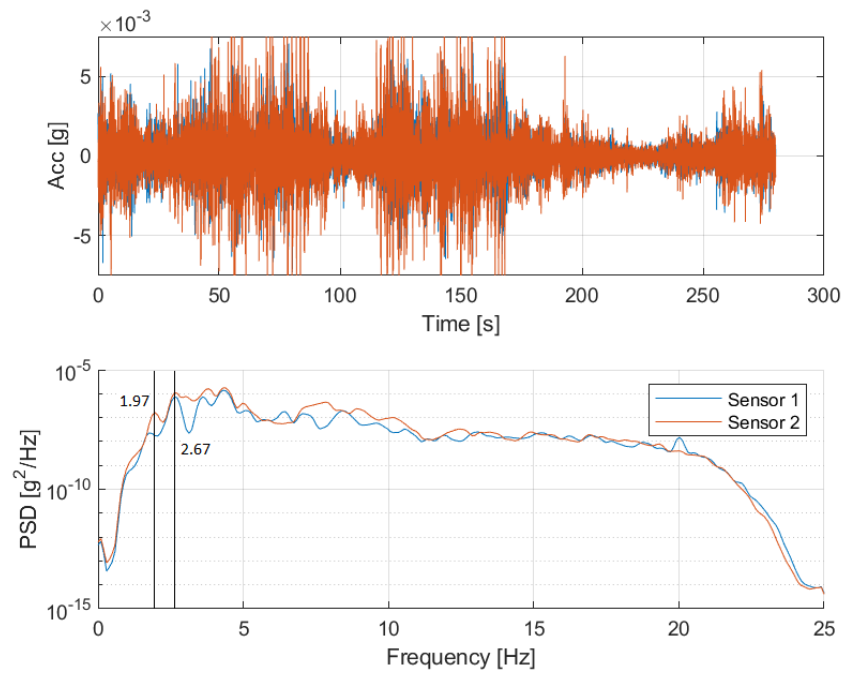


Figure 4.36: Collected data for the second measurement of the first test in Building VA-2

3D Model prediction

The 3D model for test 1 was built to resemble testing conditions as best as possible, removing the missing girts and introducing the temporary bracing on the right end wall. Again, it was assumed the roof panels were providing no diaphragm action by reducing its stiffness in SAP, with all the stiffness being provided by the purlins. An overview of the model can be seen in Figure 4.37

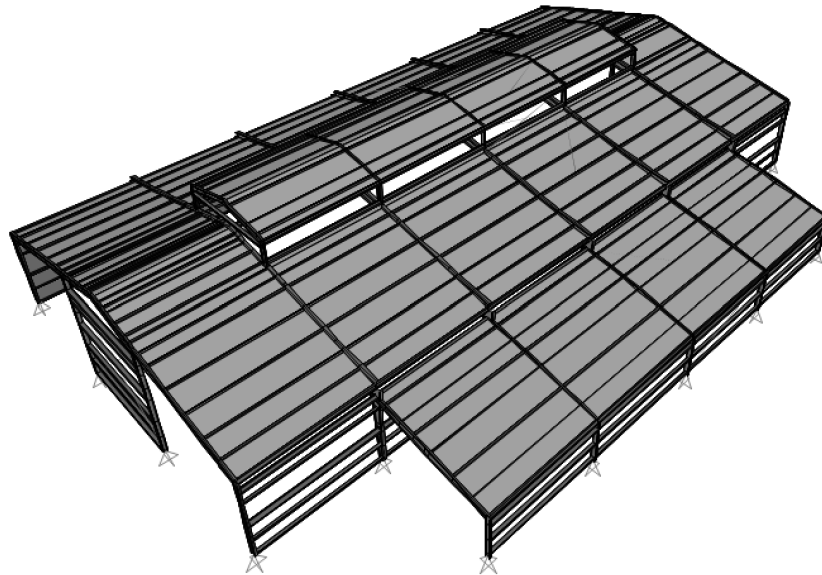


Figure 4.37: SAP2000 model of building VA-2 for test 1

The first three modes obtained from the model are shown in Figure 4.38. Given the limitations of the experimental data, it was decided to not do a direct comparison between modes. However, the periods tend to agree well with the measured results, and so the model was considered to be acceptable for future model updating. It should be noted that Mode 3 ($T = 0.32s$) is the mode associated with the movement of the interior frames.

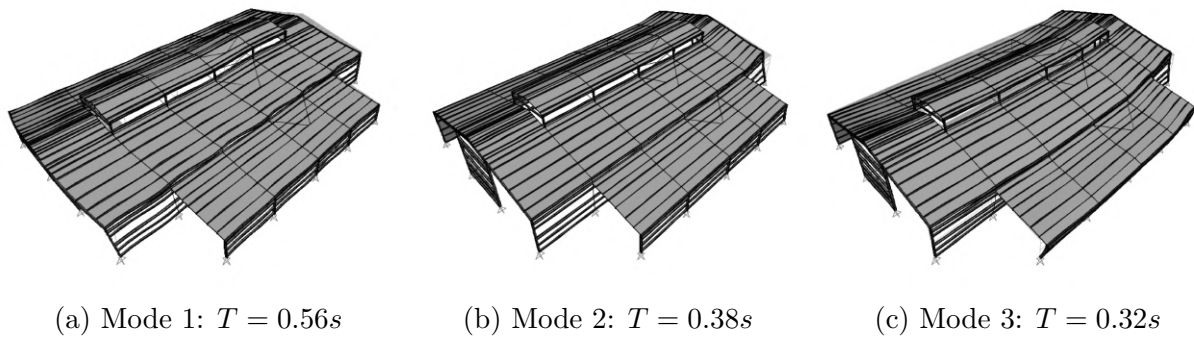


Figure 4.38: Mode prediction from SAP2000 for test 1 in Building VA-2

4.4.2 Test on fully clad building

Experimental results

The second test was carried after all the cladding had been installed on the main building, not so in the office section (the floor space generated by the appendices). This time around a denser instrumentation was available. The sensor locations for each measurement are shown in Figure 4.39

Figure 4.40 shows the recorded accelerations during measurement 2, both in the time and frequency domains. Two main differences can be seen with respect to previous test. First, measured amplitudes are significantly smaller than during test 1. This is mainly a consequence of the test conditions, as the only significant source of vibrations for this test was wind, given the remote location of the building and the lack of active construction work at the time.

The second main difference is in the frequency content, as there are no longer any peaks in the $1Hz$ ($1s$) to $3Hz$ ($0.33s$) range which, according to the previous model, were related to the endwalls. Instead a peak at around $3Hz$ ($0.33s$) is visible.

From the experimental data two modes were identified based on the SSI method. The first

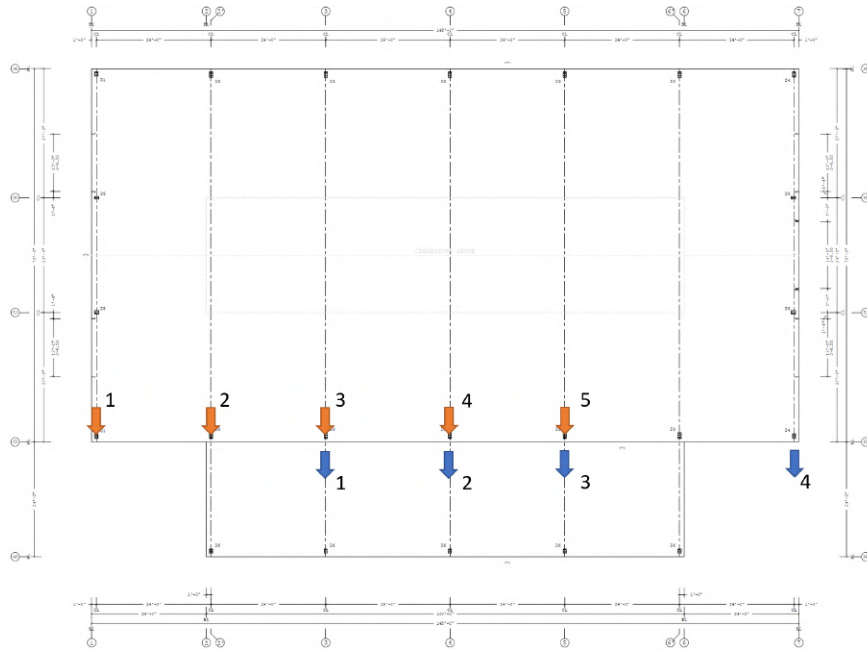


Figure 4.39: Sensor locations for Test 2 in Building VA-2. In orange: measurement 1. In blue: measurement 2.

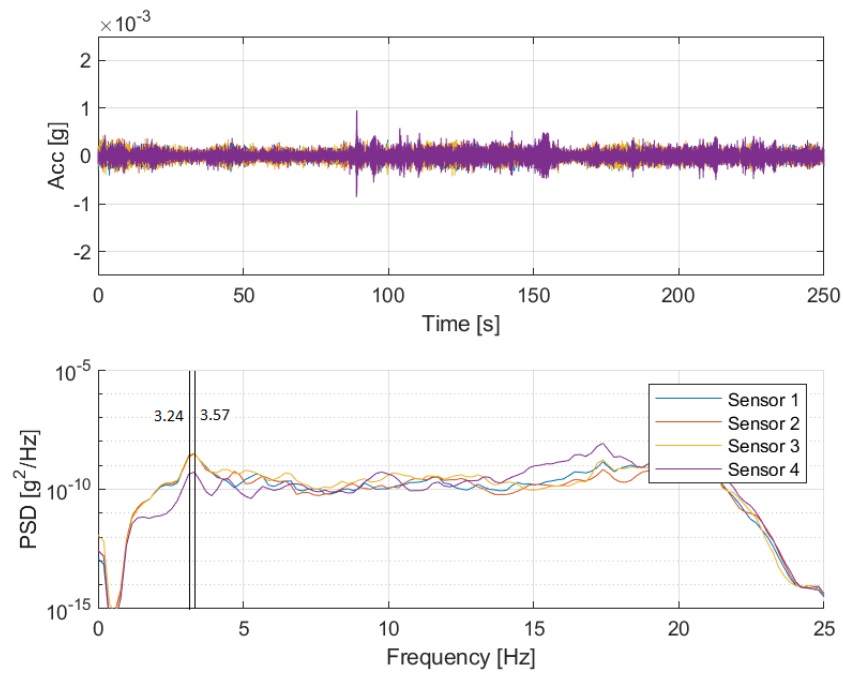


Figure 4.40: Collected data for the second measurement of the first test in Building VA-2

mode had a natural frequency of $3.24Hz$ ($0.31s$) and the second mode was found at $3.57Hz$ ($0.28s$). Note that the first mode here identified is very close to the third mode found in test 1 ($0.28s$) which was later found to be associated with the displacement of the interior frames.

The mode shapes for the identified modes are shown in Figure 4.41, where it can be seen that they are both related to the movement of the interior frames.

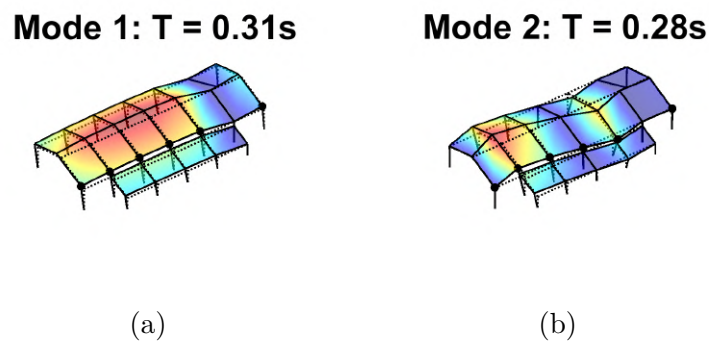
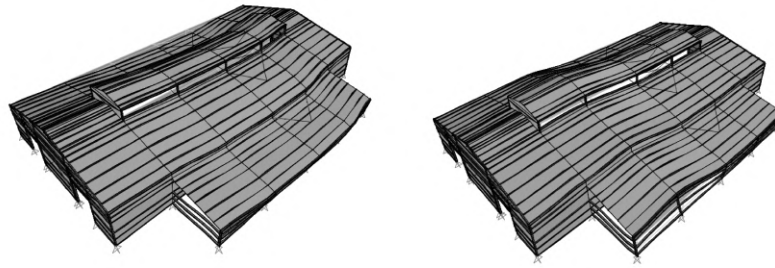


Figure 4.41: Experimental modes from test 2 in Building VA-2

3D Model prediction

Figure 4.42 shows the first two transverse modes of the structures obtained from the updated 3D model for Building VA-2, which now includes the metal panels on walls of the main open floor space. The model still assumes the roof cladding is not providing any additional stiffness, using the same modifier as in previous models. Note that the first mode is essentially identical to the third mode shown for the Test 1 prediction. This is expected, as the walls do not provide a significant amount of mass to the building, while the roof weight was already in place. This is a direct result of the negligible added stiffness provided by the roof.

More importantly though, the periods from the model match very closely with the results from the experimental tests, with differences smaller than 5%. In turn, once again it follows



(a) Mode 1: $T = 0.32s$
 $(\Delta T = 4.24\%)$ (b) Mode 2: $T = 0.29s$
 $(\Delta T = 4.41\%)$

Figure 4.42: Mode prediction from SAP2000 for test 2 in Building VA-2

that assuming the roof of a metal building introduces no diaphragm action provides good estimates of the building behavior. Similarly, the first mode of the test 1 model, which was dominated by the endwall, is no longer present after the cladding is install.

Figure 4.43 shows the crossMAC between mode shapes obtained from both the model and from test 2. The values for this case were lower, though still above 0.7 in the diagonal and below 0.1 otherwise, implying a good correlation between the mode shapes.

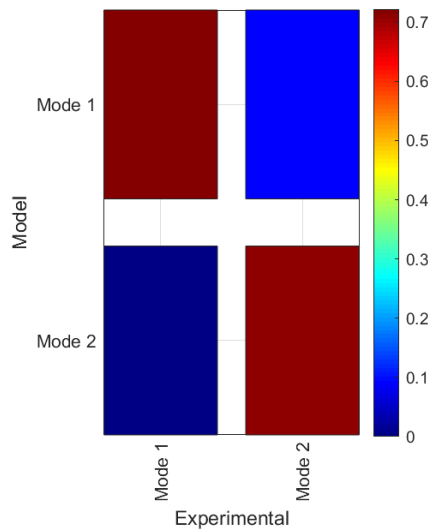


Figure 4.43: crossMAC for building VA-2 – test 2

4.5 Building WV-2

Test on fully clad building

Experimental results

From this point on, the buildings left to discuss were tested only after essentially all the cladding was installed. In the particular case of building WV-2, the right endwall was not fully built in order allow equipment to come in and out of the building. However, some cladding was partially present. The sensor locations during the test are shown in Figure 4.44.

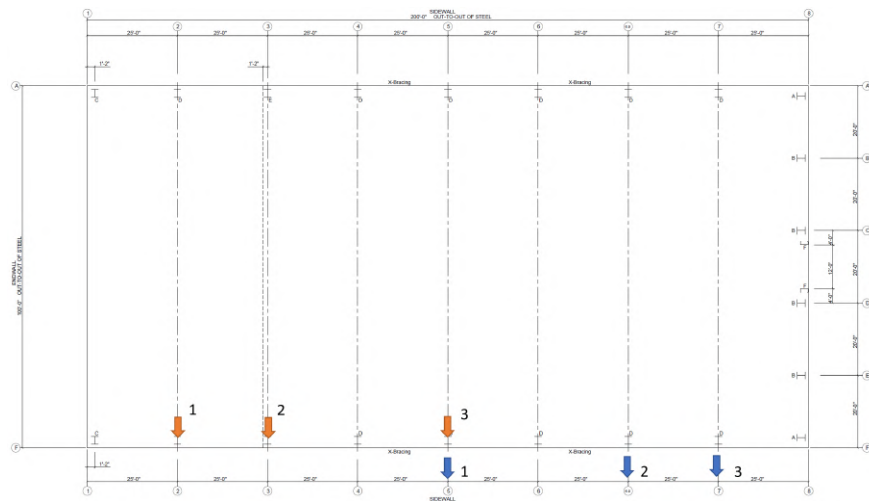


Figure 4.44: Sensor locations for the test in Building WV-2. In orange: measurement 1. In blue: measurement 2.

Figure 4.45 shows the acceleration data from measurement 1. Note that sensor 3, on the “interior” of the building peaks at a frequency around $2Hz$ ($0.5s$) while sensor 1 (one of the exterior frames) and sensor 2 (on the cladded wall) do not have any energy in that frequency range.

The results from running the SSI algorithm can be seen in Figure 4.46. The fundamental frequency of the building was found to be $1.39Hz$ ($0.72s$), with the mode shape showing

typical global behavior in between the cladded endwalls. Note frame 2 does not participate in this mode.

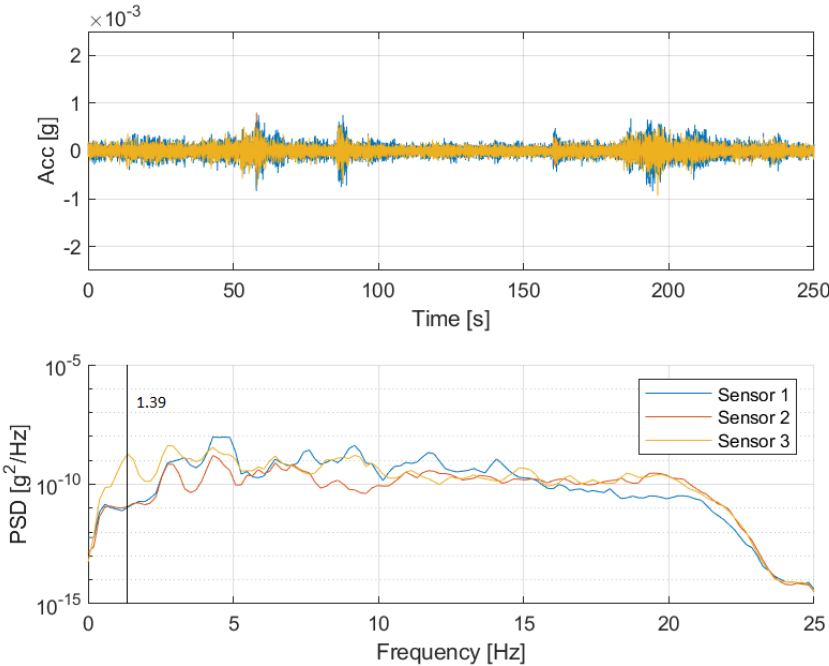
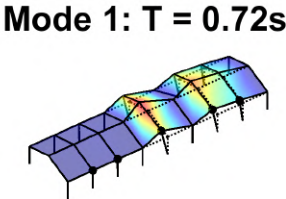


Figure 4.45: Collected data for the first measurement during the test in Building WV-2



(a)

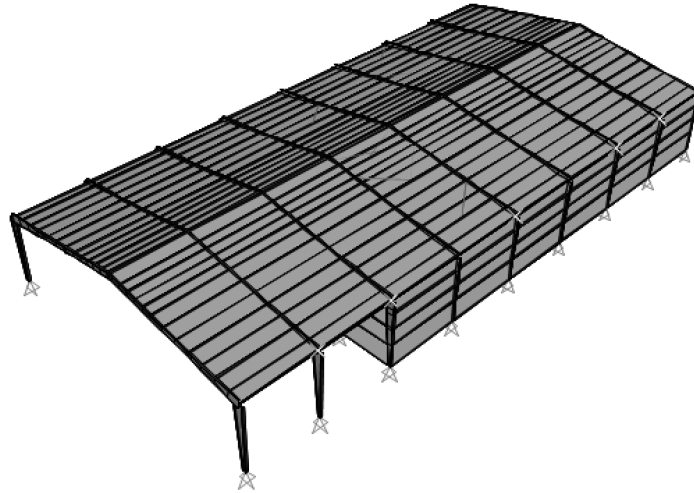
Figure 4.46: Experimental modes from the test in Building WV-2

3D Model prediction

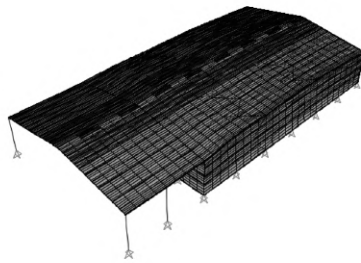
Figure 4.47 shows the full 3D model of building WV-2, built based on the state of the building at the time of testing, along with the the first two modes in the transverse direction. Even though mode 1 was identified during testing, mode 2 is shown in order to shed light on the behavior of the building. The frames on frame lines 1 and 2 were marginally more flexible than the ones on the rest of the building. Were the frames to be behave perfectly independently from each other, it would be expected for the first modes of the structure to be associated with the movement of these two frames.

However, from the resulting mode shapes it's clear that that isn't the case. Even if the roof isn't providing diaphragm action, the limited stiffness coming from the purlins is enough to create global behavior in conjunction with the endwalls, the first mode dominated by the concurrent movement of the frames on the interior of the building, and the second mode described by the displacement of the exterior frames.

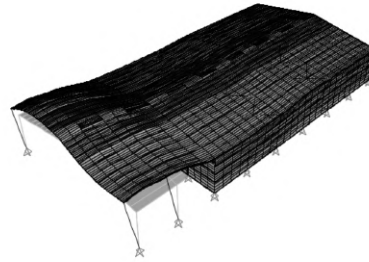
In any case, the model underpredicted the period by about 9%, while the mode shape matched very well with the experimental one (crossMAC = 0.95).



(a) Overview of the 3D model for building WV-2



(b) Mode 1: $T = 0.65s$ ($\Delta T = 8.9\%$)



(c) Mode 2: $T = 0.57s$

Figure 4.47: Analytical model of building WV-2

4.6 Building WV-1

Test on fully clad building

Experimental results

The test on building WV-1 was carried out with the building fully operational. Two measurements were taken covering the 6 interior frames of the building, as experience had shown

at this point that endwalls do not participate in the first mode of these buildings. Figure 4.48 shows the experimental modes resulting from applying the SSI method.

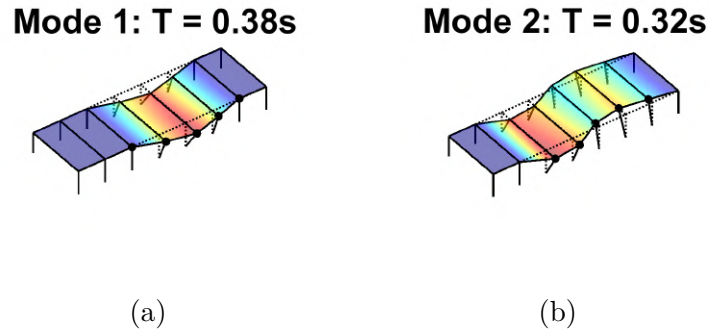


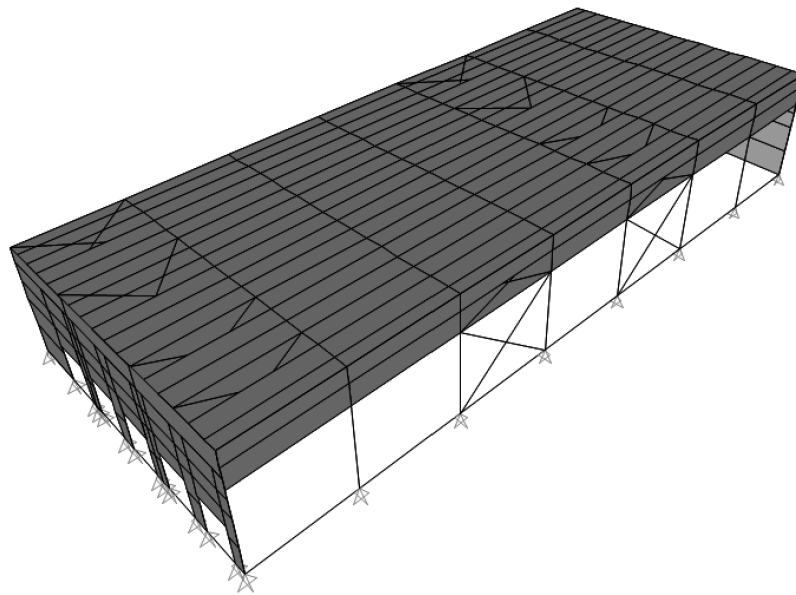
Figure 4.48: Experimental modes from the test in Building WV-1

3D Model prediction

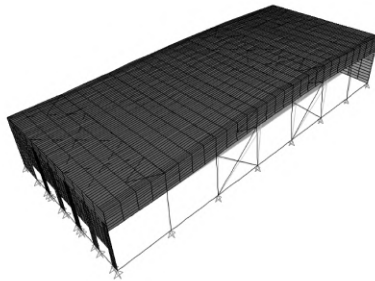
Figure 4.49 shows the model used to predict the modal properties of building WV-1, following the structural drawings available. Also in the Figure the first two modes in the transverse direction are presented.

It's clear that the periods predicted by the model are not consistent with the results obtained empirically. The overestimation was almost by a factor of 2 (100%), which was concerning. A few possible explanations were singled out for this. First, it would be possible that the roof of this building was providing significant diaphragm action and making the walls participate in the mode. However, based on all previous tests that showed the roofs providing no stiffness, and the mode shapes in Figure 4.48 where the displacements approach 0 as the frames get closer to the endwalls, this option was discarded.

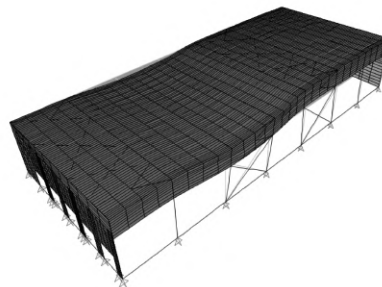
The second possible explanation would be a strong influence of the adjacent building, even if they weren't connected, which is plausible. The gap between the adjacent structures can be seen in Figure 3.13b, showing that the two structures were designed to act largely



(a) Overview of the 3D model for building WV-1



(b) Mode 1: $T = 0.73s$
($\Delta T = 93\%$)



(c) Mode 2: $T = 0.65s$
($\Delta T = 99\%$)

Figure 4.49: Analytical model of building WV-1

independent. Based on the erection drawings, the only connection between the structures is a base angle anchored to the concrete of the existing building which serves as the support of the sidewall panels along that wall line, in order to provide sealing. Given the flexibility of the metal cladding in bending this should not be cause the structures to work as a unit, though it cannot be fully discarded especially under low-level excitation.

Finally, it could be that the stiffness of the frames had been misrepresented in the model. In order to see if that was the case, the first step was looking at whether the mode shapes

obtained by the model correlated well with those obtained experimentally. If that were the case, then it could be argued that the difference in period would be mostly explained by a difference in stiffness of the frames alone. Other changes (like the restraints provided by the adjacent building, or cladding stiffness) would result in a change in mode shapes.

Figure 4.50 shows the crossMAC plot between the experimental test and the original model. Given the high MAC values (0.79 and 0.97), it was concluded that a miscalculation of the frame stiffness was the most probable cause of the discrepancy. Note that a change in period of a factor of 2 implies that the stiffness was off by a factor of 4, since the period scales with the square root of the stiffness.

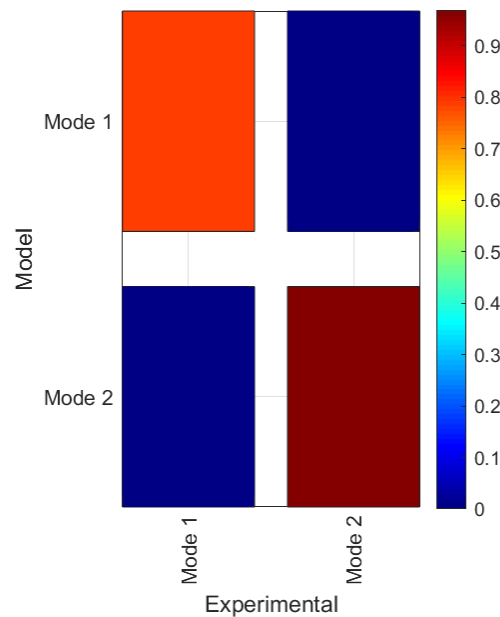


Figure 4.50: crossMAC for building WV-1

One possible explanation for this, as shown both previous studies ([Bajwa et al., 2010](#); [Kumar et al., 2020](#)) is the rotational stiffness of the column base, which can have a significant impact on the overall stiffness of the frames. However, a fully fixed based is not to be expected either.

In order to see the influence of the the column base stiffness, the model was updated assuming

a fixed column base, from which a fundamental period of 0.39s was obtained, which is about a 5% difference compared to the experimental result. Thus, there is large difference in frame stiffness depending on base fixity. It is possible that building WV-1 is more sensitive to this because of its straight columns, meaning that the moment of inertia is constant along their length instead of being an order of magnitude smaller at the base, as well as causing the bolts anchoring the column to be further apart, increasing the connection stiffness. The details of the connection, however, were not significantly different to those tested by Smith (Smith, 2013), both having a 0.375in thick baseplate with 0.75in anchor rods.

4.7 Building NC-3

Test on fully clad building

Experimental results

The final test in the study, building NC-3, was tested after all the cladding was installed. All five frames were measured, and the acceleration records can be seen in Figure 4.51. The fundamental frequency as per the SSI method, was 6.3Hz (0.15s), with the mode shown in Figure 4.52.

3D Model prediction

From the analytical model created on SAP2000, the first mode of the building in the transverse direction was found to be 3.75Hz (0.25s). The prediction given by the model was off by 73% in period, despite a high crossMAC value of 0.88. Similar to building WV-1, it is believed that the most possible explanation is an underestimation of the frame stiffness due

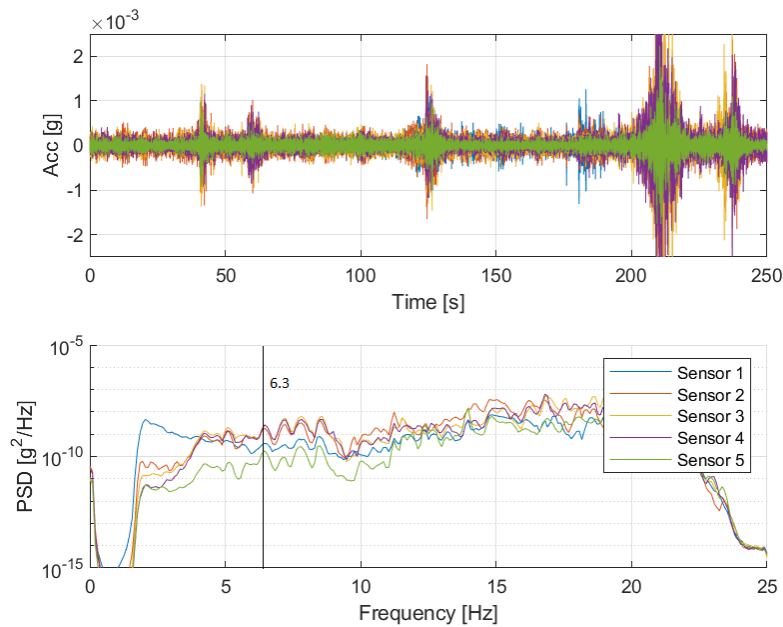


Figure 4.51: Collected data during the test in Building NC-3

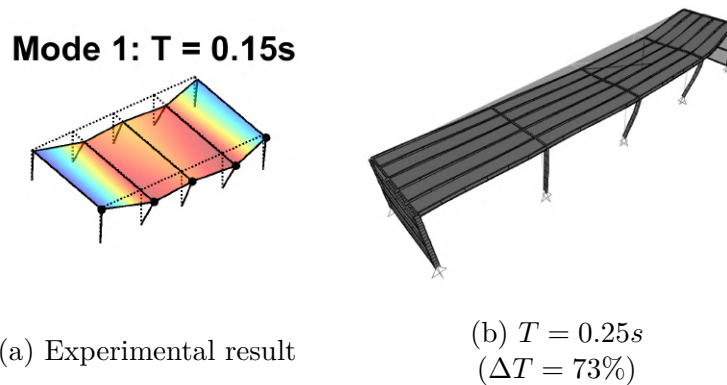


Figure 4.52: Comparison between the empirical and analytical first mode for building NC-3

to the pinned base assumption.

The model was updated to account for the possible fixity of the base, and it was found that assuming a fixed connection reduces the first period of vibration to 0.16s, which is very close the test results. Similar to building WV-2, building NC-3 – with straight columns – is very sensitive to the base fixity compared to other buildings tested with web tapered members.

4.8 Discussion

4.8.1 Summary

In total, 13 tests were carried out in 7 different buildings during different stages of construction. In three of the buildings (VA-1, NC-1, NC-2) it was possible to test the buildings when only the bare frame was present. Table 4.1 summarizes the results, showing the fundamental period (defined as the period for the mode with largest mass participation ratio in the transverse direction) obtained via ambient vibrations and through 3D modeling. From the results it follows that the assumptions made in the modeling of these structures were appropriate to obtain accurate results.

Table 4.1: Summary of fundamental period on bare frame structures

Name	T_{test} [s]	T_{model} [s]	$crossMAC$	ΔT [%]
VA-1	0.54	0.51	0.96	-6.7
NC-1	0.51	0.45	0.90	-10.6
NC-2	0.58	0.58	0.86	< 1

The other important aspect of this data set is that it allows us to compare the results during different stages of construction with the same – or almost the same – total mass applied to the structure. That was the case in buildings NC-1 and NC-2, which in all their tests had the roof mass acting on the structure, and also in building VA-2, where the difference between tests was the addition of the endwall cladding. Table 4.2 shows that in all 3 cases, the fundamental period stayed essentially the same across stages of construction.

This last result is extremely valuable, as it shows that the roof cladding in metal building systems is not engaging in diaphragm action. More than that, no significant influence of non-structural elements was observed. These two observations seem to be unique to metal buildings compared to other single-story buildings found in the literature, which experienced

Table 4.2: Comparison between tests for buildings in which applied mass stayed constant

Name	T_{test1} [s]	T_{test2} [s]	T_{test3} [s]
VA-2	0.28	0.31	-
NC-1	0.51	0.50	-
NC-2	0.58	0.59	0.63

large differences in stiffness across construction stages (Gryniewicz et al., 2021; Lamarche et al., 2009; Rogers and Tremblay, 2010; Tremblay, 2005; Wrzesien et al., 2015). Instead, it validates the 3D-modelling assumptions used by Langley (Langley, 2018) for metal buildings, who modeled the purlins but ignored the roof cladding, including their mass as a line mass to the main frame elements, similar to what was shown in this research for buildings NC-1 and NC-2.

It should be noted, however, that the previous table refers to the fundamental period as defined by the mass participation factor, which in all cases was associated with the displacement of the interior frames. The mode with largest period did not necessarily stay constant. As shown in buildings VA-1, VA-2 and NC-2, the addition of endwall cladding introduced enough stiffness for the endwall-dominant modes to not be identifiable during ambient vibration. However, the extent in which they do so (i.e., what their effective shear value G' is) cannot be recovered from the data as even low values of G' turn the endwalls essentially infinitely stiff compared to the interior frames.

Finally, Table 4.3 summarizes the results for all tests carried out on completed buildings, as well as comparing the fundamental period between the tests and the 3D model predictions. All the 3D models assumed the roof to provide no diaphragm action, and the columns to be pinned at their base. In general, very good correlation was found between the models and the tests, with most periods being within 10% and crossMAC values above 0.7.

Table 4.3: Summary of tests done on fully clad buildings

Name	T_{test} [s]	T_{model} [s]	$crossMAC$	ΔT [%]
VA-1	0.43	0.42	0.98	-1.8
VA-2	0.31	0.32	0.72	4.2
WV-1	0.38	0.73	0.79	93
WV-2	0.72	0.65	0.95	-8.9
NC-1	0.50	0.45	N/A	-10
NC-2	0.63	0.60	0.80	-4.5
NC-3	0.15	0.25	0.88	73

The two exceptions were buildings WV-2 and NC-3. Given the results for other buildings, the most probable explanation for the discrepancy of almost 2 in the natural period between the tests and the models is the degree of fixity at the base. Those models were updated to consider an idealized fixed base condition, and the resulting periods estimates were within 5% of the test results, while keeping the same crossMAC values. The reason as to why these buildings exhibit significant rotational stiffness at the base is not clear. Both buildings had prismatic columns, which means they were more sensitive to a change in base fixity as the moment of inertia was constant along the height. Figure 4.53 shows the column bases for two different buildings, VA-1 and WV-1.



Figure 4.53: Close up view of the column bases for two different metal buildings

Comparing the details from VA-1, which behaved as pinned, and WV-1, which is presumably working as fixed, two small differences can be made out (note that both bases are anchored to a concrete grade slab) . The first is the number of bolts, two on each side in VA-1 and three in WV-1. More importantly, the centroid of the column and the bolts seems to be significantly off-center in building WV-1. This was the case for every column in the building. The resulting increase in eccentricity could explain the larger rotational stiffness of the detail. However, no real conclusions can be made as it is also not known if this stiffness would remain in place for larger amplitudes of vibration. Work by Moen et al. (Moen et al., 2019), who calibrated nonlinear models for the rotational stiffness based on the shake table tests carried out by Smith (Smith, 2013) showed that said stiffness can vary by 60% depending on the type of bolts used for anchoring the base plate given the same geometry.

Perhaps more importantly, With the exception of building WV-1, all buildings tested had essentially the same detail at the column base, with a $0.375in$ and 4 $0.75in$ anchor rods. This detail was also used by Smith in his full scale shake table tests, which showed no rotational stiffness for rotations below 0.02, due to the deformation of the base plate creating a dishing effect (Smith, 2013). He also noted that, for larger rotations, highly nonlinear behavior was present as the connection becomes significantly stiffer due to the flanges impeding the rotation. It is possible then, that tightening of the bolts can restrain the base plate deformation, causing the increase in rotational stiffness though this can't be proven with the available information.

4.8.2 2D Model analysis of metal buildings

One of the main takeaways from the test results is that the roof in metal building system indeed does not contribute any significant stiffness to the structure, with most of the stiffness

of the roof system being explained by the purlins acting in their minor axis.

This was the basis for Smith and Uang to use 2D-modelling of the isolated frames to obtain their predictive period equation (Smith and Uang, 2013). It is of interest then to look at how the results differ between the 3D-models here presented and a 2D-model of an isolated frame. For all buildings, one of their interior frames was modeled separate from the rest of the structure, and assigned linear masses on its columns and rafters based on tributary areas to represent the cladding, girt and purling weight. The results of these analyses can be seen on Table 4.4.

Table 4.4: Summary of tests done on fully clad buildings

Name	T_{3D} [s]	T_{2D} [s]	ΔT [%]	T_{test} [s]
VA-1	0.42	0.42	< 1	0.43
VA-2	0.32	0.33	3.1	0.31
WV-1	0.73	0.75	2.7	0.38
WV-2	0.65	0.69	6.2	0.72
NC-1	0.45	0.50	10.0	0.50
NC-2	0.60	0.60	< 1	0.63
NC-3	0.25	0.28	10.7	0.15

The results show that the fundamental periods of metal buildings (given by the interior frames) can be effectively explained by the fundamental period of an isolated frame. 2D-models show larger periods, as expected given that they ignore the (albeit small) stiffening effect, though in general stay within 10% of the 3D model analysis and even then they are still very close to the experimental results.

The 3D-models tended to under predict the period, most probably as the connection of the purlins to the columns is not perfectly rigid. Though said connection could be modeled more accurately, as it stands a 2D model can predict the period of metal buildings with similar accuracy as a full 3D model.

Then, based on the test data and the comparison between models of different levels of detail, Smith and Uang's assumptions for the modeling of metal buildings in their synthetic database seem to hold true in the vast majority of cases. The one partial exception to this seems to be the idealized pin at the column base, which fails to describe the observed behavior in 2 out of 7 cases, though it's not possible to offer a taxative explanation for this discrepancy.

4.8.3 Modal mass participation factor

In previous work the applicability of the ELF method for metal buildings was put into the question due to the low mass participation factors for the first mode of vibration in their models (Langley, 2016; Smith, 2013). In Smith and Uang, the mass participation factor for the 2D frame on its own was found to be largely dependent on the aspect ratio of the frame. Low aspect ratios coincided with participation factors close to or above 0.9. This would be in line with the assumptions made by ASCE-7 for the ELF procedure. However, aspect ratios above 3.0 showed values that could drop below 0.8, and values below 0.4 for cases with $\alpha = 9$. These buildings exhibited large vertical displacements in the rafters in the first mode, something not accounted for when assigning load using the ELF procedure.

Meanwhile, Langley found that the participation factors for first mode in the transverse direction for their 3D models were between 0.42 and 0.5. The buildings in Langley's study had aspect ratios between 1.3 to 5.3. The 3D models then showed much lower mass participation factor than what would be expected based on the Smith and Uang data.

In order to be able to do a proper comparison, the mass participation factor U_y was computed for both the 2D and 3D models of all the buildings tested. The results are shown in Table 4.5.

From the table it follows that the difference between Langley's values and the ones in Smith and Uang hold true here as well. The 3D models had much lower participation for the

Table 4.5: Modal mass participation ratios for the first mode

Name	α	N^o frames	U_y 3D	U_y 2D
VA-1	2.39	5	0.60	0.86
VA-2	3.74	7	0.60	0.91
WV-1	2.54	8	0.48	0.96
WV-2	3.70	9	0.40	0.85
NC-1	3.70	9	0.22	0.86
NC-2	2.86	7	0.50	0.91
NC-3	1.43	5	0.56	0.87

first mode, with typical values from 0.40 to 0.60, which are consistent with previous work (Langley and Marshall, 2017), if somewhat higher. The one exception to this is building NC-1, which had interior partitions restraining the movement of several frame lines and so the first mode was limited to a relatively small portion of the building.

Similarly, the values obtained for the 2D models are in line with the values expected based on the analysis by Smith and Uang (Smith and Uang, 2013). The main reason why the mass participation factor is so different between the type of model is that they are effectively measuring different things.

The mass participation factor on a 2D frame model is looking at how the horizontal displacement of *a given frame* is explained by the first mode. If U_y is small, applying loads based only on the shape of the first mode may misrepresent the internal forces in the members.

Meanwhile, the U_y for 3D buildings is in large part looking at the system behavior and how the total seismic load effect is transferred into each frame. The reason the value encountered for metal buildings is so low is because of the relatively flexible nature of the roof. Looking for example at the first mode of building NC-2 (Figure 4.55), only approximately half the frames are showing significant displacements. And the walls, which carry a significant amount of mass, are not participating in the mode shape. This also explains why the modal

participation factors for the 3D models here are somewhat higher than the results in Langley and Marshal ([Langley and Marshall, 2017](#)). Their models had hardwalls for cladding instead of metal panels. Since hardwalls are much heavier than the metal panels, the fact that the endwalls do not participate in the fundamental period causes U_Y to be smaller.

In any case, what these low U_y values imply is that the first mode alone cannot be used to assign a distribution of a total base shear to each frame, and also puts into question the use of the fundamental period to define the total base shear. However, due to the flexible diaphragm assumption this distribution is carried out in practice by tributary areas anyway. That assumption implies that each frame is acting independently of each other, and at that point then the results from the 2D analysis would be more relevant for the evaluation of the applicability of ELF than those obtained through a 3D model.

An example of the difference between using tributary areas and accounting for the different modes from a 3D model to define the base shear in each frame line will be shown in [Chapter 7](#).

4.8.4 Influence of purlins and flexible diaphragm assumption

Reasoning behind the use of a 2D model

Though it was mentioned in the previous section that a 2D model can effectively be used to predict the fundamental period of metal buildings, that does not necessarily mean the purlins offer negligible stiffness to the structure. Bajwa et al. applied a point load on the interior frame of a metal building and found that a 2D model of the frame by itself could overestimate the deflections given by a 3D model by 10 to 20% for that loading condition ([Bajwa et al., 2010](#)).

This loading condition was recreated for building NC-2. Building NC-2 was chosen because

of its regular geometry and because the period obtained from the 3D and 2D models were virtually the same. It is then a good case study on how the secondary framing may affect the stiffness.

A unitary point load was applied at the beam column joint of frame line 5. Figure 4.54 shows the deflected shape from a top down view. The first thing that should be pointed out is that essentially only the frame with an applied load is deflecting in a meaningful way. The ratio between the displacement in frame 5 and the second largest displacement (frame 6) turned out to be 40. The model is then behaving in similar fashion. Put another way, the adjacent frame's displacement was 2.5% that of the loaded frame, which is consistent with the results in Bajwa et al. (Bajwa et al., 2010).

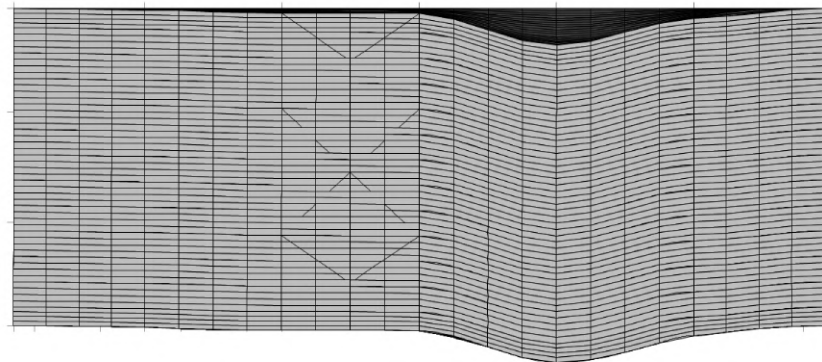


Figure 4.54: Deflections on Building NC-2 to a point load applied at the rafter level of frame line 5.

The displacement of frame 5 was $0.40in$. Meanwhile, that same unit load applied to the isolated frame resulted in a displacement of $0.63in$. The difference between the two values is almost 37%, a ratio similar to the one informed by Bajwa.

The purpose of this analysis was to first show that the 3D models used show similar behavior not only to the new test data, but also to past work done on metal buildings. The second objective was to try and explain why, despite the clear added stiffness due to the secondary

framing, the stiffness taken from a 2D model is a good predictor of the fundamental period. Going back to Figure 4.54, the deflected shape due to a point load is mostly concentrated on the loaded frame. That large relative displacement between frames causes the purlins and girts to try and restrain the displacement.

Meanwhile, the fundamental mode shape of building NC-2 (and in all tested buildings as part of this project) is not associated with the displacement of each frame in isolation, but shows a more global response akin to a distributed loading condition (Figure 4.55). As a consequence, the relative displacement between frames is significantly smaller, and so not much force is being transferred through the secondary framing and the displacement of any given frame is not restrained as much.

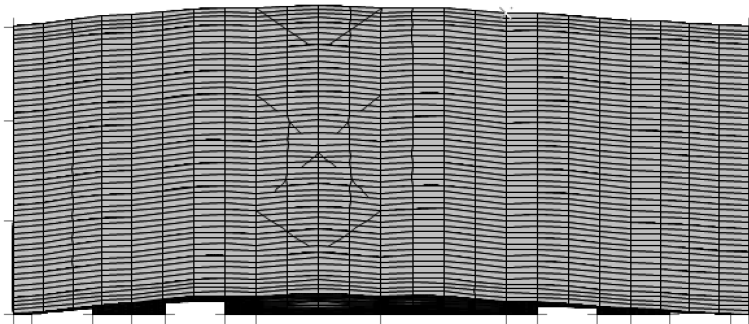


Figure 4.55: First mode of building NC-2 seen from above.

Indeed then, the stiffness of an isolated 2D frame is more representative of the “loading condition” associated with the fundamental mode.

Flexible diaphragm assumption

Though the results in Bajwa et al. (Bajwa et al., 2010), as well as the test results in this work seem to provide significant evidence that the roof diaphragm in metal buildings would be classified as flexible, no formal evaluation as required by ASCE-7 has been done. In this section, this analysis will be carried out for building NC-2 to see whether metal buildings satisfy the limits set forth by ASCE-7 to treat the diaphragm as flexible.

A unit surface load was applied in the transverse direction in all shell elements composing the roof of the buildings. A top down view of the resulting displacements are shown in Figure 4.56. At the end span, the deflections are $0.1858in$ on the endwall and $1.1484in$ on frame line 2.

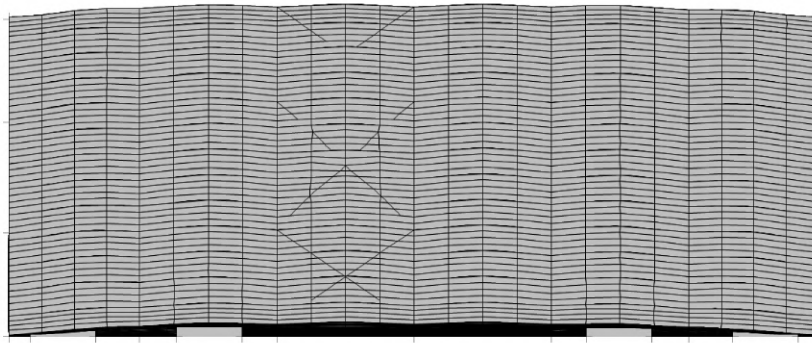


Figure 4.56: Deflections due to a surface unit load applied to the roof diaphragm.

The average drift can then be computed as

$$\Delta_{ADVE} = \frac{0.1858 + 1.1484}{2} = 0.667in \quad (4.1)$$

Meanwhile, the maximum displacement of the diaphragm, which occurs roughly at midspan between the endwall and frame line 2, is $1.1277in$. Then, the maximum diaphragm deflection is

$$\delta_{MDD} = 1.1277 - 0.667 = 0.461in \quad (4.2)$$

from which the ratio can be finally computed

$$\delta_{MDD}/\Delta_{ADVE} = 0.461/0.667 = 0.69 < 2 \quad (4.3)$$

which is smaller than 2. As such, the diaphragm would not qualify as flexible. This calculation was redone without the shell elements for the roof and instead introducing the load as a linearly distributed in each purlin. The ratio between the maximum “diaphragm” displacement and the average drift of the frames was 1.2, larger than before but still significantly below 2.

This means that, despite the very low diaphragm stiffness of the roof, due to the flexible nature of the main frames the diaphragm would qualify as semirigid as per ASCE-7. Given that metal buildings have historically been built using the flexible diaphragm action this result should not be taken at face value as an indication the metal buildings should be modeled with a 3D diaphragm.

However, some early signs that the diaphragm would not qualify as flexible could be taken from the mode shapes shown in this chapter. Were the diaphragm to be truly flexible, then several closely spaced (or even identical for regular structures) modes representing the individual movement of each frame would appear. Instead, as seen in Figure 4.55 for Building NC-2 and other buildings as well, the modes exhibit signs of global behavior, similar to a beam supported by the endwalls.

How this behavior affects load distribution for seismic design, and possible shortcomings of assigning load based on tributary areas will be discussed in Chapter 7.

4.8.5 Revisiting the VTH and BBTC buildings

Finally, it is interesting to compare how the results from the tests in this project compared to those by Kumar et al. (Kumar et al., 2020). In their report, 6 metal buildings were tested, and the results were compared against both the ASCE-7 and Smith and Uang prediction equations, with most of the buildings exhibiting significantly shorter periods than as predicted by Smith and Uang.

In this test we've seen so far that both 3D and 2D modeling of structures can provide accurate fundamental period estimations. In light of this, it was decided to revisit two buildings in the report for which member sizes were available, the buildings named BBTC and VTH.

2D Models were created for both buildings following the same procedure as for the rest of the buildings in this work. The results are summarized on Table 4.6

Table 4.6: Summary of tests done on fully clad buildings

Name	T_{2D} [s]	T_{test} [s]	ΔT [%]
BBTC	0.52	0.50	4
VTH	0.64	0.39	64

The BBTC building shows excellent agreement between the 2D model and the test data, while the VTH prediction was off by about 60% similar to buildings WV-1 and VA-3. In fact, if the latter model is updated with the column base designed as fixed, the estimated period becomes 0.42s which is within 8% of the experimental result.

In order to check if vibration amplitude could be the cause of the apparent fixity of the base, two sets of tests were carried out on the VTH building. A free vibration test, done by closing and opening the mechanical hangar door at one of the endwalls, and also an ambient vibration test.

Figure 4.57 shows the free vibration response of the center interior frame after the door was

closed. The acceleration amplitude was 2 orders of magnitude larger than the corresponding free vibration test in Kumar et al. (Kumar et al., 2020). However, from the frequency response it can be seen there was no shift in natural period, with the first mode as obtained through the SSI algorithm being 2.55Hz (0.39s). This is the exact same result as the ambient vibration tests done by Kumar et al. and also for this report. Given that the results are identical to those from 2019, they will not be included here.

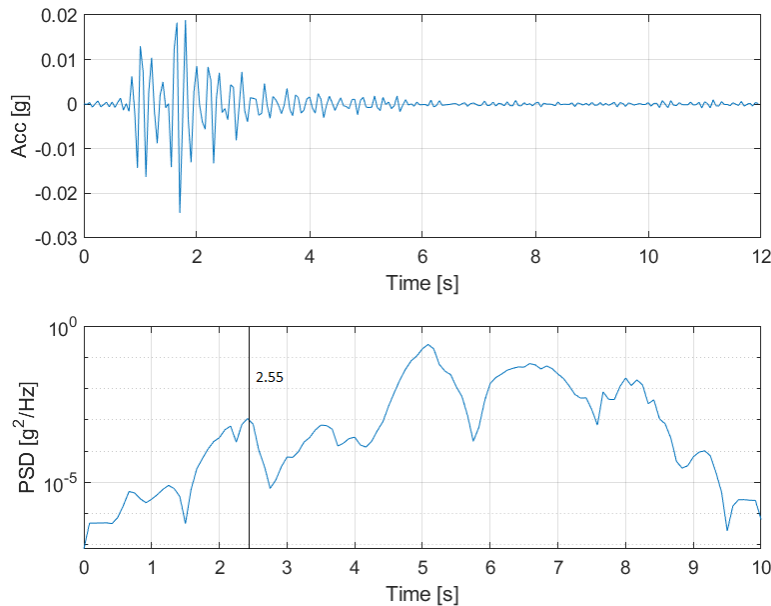


Figure 4.57: Acceleration data from middle interior frame of the VTH building during the free vibration test.

The main conclusion here, however, is that the natural period of the building did not seem to change with amplitudes ranging from $0.0005g$ during the ambient vibration test to $0.02g$ during the free vibration tests. It's worth noting that both cases had amplitudes much lower than what was measured by Goel and Chopra (Goel and Chopra, 1997), which reached values of $0.15g$.

In that case, then, future work should focus on understanding why certain base to column connections exhibit large amounts of rotational stiffness compared to others, and if the initial

stiffness captured here is representative of the base conditions for a large earthquake.

As a summary though, the test results from Kumar et al. ([Kumar et al., 2020](#)) for are consistent with the results reported in this chapter. In the next chapter, the Smith and Uang period formula will be evaluated and compared to both the experimental data collected, as well as the different models created for each building.

Chapter 5

Evaluation of the Smith and Uang Equation

In the previous chapter the results from the experimental campaign were described in detail and compared to analytical models of the builds to validate some of the assumptions made when modeling metal buildings. Other important results regarding the behavior of metal buildings were investigated. More importantly, though, it largely served as a validation of the modeling approach used by Smith and Uang ([Smith and Uang, 2013](#)) to generate a metal building data set, from which their fundamental period equation formula was derived.

This chapter will then focus on whether the equation itself provides good estimates of the fundamental period of the tested buildings, and whether those results are enough to fully validate the equation.

5.1 Fundamental period comparison with best guess weight

For reference, the Smith and Uang period formula – meant to be a lower bound estimate – will be shown again. The natural period of a metal building with an aspect ratio α , mean roof height (in inches) H and seismic Weight (in kips) W can be first estimated as

$$T_1 = \begin{cases} 0.058 (WH)^{0.3} & \alpha \leq 3 \\ 1.58W^{0.16}/\alpha & \alpha > 3 \end{cases} \quad (5.1)$$

If the lateral stiffness k_{lat} of the frame is known, the following expression can be used which is based on Rayleigh's method as provided by Smith and Uang

$$T_2 = 2\pi \sqrt{\frac{W/g}{k_{lat}}} \left(1 + \frac{\alpha^{2.5}}{425} \right) \quad (5.2)$$

Table 5.1 shows the fundamental period obtained based on experimental testing, T_{test} , the period from the 3D and 2D models, T_{3D} and T_{2D} , the prediction from ASCE-7 T_{ASCE} and the periods T_1 and T_2 from the equations above. The values of α , W and H are also shown for reference.

Table 5.1: Fundamental period of tested buildings using different methods

Name	W [kips]	H [in]	α	k_{lat} [kip/in]	T_{test} [s]	T_1 [s]	T_2 [s]	T_{2D} [s]	T_{3D} [s]	T_{ASCE} [s]
VA-1	5.3	276	2.39	3.48	0.43	0.52	0.40	0.42	0.42	0.34
VA-2	11.5	250	3.74	11.72	0.31	0.62	0.34	0.33	0.32	0.32
WV-1	9.5	378	2.54	1.82	0.38	0.68	0.75	0.75	0.73	0.44
WV-2	11.4	324	3.70	2.25	0.72	0.63	0.77	0.69	0.65	0.39
NC-1	7.0	259	3.70	3.07	0.50	0.58	0.51	0.50	0.45	0.33
NC-2	5.2	252	2.86	1.59	0.63	0.5	0.60	0.60	0.60	0.32
NC-3	1.8	168	1.43	2.65	0.15	0.32	0.27	0.28	0.25	0.23

Note that the period obtained using the Goel and Chopra (Goel and Chopra, 1997) equation remains largely constant for all buildings, as its only dependent on height. Given the large range these buildings exhibit despite their similar height, it can be concluded that the current provisions are not accurate for metal buildings, as first shown by Kumar et al. (Kumar et al., 2020). The above results are shown in a more streamlined format in Figure 5.1, showing the

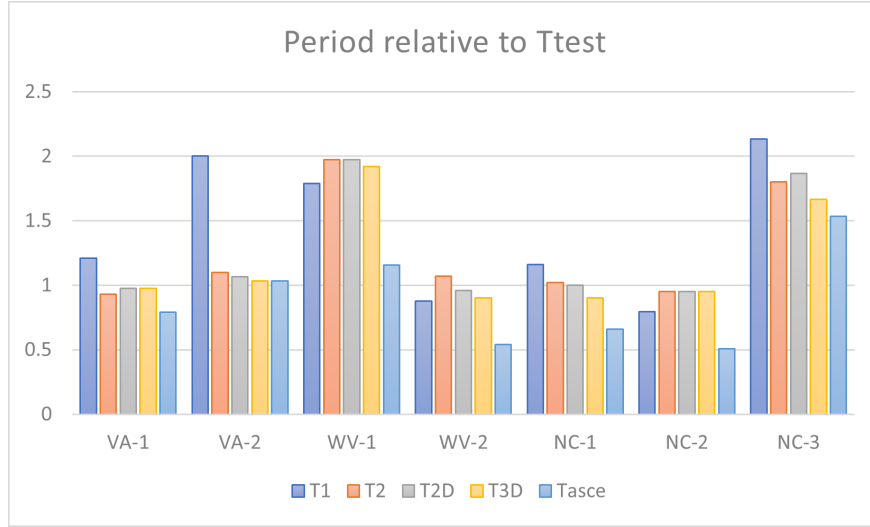


Figure 5.1: Comparison between the different period estimates (relative to T_{test})

different periods predictions normalized by the value of the test results.

Excluding the buildings that exhibited large rotational stiffness at their base (WV-1 and NC-3), it's clear from the above results that both the 2D and 3D models match very well with the measured response, as discussed in the previous chapter. More importantly, the refined equation to obtain the period T_2 shows excellent correlation with the full dynamic analysis (T_{2D} and T_{3D}). This means that the period could be estimated only by modeling an isolated 2D-frame, and a simple static analysis to determine its stiffness can be used coupled with Equation 5.2. Not having to run a dynamic analysis means that it becomes unnecessary to discretize the elements in between joints and assign masses in correspondence to the tributary loads, which simplifies the modeling.

However, even though the refined estimation does a very good job of predicting the natural period, the base prediction from using Equation 5.1 seems to over predict the measured period and, in general, the results of the modeled periods as well. This is concerning because the Smith and Uang equation is not meant to predict the period, but to provide a lower bound. The Smith and Uang equation only provided a lower bound (ratio < 1 in Figure 5.1)

of the tested period in 2 out of 7 buildings, and only was below the refined estimate in 3 cases.

There are some outliers in the dataset that worth discussing however. As mentioned before, buildings WV-2 and NC-3 were showing a fixed base behavior and so naturally all predictions were significantly off. Even the ASCE-7 formula, which sometimes under predicted the period by a factor of 2 (WV-2, NC-2), was not providing a conservative lower bound. Though this may not have major implications in design (as using the ASCE-7 equation for metal buildings general puts the building in the plateau of the spectral acceleration plot) currently, adopting the Smith and Uang equation may lead to underestimating the base shear. It must be highlighted again, then, that further studies need to be done to understand why some base to column connections show increased rotational stiffness, whether this stiffness stays constant for larger amplitudes of shaking, and whether this ultimately has consequences in terms of reliability.

The other major outlier is building VA-2. Figure 5.1 shows that, despite the models and the refined prediction doing a great job estimating the observed period, Smith and Uang's formula was off by a factor of 2, when in the other cases the difference was within 20%. The main reason for this is that building VA-2 had appendices in every interior frame, essentially creating a 2-bay frame. It could also be thought of as a modular metal building with a *fixed* connection at the top, whereas all the Smith and Uang models assumed any interior column to be a gravity column. T_{2D} , T_{3D} and T_2 all take into account the appendix in their formulation, while T_1 does not. This is a limitation of the Smith and Uang (and any other potential) formula, and should be properly acknowledged if the equation ends up being adopted by building codes.

Also, a minor note should be made regarding building NC-2. This building had a aspect ratio of 2.84, which is very close to the cutoff point of 3 where the expression to estimate

the period changes. As mentioned in the literature review, this causes a discontinuity in the predicted period. For this building for example, the value using the “incorrect” equation would lead to period of $0.72s$, which is 44% larger than the value of $0.5s$ obtained considering $\alpha < 3$. This again shows that this discontinuity should most probably be revised.

5.2 Fundamental period comparison with design weight

Based on the results of the previous section, it would seem at first glance that the Smith and Uang formula is not providing the intended lower bound estimate for metal buildings. However, it should be noted that all buildings were designed for much higher loads than those present at the time of testing. It is generally the case that the dead loads used in design will be somewhat higher than those seen in service. For example, building NC-1 was designed to accommodate the installation of solar panels in the future, which resulted in a collateral load of $7psf$.

This may affect the results because, looking at Equation 5.2 and based on structural dynamics theory (Chopra, 2017), the period of a structure increases with the square root of the mass. Meanwhile, the Smith and Uang formula, as shown in Figure 5.1 scales with the $W^{0.3}$ or $W^{0.16}$, depending on the aspect ratio. The discrepancy in scaling is because the Equation is, in some fashion, trying to estimate the stiffness of the structure in order to provide a fundamental period, and the stiffness also tends to increase with W as the member sizes get larger to deal with higher dead loads.

It is possible then, that considering the best estimate of the building mass (i.e.: the mass present during testing) in equation 5.1 would be providing a lower bound estimate of the period for a building designed for these lower loads, which would be more flexible than the actual building tested. The refined equation is not affected by this as it uses the actual

frame stiffness.

It was deemed more appropriate, then, to do a comparison between the predictive equation and the refined expression when accounting for a seismic weight closer to its design value (as close as possible given the available documentation). The use of the refined equation is justified based on the previous section, which showed excellent correlation between T_2 and the periods from the models.

Table 5.2 shows the results when the collateral load adopted for design is included in the seismic weight. The collateral load D_c was taken from the design documents for each building and is presented in the Table as well. Only buildings VA-1, VA-2, WV-2, NC-1 and NC-2 are shown, as these buildings showed very good correlation between the test data and the models, which provides confidence in extrapolating the period for a larger weight.

Table 5.2: Fundamental period of tested buildings using different methods

Name	D_c [psf]	W [kips]	T_1 [s]	T_2 [s]	T_{ASCE} [s]	T_1/T_2
VA-1	3	9.4	0.61	0.54	0.34	1.13
VA-2	5	24.5	0.70	0.49	0.32	1.43
WV-2	2	16.4	0.67	0.92	0.39	0.73
NC-1	7	21.0	0.77	0.89	0.32	0.87
NC-2	3	9.7	0.60	0.81	0.32	0.73

The results when accounting for the design level weight paint a different picture. As expected, the Smith and Uang formula is still overpredicting the period for building VA-2, due to the presence of appendices that are were not part of their modeling. However, for buildings WV-2, NC-1 and NC-2 the values obtained using Equation 5.1 are shorter than those of the extrapolated test results. In those cases, then, the Smith and Uang equation is indeed providing a lower bound of the natural period.

It is possible to convert the lower bound estimate to a best guess estimate by multiplying the period by $\sqrt{C_u}$, with $C_u = 1.6$ (Smith and Uang, 2013). By doing so for buildings WV-2, NC-1 and NC-2, the “best guess” estimate from the Smith and Uang formula would be $0.85s$, $0.97s$ and $0.76s$ respectively. These values all fall within 10% of the extrapolated experimental results, with the periods for buildings WV-2 and NC-2 being slightly underpredicted and the period for building NC-1 slightly overpredicted.

In those three cases, then, not only is the Smith and Uang predictive equation providing a good lower bound estimate, its best guess estimate is also quite accurate. Though the latter result is not important for design purposes as the “best guess” estimate is not used, it does show that the building tested fall close to the original regression line which led to the predictive equation.

For VA-1, however, the lower bound estimate proved to be overpredicting the period, being 10% larger than the extrapolated period considering the design loads. Statistically, it would be expected for some of the buildings to fall outside the defined bounds, so no real conclusions can be taken from this case.

Finally, looking at Table 5.2 it’s clear that using the equation in ASCE-7 can result in excessively short periods, and is not adequate for metal buildings.

All in all, when accounting for the design level loads, the results from the Smith and Uang formula seemed to provide reasonable lower bounds estimates for the buildings that fell within the scope of their data set, as long as the column bases behaved as pinned. However, it should be noted that those only represent four out of the 7 buildings tested for this project.

5.3 Comparison between the synthetic data set and the tested buildings

5.3.1 Building classification

It should be understood that the results presented here apply to the set of buildings that were tested, which may not necessarily be representative of the complete field of metal buildings that were included in Smith and Uang's research.

The buildings in Smith and Uang's data set can be classified (beyond their weight, aspect ratio and height that is) by the following properties

1. Cladding type: Metal Panels (MP) or Concrete (C)
2. Roof type: Monoslope (M) or Gabled (G)
3. Structural system: Clear Span (CS) or Modular (MO)

with the difference between clear span and modular buildings being the presence of interior gravity columns. Given that the final design of a metal building may be governed by different load combinations depending on its location, two more classes were evaluated in accordance with the loading conditions

1. Seismic Load: Low (LS) and High (HS)
2. Wind Load: Low Wind (LW) and High Wind (HW)

where classes L and H are associated with a spectral acceleration for short periods of $0.17g$ and $1.0g$ respectively, and classes LW and HW with basic wind speeds of $85mph$ and $120mph$

respectively, with these values arbitrarily chosen by Smith and Uang so as to cover different extremes of ASCE-7 hazard maps. Table 5.3 shows how the tested buildings are classified as per the above.

Table 5.3: Classification of tested metal buildings

Name	MP/C	M/G	CS/MO	LS/HS	LW/HW
VA-1	MP	G	CS	LS	LW
VA-2	MP	G	CS	LS	LW
WV-1	MP	M	CS	LS	LW
WV-2	MP	G	CS	LS	LW
NC-1	MP	M	CS	LS	LW
NC-2	MP	M	CS	LS	LW
NC-3	MP	M	CS	LS	LW

From the table it becomes clear that some building types were not covered by the tests carried out in this project. A similar conclusion can be reached for the work done by Kumar et al. (Kumar et al., 2020). In the end, there is no available test data for buildings with concrete walls, no data for modular buildings, and no data for buildings in either high wind or high seismic areas. This means that the observations made in this project are only valid for a (potentially) small percentage of the total building population.

Based on the above classification, only two combinations of buildings were tested: clear span buildings in low wind and seismic regions with metal panel cladding and a gabled roof, and the same buildings with a monoslope roof. Out of the 192 buildings in the Smith and Uang dataset, only 4 and 6 buildings meet each criteria, respectively, which is less than 3%.

Smith and Uang used weighted linear regression, so it could be argued that the sum of the weights of those buildings should be used. In which case, then these classes comprise 5% and 3% of the population. However, it should be noted that between this work and the work of Kumar et al., effectively more buildings with these characteristics have been tested than similar data points in the Smith and Uang’s predictive equation.

Either way, the number is indeed very low to say the tests results are representative of the buildings covered by Smith and Uang’s formula.

5.3.2 Differences with building classification

Based on the previous section it would seem that the tested buildings comprised only a very small portion of all metal buildings. However, this could be virtue of setting too many classifiers that may not have an impact on the natural period prediction. To that end, the ratio between the period obtained by the 2D models developed by Smith and Uang, T_{2D} and the period resulting from applying their predictive equation, T_1 will be compared between building types.

Since it’s not possible to compare buildings with the same dimensions and weight but different classifications, the analysis will be carried out by looking at the difference in average of each type of building. First, Figure 5.2 shows the cloud points for the data set split according to the different classifications based on structural characteristics.

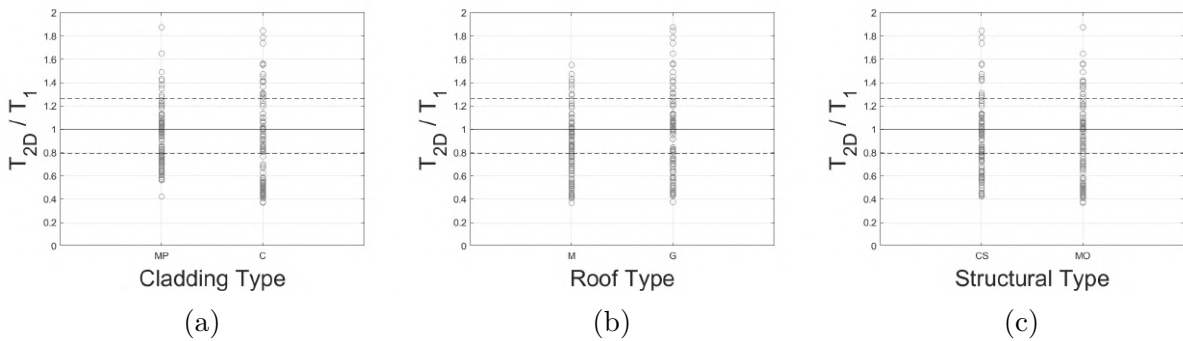


Figure 5.2: Ratio between model and predicted period based on different classifiers for the Smith and Uang data set.

Based on the plots, it seems that the type of roof and whether the structure is modular or clear span does not have a significant effect on the period of these structures, meaning these classes could be merged together. However, when looking at the cladding type there’s

a cluster of data points at $T_{2D}/T_1 = 0.4$ for class C that is not present for class MP. In turn, it was decided to treat buildings with concrete walls and metal panels separately.

When accounting for this merger, then the tested structures go on to represent 27% of all buildings in terms of their type and loading condition.

5.3.3 Differences with loading conditions

The loading conditions may also have a significant effect on the period of metal buildings. For buildings with metal panels, given their relatively low weight and lack of drift requirements, it was assumed that, whenever high wind loads were present, then the wind loads were controlling the design. Meanwhile, in low wind regions, it was assumed that seismic would control in high seismic regions and dead load otherwise. This creates three mutually exclusive groups, defined as follows:

1. MPL: buildings with metal panels in both low seismic and wind regions
2. MPH: buildings with metal panels in high wind regions
3. MPM: buildings that don't qualify for either MPL or MPH (buildings in low wind and high seismic regions)

For buildings with concrete panels, the opposite was assumed. Given their heavier nature and the inclusion of drift limits in their design (at least, in Smith and Uang's database), it was assumed that seismic controlled in all high seismic regions, and to treat high wind and low seismic regions as the intermediate case. The classification is then as follows:

1. CL: buildings with concrete walls in both low seismic and wind regions

2. CH: buildings with concrete walls in high seismic regions
3. CM: buildings that don't qualify for either CL or CH (buildings in high wind and low seismic regions)

Figure 5.3 shows how the ratio between the modeled period and the prediction changes for each of these groups. For buildings with concrete walls, the groups are clearly separate from each other, with the period of the CL class being underestimated (ratio larger than one) and the CH class being severely overestimated (ratios lower than 0.8). In fact, almost all buildings in the CH class fall below the dotted line at around 0.8, which means that they all have shorter periods than what even the lower bound estimate is predicting. This is extremely concerning as it is precisely the buildings in high seismic regions the ones to be most affected by seismic loads, and overpredicting the period would result in underpredicting the seismic loads which would probably control the design.

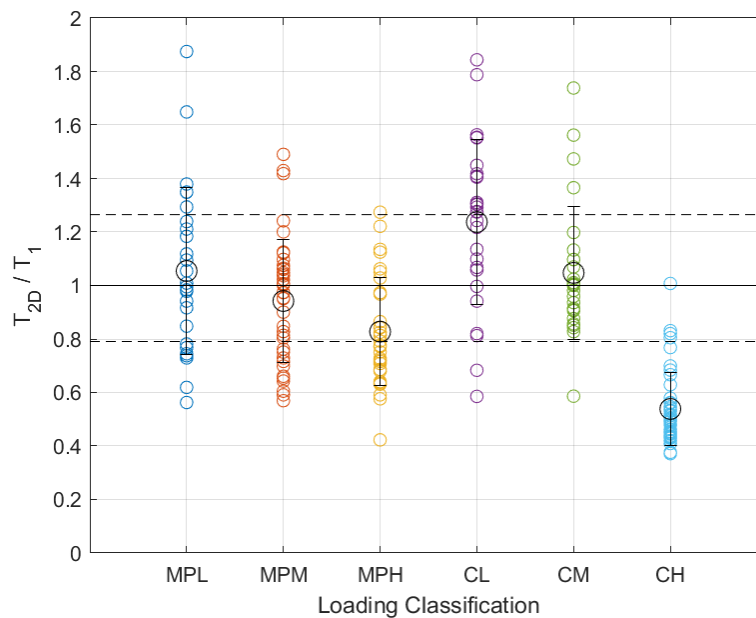


Figure 5.3: Ratio between model and predicted period based on loading conditions

A similar effect can be seen for buildings with metal panels, though not as pronounced. The periods of buildings in high wind regions is, on average, underpredicted by 20%, and about half of the data points have periods shorter than the lower bound. For this class, however, wind is expected to control over seismic and so whether this result is significant can be argued. As for Classes MPM and MPL, these are relatively similar to each other. It seems, then, that the equation is providing accurate results for buildings in low wind regions in general and these two classes could be grouped together.

Considering groups MPL and MPM to be roughly equal, and accounting for the analysis in the previous subsection, the buildings tested in this project represent 70% of all buildings in the set (summing the weights of 49 buildings in the set). Note that this number is only with respect to building classification.

5.3.4 Geometric parameters

Another point of interest is whether the geometry of the tested buildings covers in reasonable fashion the wide range of possible building designs. This will be done based on the three fundamental parameters that are needed to estimate the period as per Equation 5.1: The mean roof height H , the seismic weight W and the aspect ratio α . Given that the predictive equation is in reality two different expressions – one dependent on W and H for $\alpha < 3$, and another dependent on W and α for $\alpha > 3$, two plots are presented that show the combination of the variables that play a part in each respective equation (Figure 5.4). The gray circles are data points from Uang and Smith, the blue triangles are the buildings tested by Kumar, and the red squares are buildings tested for this project. Note that the seismic weights plotted for the new tests are using the design level loads and not the “best guess” estimate during testing.

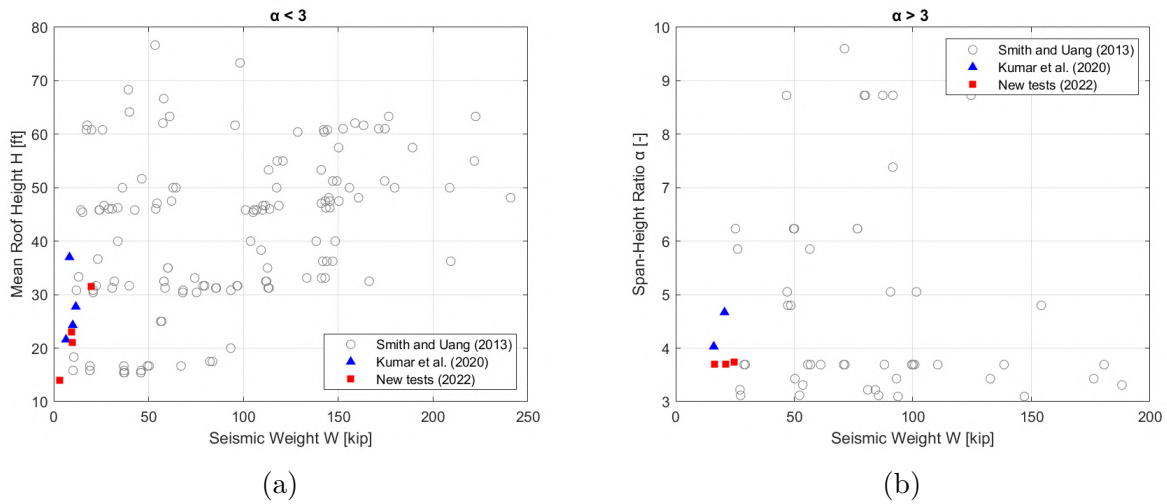


Figure 5.4: Scatter plot showing the geometric properties of different buildings.

It becomes immediately clear that the tested buildings do not cover the complete parameter space included in Smith and Uang’s database. The largest difference is in the seismic weight. The tested building had weights ranging from $3kip$ to $25kip$. Most of the buildings in Smith and Uang extend past that, with weight $50kip$, $100kip$ and up to $200kip$. The reason for this is two-fold. On one hand, some of the buildings in Smith and Uang were designed for a flat roof snow of $40psf$, which means that a portion of the snow mass had to be included in the seismic weight as per ASCE-7. Similarly, buildings with concrete walls would generally have larger seismic weight as well.

On the other hand, the total length of modular buildings can be significantly larger than that of clear span buildings. Total lengths of $240ft$ and $300ft$ were identified when going through the database. Given the lengths of these buildings is almost triple what was measured both in these projects and by Kumar, it follows as well that their weight would be larger in similar scale.

Similar shortcomings can also be observed for the mean roof height and aspect ratios covered by the tests. Aspect ratios above 5 do not seem to be common, but a significant number of

buildings in the database have mean roof heights above $40ft$, which was the tallest building tested. Future work should focus on covering a higher range of heights and weights to cover the full spectrum of metal buildings.

As mentioned before, Smith and Uang weighted their buildings based on their statistical likelihood. These weights were assigned based on feedback by an industry expert, who established frequencies based on the production history of their company (Smith, 2013). Considering these weights, and assuming that the tested buildings are representative of any building with weight less than $25kip$, mean roof height lesser than $40ft$ and aspect ratios smaller than 5, the tested buildings represent 46% of the building database based on geometry alone.

5.4 Summary and Discussion

In this chapter the results of the experimental testing work were compared to different period estimation equations: The predicted equation by Smith and Uang (Smith and Uang, 2013), their refined equation if the lateral stiffness known, and the ASCE-7 equation. From the comparison it followed that the Smith and Uang predictive equation can provide a lower estimate for metal buildings with metal panels for cladding as long as the column bases exhibited pinned behavior and the frames were free of appendices. However, that was not the case for two of the buildings in this test set, as well as the VTH building in Kumar et al. (Kumar et al., 2020), which seemed to show fixed base supports. The reason as to why this happens is not clear, but nonetheless is a significant road block as it can shorten the building's period by a factor of 2.

The refined equation was shown to have excellent correlation with test results, and is an excellent alternative in lieu of performing modal analysis of 2D or 3D models. ASCE-7's

equation was consistently underpredicting the period in most cases, which reinforces the need for a specific equation for metal buildings.

The test set available after this project still falls short of covering the complete building space used by Smith and Uang. Based on building classification and loading conditions, the test set represented about 70% of the built environment. Doing the same for the geometry of the buildings, about 46% of all buildings were covered by this test. When combining both criteria, the tested buildings represent only 35% of all metal buildings, according to the weights used by Smith and Uang (Smith and Uang, 2013). This means a large portion of metal buildings are still unaccounted for.

More importantly though, the tests are limited to buildings with $W < 25kip$, $H < 40ft$ and $\alpha < 5$ which is only a fraction of what the Smith and Uang formula intends to cover. That means, that, beyond what percentage of metal buildings fall under the test scope, it should be made clear that the results cannot be extrapolated to buildings with larger spans, heights and aspect ratios, nor to buildings in high wind regions or with concrete walls.

A look at the different building types and loading conditions showed the fundamental period of buildings with concrete cladding can differ significantly from those with metal panels. Especially for the former, high loading conditions (in this case, defined by high seismic loads) can result in much stiffer structures due to drift limitations. This, in turn, makes the predictive equation by Smith and Uang not suitable to estimate their period. Almost all buildings falling under this category had periods shorter than the lower bound estimate, which would underpredict the base shear.

Given that estimating the period becomes more important in regions of high seismic risk, it is fair to ask why include buildings in low seismic regions to develop the equation, especially for the case with concrete walls where the stiffness difference appears to be significant. The

equation in ASCE-7, for example, was developed by measuring buildings in California (Goel and Chopra, 1997), Including buildings from low seismic regions would result in a more scattered data set, as well as an overall overestimation of the period, which is unconservative for design.

For metal buildings, the difference between loading conditions is not as clear. Generally speaking, though, whether a single formula can be used to describe buildings with such different characteristics should be debated. It would probably be more adequate to only consider structures in high seismic regions, and also split the results between buildings with concrete walls and those with metal panels.

Finally, a note should be made about the use of weighted linear regression for the development of the equation. Including weights in the regression, as argued by Smith and Uang (Smith and Uang, 2013), ensures that buildings that are more common are estimated better than outliers. However, the weights used should be carefully considered.

In the Smith and Uang's database, Frame 97 (a gabled, modular frame with metal panels, $H = 15\text{ft}$ in a low wind, high seismic region) has a weight of 0.32, meaning that a single data point out of all 192 buildings represents 32% of the population. The next highest weight is 6%. This has the potential to significantly bias the results.

For example, the sum of the weights of all buildings with concrete walls in high seismic regions – which are the most sensitive type of metal buildings to earthquake loading – is 2.6% (from 43 data points). To offer a comparison, there are 7 buildings in the data set that *on their own* have a larger weight. This explains in large part why the predictive equation performs poorly for the buildings labeled as CH, as they carry almost negligible weight in the regression. The weighting function, if buildings of all types are to be included in one single equation, should probably be revised so that the impact an estimation error could have on

the safety of the structure is accounted for. That is, how critical the period estimation is for the design of the structure.

Chapter 6

Development of new period prediction formulas

6.1 Introduction

The analysis from the previous chapter showed that the assumptions Smith and Uang made to develop their synthetic database are reasonably accurate and adequately represent the natural period of metal buildings (at least buildings with metal panels, based on the limited experimental data). However, though their proposed equation does provide a lower-bound estimate for regular buildings with metal cladding, the equation may overpredict the period of buildings with concrete hardwalls. The reason for this was two-fold: first, due to the use of a single equation to describe buildings with very different properties and design requirements, and second due to the use of a weighted linear regression that effectively ignored the data from buildings with concrete cladding in high seismic regions. Building NC-2, which had a height of span-to-height to ratio near 3, where the piecewise function for the prediction became non-continuous, also showed the necessity to address said discontinuity.

Similarly, the evaluation of the data set showed that the building location plays a significant role in the building period, with buildings in high seismic regions having shorter periods. Since the equations in ASCE-7 were developed from tests done in California, it is probably more appropriate to only consider buildings in high seismic regions for the development of a

predictive equation that is consistent with the rest of the building code.

In this Chapter, a new set of predictive equations will be proposed that addresses this drawbacks, by using only data from buildings in high seismic regions and by separating buildings with metal panels from those with concrete hardwalls.

6.2 Rational analysis for determining the equation type

Similar to the work by Goel and Chopra ([Goel and Chopra, 1997](#)), it was decided that the best approach to develop a new equation was to first obtain a rational expression to determine the period. In their case, by assuming the mass was evenly distributed across each floor and using Rayleigh's method assuming a linear first mode shape they found that the period of a multi-story building could be mostly predicted by its height h . For a single-story building controlled by seismic loading, as shown by Lamarche et al., the natural period could also be largely be described by the height ([Lamarche et al., 2009](#)). An equation of the type

$$T_a = a h_n^b \tag{6.1}$$

with h_n being the mean roof height (in inches), and constants a and b would probably be adequate for buildings with concrete hardwalls in high seismic regions.

The design of metal buildings with metal panels, however, is essentially controlled by the gravity loading. As such, the lateral stiffness would be largely independent of the building height. In turn, a new equation type should be formulated for them.

In order, to find the parameters that best describe the natural period of buildings with

metal panels, the lateral stiffness of a single story clear span frame was evaluated. As this is only meant to be simplified analysis, for the purpose of calculating the lateral stiffness the following assumptions were made:

- Frame elements are axially rigid, and shear deformations can be ignored
- Columns are ideally pinned at the base
- The cross-sectional properties EI of beams and columns are constant along the length and equal to each other
- The roof is perfectly flat (monoslope roof with no pitch)

Figure 6.1 shows a schematic view of the frame with height h , span L and cross-sectional properties EI , along with the resulting moment diagram when a unit load is applied at the rafter level (note that, due to the axial rigidity assumption, where that load is applied along the rafter does not affect the results). Interestingly, the moment diagram (and thus, the deformed shape as well) is anti-symmetric, and there would be no vertical displacement at midspan due to horizontal loads. This is important because it means that an interior gravity column at midspan would not affect the lateral stiffness of the frame, which gives another degree of confidence that modular buildings and clear span buildings could be mostly grouped together when developing period estimation equations.

In any case, using virtual work the lateral stiffness of the building f_{lat} can be obtained as

$$f_{lat} = 2 \frac{(0.5h)^2 h}{3EI} + 2 \frac{(0.5h)^2 (0.5L)}{3EI} \quad (6.2)$$

If instead of the span L , the span-to-height ratio $\alpha = L/h$ is used, then the flexibility can be expressed as

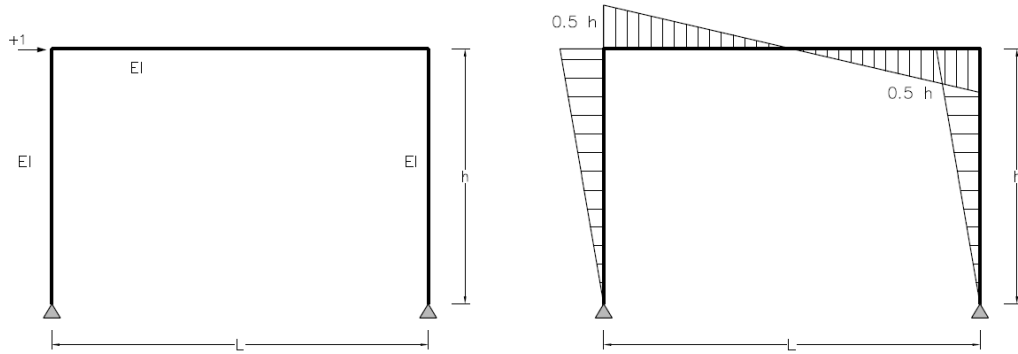


Figure 6.1: Simplified analysis of a single-story moment frame

$$f_{lat} = \frac{h^3}{6EI} (1 + 0.5\alpha) \quad (6.3)$$

However, the design of these buildings is controlled by their dead weight, where the maximum moments increase with the square of the length and height, with the moment of inertia needing to increase at the same rate to keep stresses below a given threshold. As a simplification, we can assume then that the stiffness will be a function of $(1 + 0.5\alpha)^2$ based on the above. As such, then the lateral flexibility would be approximately

$$f_{lat} \propto \frac{1}{(1 + 0.5\alpha)} \quad (6.4)$$

effectively inverting the relationship between the flexibility and the span-to-height ratio. Remember as well, that the lateral stiffness K_{lat} is the inverse of the flexibility. Finally, then, for a single degree-of-freedom system the natural period is

$$T = 2\pi \sqrt{\frac{W}{g k_{lat}}} \propto \left(\frac{W}{1 + 0.5\alpha} \right)^{0.5} \quad (6.5)$$

where W is the weight of the building and g is the gravitational constant. Finally, then, the proposed equation is of the type

$$T_a = a \left(\frac{W}{1 + 0.5\alpha} \right)^b \quad (6.6)$$

with a and b calibration constants. Note the new equation is not a function of height h_n (as is Equation 6.1) but of the seismic weight W (in *kip*) and span-to-height ratio. Also, despite having two variables instead of a single one, it still only has two constants that need calibration. Both equations are suitable for power regression, similar to the equations in ASCE-7.

6.3 Linear regression analysis

Out of the 192 buildings in the Smith and Uang data set, 39 were identified as buildings with metal panels, and 44 as buildings with concrete hardwalls, both in high seismic regions. The number of buildings in each case is close to those used in similar studies to develop period estimation equations (Goel and Chopra, 1997; Lamarche et al., 2009; Shan et al., 2013). It was decided, unlike Smith and Uang, to perform a standard linear regression, ignoring the statistical weights. First, there wasn't enough confidence in the assigned weights for some of the buildings, as discussed on the previous Chapter. Moreover, a predictive equation should provide a similar level of confidence across the variable space (i.e.: different heights, weights and span-to-height ratios), and so it was believed that a standard linear regression would be more suitable to achieve this over improving the accuracy in a smaller, perhaps more common variable range.

In any case, 5 total equations types were studied, all of them being variations of Equa-

tions 6.1 and 6.6 with different degrees of complexity (such as introducing more calibration constants, or simplifying the relationship between period and α). The adequacy of the calibrated equations was evaluated in two ways. First, through the use of adjusted coefficient of determination R_{adj}^2 . The coefficient determination in this case is a measure of the percentage of the variance in the period that is explained by the selected variables used in the regression. Values close to 1 would indicate a very good fit, and generally speaking high values are desired.

Note that the adjusted value was used over the traditional R^2 because adding more constants will always improve the results, though that doesn't necessarily mean the predictive capabilities of the equation are better. Instead, R_{adj}^2 penalizes equations with more constants in order to be able to compare them to each other on equal ground.

The other way the goodness of fit was evaluated was by the parameter C_u , as used by Goel and Chopra, and Smith and Uang (Goel and Chopra, 1997; Smith and Uang, 2013). C_u is a measure of the dispersion in the data, and is calculated by first linearizing the problem by taking the natural logarithm of both the predicted and model periods, and then evaluating the standard deviation of the error in the estimate s_e . Finally, C_u can be obtained as

$$C_u = e^{2s_e} \tag{6.7}$$

which is, effectively, 2 times the standard deviation of error in the data for a power regression.

Table 6.1 shows the results of the regression for the different equation types that were evaluated. The expressions presented are the best-fit results. The two major takeaways from the table are that, first, the period of metal buildings with metal panels is effectively not a function of height with Equation 6.1 showing the worst coefficient of variation. As Smith and Uang showed before, this is another reason why the ASCE-7 equation is not

suitable for metal buildings and why a new predictive equation is necessary (Smith and Uang, 2013).

Table 6.1: Regression models for metal buildings with metal cladding in high seismic areas.

EQ. Best-fit	R_{adj}^2	C_u
$0.35W^{0.4}H^{0.01}(1 + 0.5\alpha)^{-0.43}$	0.589	1.56
$0.36[W/(1 + 0.5\alpha)]^{0.4}$	0.610	1.54
$0.30W^{0.4}\alpha^{-0.18}$	0.568	1.59
$0.44(W/\alpha)^{0.32}$	0.474	1.67
$0.56H^{0.22}$	0.042	1.99

Perhaps more notable, the equation that performed the best was Equation 6.6, which was developed specifically for single-story buildings designed for gravity loads. What is more, the exponent is 0.43, very close to the 0.5 obtained with a rational analysis. Though the R_{adj}^2 value is low, this about the best fit one can obtain with a limited number of variables. Perhaps more notable, the C_u value is close is essentially 1.6, which is identical to the one found by Goel and Chopra in his study of mid-rise buildings (Goel and Chopra, 1997). Thus, the amount of scatter in the results can be considered appropriate.

Table 6.2 shows the results for buildings with concrete hardwalls. Since the design of these buildings is controlled by drift due to seismic loads, height is indeed the variable that best explains their natural period. Given its simplicity, Equation 6.1 is considered the best equation type for the development of a period estimation formula. Note the much higher R_{adj}^2 value compared to the case with metal panels. The better fit is explained, again, by the controlling load in the design. Buildings with metal panels, as seen in the previous chapter, tend to be controlled either by gravity loading or wind, and so there is larger scatter in the results than for buildings with concrete hardwalls.

Table 6.2: Regression models for metal buildings with concrete hardwalls in high seismic areas.

EQ. Best-fit	R_{adj}^2	C_u
$0.06W^{0.05}H^{0.66}(1+0.5\alpha)^{0.25}$	0.863	1.22
$0.22[W/(1+0.5\alpha)]^{0.35}$	0.457	1.47
$0.11W^{0.45}\alpha^{-0.07}$	0.477	1.47
$0.40(W/\alpha)^{0.20}$	0.332	1.55
$0.10H^{0.61}$	0.818	1.25

6.4 Proposed lower-bound equations

Given the results in the previous section, Equations 6.1 and 6.6 were identified as the best possible expression for a period prediction formula among those evaluated. The expressions shown before were the results of best-guess fit. However, for design we want a lower-bound estimate. Similar to both Goel and Chopra, and Smith and Uang, the lower bound estimates were obtained by dividing the best-guess equation by $\sqrt{C_u}$, which essentially means taking for an estimate the mean value minus one standard deviation. It then follows that the upper bound estimate can be obtained from the lower bound estimate by multiplying by C_u , with the upper bound representing the mean value plus one standard deviation.

Proposed equation for metal buildings with metal panels

Adopting $C_u = 1.6$, the proposed equation for metal buildings with metal panels becomes

$$T_a = 0.28 [W / (1 + 0.5\alpha)]^{0.4}, C_u = 1.6 \quad (6.8)$$

with W being the seismic weight in *kip*, and α the span-to-height ratio as defined by Smith and Uang (Smith and Uang, 2013). Figure 6.2 shows the lower and upper bounds resulting from the proposed equation. The Figure shows that most of the data set in Smith and Uang’s data set falls within the bounds, indicating that the proposed equation does a good job of predicting the natural period of these buildings.

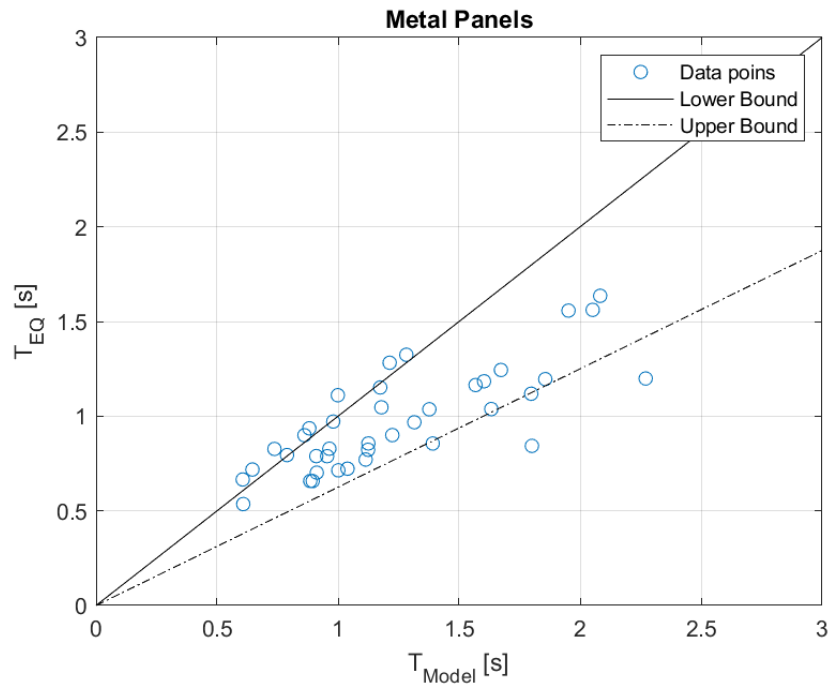


Figure 6.2: Performance of proposed equation for metal buildings with metal panels using Smith and Uang’s data set

Proposed equation for metal buildings with concrete hardwalls

Adopting $C_u = 1.25$, and rerunning the linear regression with the exponent fixed at 0.6, the proposed equation for metal buildings with concrete hardwalls becomes

$$T_a = 0.095h_n^{0.6}, C_u = 1.25 \quad (6.9)$$

with h_n being the mean roof height in *ft*. Figure 6.3 shows the lower and upper bounds resulting from the proposed equation. The Figure shows that most of the data set in Smith and Uang's data set falls within the bounds, indicating that the proposed equation is effective at predicting the natural period of these buildings.

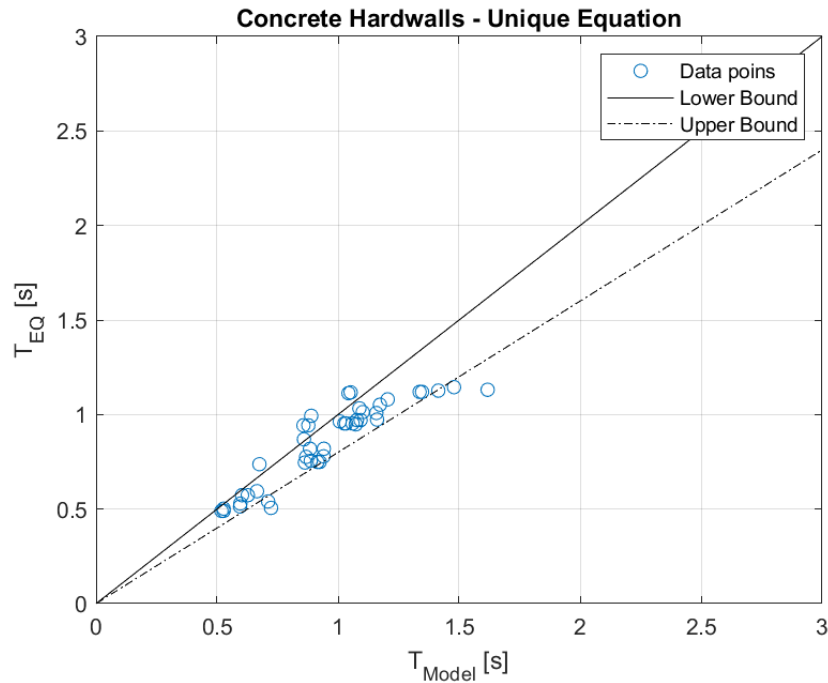


Figure 6.3: Performance of proposed equation for metal buildings with concrete hardwalls using Smith and Uang's data set

Alternate expression for buildings with concrete hardwalls

The possibility of merging both equations into a single equation was also evaluated in order to streamline its application in practice. To that end, Equation 6.6 was calibrated with a fixed value of $b = 0.4$ (identical to the one obtained for metal panels). The resulting best-fit equation becomes

$$0.18 [W / (1 + 0.5\alpha)]^{0.4}, R_{adj}^2 = 0.449, C_u = 1.46 \quad (6.10)$$

which is effectively the result obtained from metal panels divided by a factor of 2. Thus, the period estimation equation for buildings with metal panels could be used for buildings with concrete cladding reducing the result in half. As shown in Figure 6.4, the alternative proposal results in larger scatter, also verified by the low R_{adj}^2 value of 0.449. Despite this, adopting $C_u = 1.6$, as used for buildings with metal panels causes most data points to still fall within the bounds.

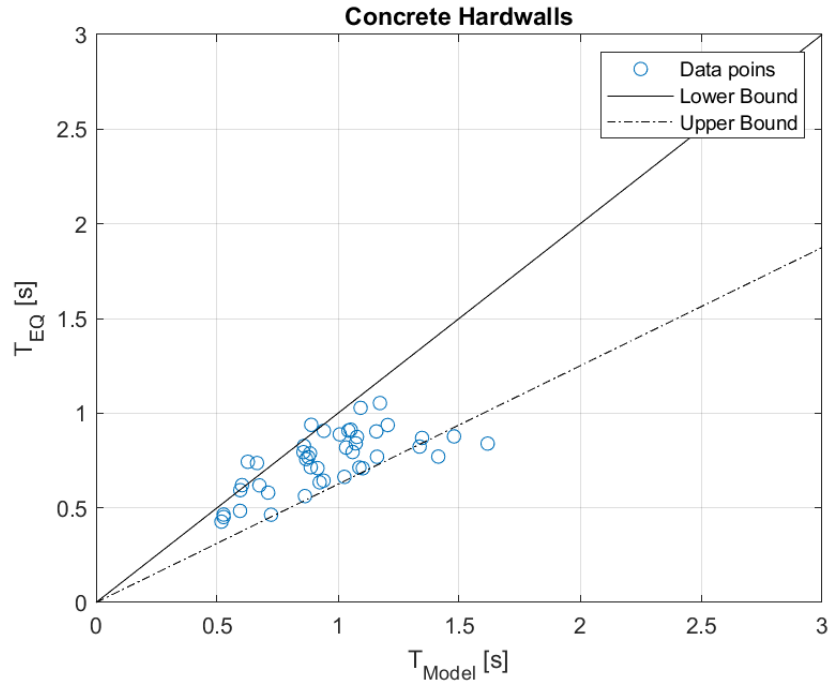


Figure 6.4: Performance of the alternative proposal for metal buildings with concrete hardwalls using Smith and Uang’s data set

6.5 Equation performance in tested buildings

Finally, it is worth revisiting the buildings tested as part of this project and evaluate whether the new proposed equations offer suitable lower bounds for their period, as covered in the previous Chapter for the Smith and Uang formula. Table 6.3 shows the result for the 5 buildings that exhibited pinned behavior at the base, with T_1 being the estimated period using Smith and Uang’s formula, T_2 the period using their refined equation (which was shown to correlate very well with 2D-modeling) and T_a the period estimated with Equation 6.8.

Table 6.3: Fundamental period of tested buildings using the new proposed equations

Name	D_c [psf]	W [kips]	T_1 [s]	T_2 [s]	T_a [s]	T_a/T_2
VA-1	3	9.4	0.61	0.54	0.50	0.93
VA-2	5	24.5	0.70	0.49	0.66	1.35
WV-2	2	16.4	0.67	0.92	0.67	0.73
NC-1	7	21.0	0.77	0.89	0.62	0.70
NC-2	3	9.7	0.60	0.81	0.49	0.60

The results show that the new equation is indeed providing a lower-bound estimate for all buildings except building VA-2, which had appendices, with ratios ranging from 0.6% to 0.93%. VA-1, for which the Smith and Uang equation was overpredicting the period, now falls within the boundaries with the new formula. Compared to Smith and Uang the resulting underprediction tends to be bigger, though this was expected as Equation 6.8 was developed with buildings in high seismic regions, while the buildings tested were in low seismic regions. Either way, with the exception of building NC-2, all buildings fall within the upper bound as well (for building NC-2, the difference between the upper-bound and the modeled period is 4%). Note that, comparing to the results using the ASCE-7 equation (see Table 5.2), the proposed equation still predicts periods that can be as much as double those obtained with the current code provisions.

Chapter 7

Observations on the application of the Equivalent Lateral Force Method

7.1 Introduction

The final chapter is meant to provide a preliminary analysis on the consequences of the observations made in Chapter 4 about the dynamic behavior of metal buildings.

A case study will be evaluated, in order to see if the behavior seen during experimental testing, with the global mode shapes due to stiffness of secondary framing and low mass participation ratios has an effect of the base shear distribution to the different frames in a metal building system.

It should be noted that this is not the only potential issue with the application of ELF. As mentioned by Smith, low mass participation was also seen at the individual frame level, which may mean that higher order modes could affect the moment and shear diagrams (Smith, 2013). Similarly, it was found that that some buildings exhibited large vertical deformations, which are not accounted for introducing forces as purely horizontal when using ELF. Remember that the forces from ELF are the result of considering the deformed shape, and so if the mode shape has large vertical deformations then the equivalent forces may need to include vertical components along the beams. Given that metal buildings are

heavily optimized structures, and that alternating lateral torsional buckling of the rafter seems to govern the inelastic behavior of the frames, more work should be done to obtain procedures that can accurately calculate the bending moment diagram given the base shear. The procedure found in the guide by MBMA ([MBMA, 2019b](#)), which consists of point loads at each beam column joint, should be evaluated to see if leads to satisfactory results or if this methodology could be improved by, for example, considering the base shear as distributed along the roof.

7.2 Simplified N-DOF model of a metal building

As discussed in Chapter 4, the first mode in metal building systems exhibit very low mass participation ratios, well below the 0.9 threshold typically used to be allowed to consider only the first mode in the analysis. Building WV-2, for example, had a mass participation factor of 0.4 based on its 3D-model. With the first mode only exciting the frames in the interior of the building ([Figure 4.46](#)).

Along these lines, as shown for building NC-2, the roof diaphragm of metal buildings does not qualify as flexible when checked following ASCE-7. Again, this should not be taken as indication that the flexible diaphragm assumption shouldn't be used, as history has shown that metal buildings designed this way have performed well during earthquakes. If anything, it may be a commentary on how difficult it is to actually fulfill the ASCE-7 provisions for flexible diaphragms.

In any case, the objective of this section is to evaluate how the base shear of each frame applying the ELF procedure and flexible diaphragm assumption compares to the result of considering the low mass participation ratios and purlin/girt stiffness observed in test data and the associated 3D models.

To that end, a simplified multiple degree-of-freedom model of building WV-2 was designed. This model consists of a series of linear springs representing the different frame lines, interconnected by another set of springs representing the purlin and girt stiffness. Figure 7.1 presents a generic version of this model, which is essentially identical as the one used by Sparks and Sockalingam for calibrating metal building parameters (Sparks and Sockalingam, 1988).

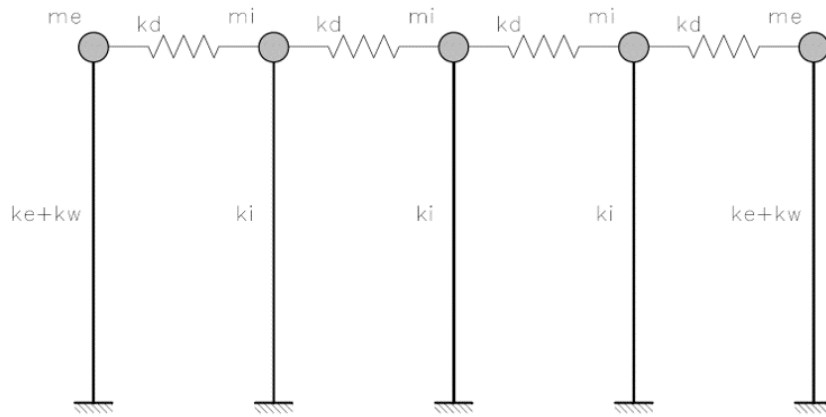


Figure 7.1: Generic example of a simple N-DOF model for 3D analysis of metal buildings.

The generic model for a metal building with n frames can be described in terms of the stiffness of frame i , k_i , its mass m_i , and the stiffness of the deck k_d as follows

$$K = \begin{bmatrix} k_1 + k_d & -k_d & & & \\ -k_d & k_2 + 2k_d & -k_d & & \\ & -k_d & k_3 + 2k_d & -k_d & \\ & & & \ddots & \\ -k_d & & & & k_n \end{bmatrix}, \text{diag}(M) = \begin{Bmatrix} m_1 \\ m_2 \\ m_3 \\ \dots \\ m_n \end{Bmatrix} \quad (7.1)$$

where K is the global stiffness matrix and M is the global mass matrix. For this model, the following properties were used:

- $k_i = 2.27kip/in$, $i = 1, 2, 4, 5, 6, 7, 8$
- $k_i = 39.28kip/in$, $i = 3, 9$
- $k_d = 1.33kip/in$
- $m_i = 11.45kip/g$, $i = 4, 5, 6, 7, 8$
- $m_i = 10.64kip/g$, $i = 2$
- $m_i = 8.09kip/g$, $i = 1$
- $m_i = 12.67kip/g$, $i = 3$
- $m_i = 10.12kip/g$, $i = 9$

These were chosen to approximately represent the behaviour of building WV-2. The mode shapes ϕ_i and natural periods T_i of the model can be obtained from the eigenvectors and eigenvalues of $M^{-1}K$, respectively. Similarly, the modal mass M_i , the modal response coefficient γ_i and the mass participation U_{yi} can be computed as

$$M_i = \phi_i^T M \phi_i \quad (7.2)$$

$$\gamma_i = \phi_i^T M r \quad (7.3)$$

$$U_{yi} = \frac{(\gamma_i)^2}{M_T M_i} \quad (7.4)$$

with M_T being the total mass of the system and r being the influence vector, which for this problem is a column vector of 1's. The modal properties of the simplified model are

shown in Table 7.1. Note that the sum of mass participation factors does not reach 0.9 until effectively all modes are considered in the analysis. This is due to the large stiffness of the endwalls, which is why Response Spectrum Analysis (RSA) would require several modes in a complete 3D-model of a metal building. As Langley and Marshall mentioned, it could take “hundreds” of modes to reach 0.9 mass participation (Langley and Marshall, 2017). With modern computational capabilities, this is not necessarily a limitation, however. In any case, since this simplified model has a reduced number of modes, RSA will be used in order to show how the different modes are contributing to the base shear of each frame.

7.3 Base shear distribution among frames

For the purpose of this example, the building will be located in Chester, CT, with site class D. This is “Site 1” in the examples found within the MBMA guide (MBMA, 2019b), and the reader is referred to the book for more information on the design spectrum for this site. The spectral acceleration for each mode, S_i are also in Table 7.1. Comparing with Figure 4.49, it can be shown that natural periods of the first two modes are roughly equivalent to those of the full 3D model. The participation factor is larger, mainly due to the lumped mass formulations as the mass on the bottom half of the structure is not accounted for. This was considered good enough for a preliminary analysis. The mode shapes (shown in Figure 7.2) were also similar.

In order to obtain the maximum base shear in each frame i , the contribution of each mode j to the base shear of said frame must be calculated. Given the spectral acceleration for mode j , S_{aj} , the spectral displacement D_j can be computed as

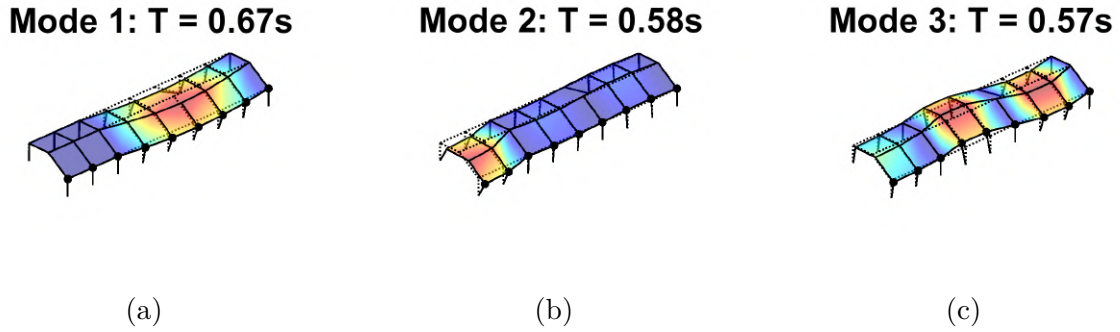


Figure 7.2: First three modes for simplified WV-2 model.

Table 7.1: Modal properties of simplified proxy of building WV-2

Mode	T_i [s]	M_i [kip/g]	γ_i [kip/g]	U_i	S_{ai} [g]
1	0.67	11.45	-25.11	0.56	0.048
2	0.58	9.29	17.72	0.18	0.056
3	0.57	11.22	4.11	0.02	0.056
4	0.49	11.45	-6.73	0.04	0.061
5	0.43	11.45	-2e-3	2e-9	0.061
6	0.42	9.26	-1.47	2e-3	0.061
7	0.40	11.45	1.84	3e-3	0.061
8	0.18	12.66	-11.76	0.11	0.061
9	0.16	10.12	-9.75	0.095	0.061

$$D_j = \left(\frac{T_j}{2\pi} \right)^2 S_{aj} \tag{7.5}$$

from which the maximum displacement of frame i due to the response of mode j , $Y_{i,j}$ can be taken as

$$Y_{i,j} = \phi_{i,j} \frac{\gamma_j}{M_j} D_j \tag{7.6}$$

Finally, the base shear $V_{i,j}$ in each frame i due to mode j is simply the displacement of the frame times its stiffness

$$V_{i,j} = k_i Y_{i,j} \quad (7.7)$$

Finally, mode combinations rules such as CQC can be used to find the maximum total base shear of each frame V_{Ti} (Chopra, 2017). The result of this analysis can be found Table 7.2. For comparison, the result of using the equivalent lateral force procedure assuming independent behavior of the frames is shown as V_{ELFi}

Table 7.2: Distribution of base shear among frames based on RSA and ELF, in units of *kip*

Mode Frame	1	2	3	4	5	6	7	8	9
1	7.4E-03	9.7E-03	1.9E-01	3.1E-01	5.2E-01	6.0E-01	5.2E-01	3.1E-01	1.9E-01
2	4.2E-01	3.5E-01	2.6E-01	7.7E-02	6.7E-02	-6.2E-03	-7.3E-02	-7.2E-02	-4.4E-02
3	3.7E-02	3.0E-02	-2.5E-02	-7.1E-02	-7.1E-02	-5.5E-04	7.0E-02	7.2E-02	4.5E-02
4	-4.1E-03	-4.0E-04	6.9E-02	1.1E-01	-1.3E-03	-1.1E-01	-1.3E-03	1.1E-01	7.0E-02
5	-1.1E-06	6.9E-07	1.2E-05	1.7E-05	-1.8E-05	1.3E-08	1.8E-05	-1.7E-05	-1.1E-05
6	-2.7E-02	2.5E-02	1.6E-02	-6.4E-04	-2.4E-05	6.8E-04	-9.3E-04	6.4E-04	4.3E-04
7	6.8E-04	-7.8E-04	6.3E-03	1.0E-02	-1.8E-02	2.0E-02	-1.8E-02	9.9E-03	6.8E-03
8	9.6E-05	-1.7E-03	6.7E-01	-1.5E-03	6.2E-05	-2.5E-06	1.0E-07	-4.0E-09	-1.3E-08
9	2.9E-13	-6.3E-12	3.1E-09	-1.2E-09	3.6E-08	-1.1E-06	3.5E-05	-1.1E-03	5.7E-01
V_T	4.5E-01	3.8E-01	7.7E-01	3.4E-01	5.2E-01	6.0E-01	5.2E-01	3.3E-01	6.1E-01
V_{ELF}	4.3E-01	4.9E-01	7.7E-01	5.1E-01	5.1E-01	5.1E-01	5.1E-01	5.1E-01	6.2E-01

From the Table there are two major takeaways. The first is that the first mode is not always the one driving the maximum response in the frames. The base shear in Frame 1, on the left end of the structure, is largely dominated by the response of the second mode of the building. This makes sense if we go back to Figure 4.49, where it's shown that frame 1 did not participate in the mode shape of mode 1, but was displaced the most in mode 2.

The other main observation is that the base shear in some frames resulting from doing a RSA can be larger than those obtained from ELF. The reasoning for this is two-fold. On one end, the period of higher mode shapes is shorter, and so their spectral acceleration is higher, resulting in larger displacements and larger forces. Such is the case in frame 1, where V_{T1} is 5.5% larger than V_{ELF1} . More significantly, frame 6 exhibits a 17% increase in base shear

when considering the the effect of the secondary framing in the response.

Consequently, the example here shows that ELF may not be applicable to metal buildings due to their flexible nature and low mass participation ratio in the first mode. However, it should be noted that this analysis assumes that the secondary framing is behaving elastically and its stiffness remains unchanged. Whether this is possible under design level loads is not clear. It's not clear how Langley modeled the secondary framing behavior, as much of the discussion on the nonlinear modelling is focused on other elements of the structure (Langley, 2016).

Another point that should be made is that, in the example above, Frame 6 (if designed with ELF) would start exhibiting nonlinear behavior earlier than the rest of the frames, and it may be possible for the seismic load to redistribute to other frame lines creating a more uniform base shear distribution in the end. However, this would also mean that the drift along frame line 6 would be larger than that predicted with a 2D-analysis. Work by Smith (Smith, 2013) showed that metal building moment frames can exhibit very large amount of drift before collapse, and so it's plausible that the increased ductility demand this case study is implying would not negatively impact the design of metal buildings with metal panels. However, the potentially larger drift may have an effect on the safety of buildings with hardwalls.

Only nonlinear 3D-analysis would be able to answer the questions here presented, mainly regarding the maximum drift during the design earthquake, and whether designs using ELF and 2D-analysis can accommodate the increased loading and displacements in certain frames that this case study imply, and if the current value of C_d for estimating the inelastic displacement is adequate for metal buildings as is.

Chapter 8

Conclusions and Future Work

8.1 Summary

Initial Objectives

The purpose of this work was to provide a better understanding of the structural behavior of metal building systems – namely their fundamental period – looking at the influence of non-structural elements and evaluating how different modeling approaches of varied levels of complexity (2D and 3D) perform as predictors. As part of this work, the results were used to assess the accuracy the assumptions made by Uang and Smith that led to the development of their period estimation formulas, as well as validate the equations themselves. Given that past test data, as well as experiences in other types of single-story buildings seemed to imply that non-structural elements and cladding could be playing a significant role in the dynamic response of metal buildings, it was decided to carry out an experimental testing program that could help provide an answer on whether this was the case for metal buildings as well.

Experimental testing

Seven buildings were tested in total using ambient vibration data, four of them in different stages of construction for a total of thirteen tests. To the author's knowledge, this is the first study of its kind for metal buildings. The tests across construction stages – before and after the cladding was installed – showed that the endwall stiffness is affected by their cladding, though the cladding stiffness could not be evaluated from the test results as the endwalls tended to become essentially infinitely rigid compared to the flexible interior frames.

The difference in period between tests results across construction stages also showed that that the introduction of the roof cladding did not affect the fundamental mode of the buildings, implying that no diaphragm action was being developed. This result seems to be unique to metal buildings, as other experiences in Europe and Canada for single-story buildings showed significant changes in stiffness after the inclusion of non-structural elements.

Analytical Modeling of metal buildings

3D models were created for all buildings and all stages of construction. These 3D models assumed a pinned base, and a simplified geometry and connections between the secondary and primary framing. They also used a centerline model for the panel zone of the beam-column joint. These models were shown to accurately describe the behavior of metal building in all cases where bare frame testing was possible.

Some buildings showed an increased stiffness compared to what was predicted by the models. Unfortunately, none of these buildings was tested before its final configuration. However, the results from other tests, as well as the mode shape information implies that the main reason for this was an increased fixity at the base of the columns. In fact, in all cases updating the model to a fixed base provided accurate results for the fundamental period.

The applicability of 2D modelling for metal buildings was also evaluated by looking at their correlation with both 3D modeling results and the test data. Results showed that 2D modeling of isolated frames can accurately predict the fundamental period.

Evaluation of Smith and Uang's formulas

Given that the weight of the buildings during testing did not match the values used for design, the stiffness obtained from the models, validated against the experimental results, was used to extrapolate the natural period for the design seismic weight. For regular buildings without appendices, the Smith and Uang's formula seemed to provide a reasonable lower estimate of the natural period. In fact, the "best guess" estimate from the linear regression proved to be within 10% of the extrapolated periods.

The refined equation based Rayleigh's method was also studied, and in all cases it showed excellent correlation with a full dynamic analysis of the buildings.

The buildings tested were estimated to represent only about 37% of the built environment. Looking into the different types of building types included in Smith and Uang's formula, it was found that that the equation may severely overpredict the period for buildings with concrete walls in high seismic areas. Given that seismic loads are critical to the safety of these structures, it would be prudent to evaluate them separately from the rest of the buildings. In fact, building with concrete panels in general seemed to be more sensitive to loading conditions, and so grouping all buildings classes into a single equation may result in overpredicting the period for certain types of buildings.

Building NC-2, with an aspect ratio close to 3, showed that the discontinuity in the formula should be addressed. Abnormally large weights for some buildings used in the regression should also be revised to avoid introducing bias into the equation

Development of new period estimation equations

Based on the above, two new period estimation equations were developed for metal buildings: one for buildings with with metal sheeting and one for concrete hardwalls. These equations were developed in semi-empirical fashion, with the controlling parameters being obtained from rational analysis of a single-story moment frame and the final constants calibrated using standard linear regression.

These equations focused only on buildings in high seismic regions, where seismic loads may govern the design and are consistent with the current formulas in ASCE-7. The equations proposed are continuous, and exhibited similar or reduced levels of scatter compared to the equations developed by Goel and Chopra for mid-rise construction.

It should be noted that these new proposed equations are only applicable for the interior moment frames of standard metal building systems with no appendices, and do not apply to the endwall framing.

Applicability of the ELF method

The 3D models, validated against the test results, showed that first mode of metal buildings exhibit very low mass participation factors, and evaluation of the flexible diaphragm assumption showed that, even if the roof diaphragm provided no additional stiffness, the secondary framing was enough to qualify the diaphragm as semirigid. These two results together imply that the ELF method may not be applicable to metal buildings.

A preliminary analysis using a simplified N-DOF model showed that the ELF method may underestimate the base shear which could also lead to larger inelastic displacements if designed using ELF. However, the consequences for this in design are not known.

8.2 Main Conclusions

- A new data base with metal building tested during different phases of construction has been developed, the first for these types of buildings
- The cladding in the endwalls of metal buildings can significantly increase their stiffness. This, however, does not affect the fundamental period of the buildings, which is controlled by the stiffness of the interior frames. This is due to the flexibility of the roof diaphragm, which allows for the interior frames to deform without being restrained by the end walls.
- The roof cladding does not seem to provide any diaphragm action, and its stiffness can be considered to be negligible, which is consistent with low values reported by previous tests on roof assembly. Effectively all the stiffness at the roof level is provided by the purlins and not the sheeting.
- 2D models of metal buildings are just as capable as 3D models in predicting the fundamental period. However, important information regarding mode shapes and mass participation factors are lost.
- Some metal buildings exhibit what seems to be unintended rotational stiffness at the base of the columns, and more work needs to be done to understand what construction details may cause this, and whether it's representative of the behavior at higher amplitudes.
- The Smith and Uang formula can provide reasonable lower bound estimates for metal buildings with metal panels as long as they exhibit pinned base behavior. However, a non-negligible number of tests have so far been more consistent with a fixed base connection.

- The Smith and Uang formula may severely overestimate the period for metal buildings with concrete walls in high seismic areas. These buildings had very low contribution to linear regression due to low weights. Buildings with concrete walls seemed to be more sensitive to loading conditions and this should be accounted for in a period estimation equation.
- New prediction equations for adoption in ASCE-7 are proposed, which includes the effect of the type of cladding and provide reasonable lower bounds for the tested buildings. These equations were calibrated based on a rational analysis for the parameter estimation and using standard linear regression on metal buildings in high seismic regions.
- The ELF method may underestimate the base shear in some frame lines of a metal building system when compared to the results of a 3D model, though the consequences and significance of this are yet to be explored.
- Since the period of the endwalls was not able to be extracted from experimental tests, no real recommendation can be offered. However, they seem to be much stiffer than the interior frames, and so the current equations in ASCE-7 are probably sufficient as they would make the base shear be governed by the plateau of the spectral acceleration plot.

8.3 Future Work

Given the results, future research should focus on why some column bases exhibit significantly larger rotational stiffness despite similar details on the structural drawings. Full scale testing for different configurations is recommended to see if the fixed base condition is an artifact

of low level vibrations or a direct result of the base detail.

The new proposed equations for period estimation are applicable as long as the synthetic database created by Smith and Uang is an accurate representation of the true behavior of metal building systems. This can only be reasonably justified for buildings with metal panels based on the tests carried out in this work, though there is no reason to believe at the moment that different conclusions will be reached for buildings with concrete hardwalls. Either way, the database of tested buildings should be expanded to cover current shortcomings. Modular frames with large seismic weights, buildings with concrete walls, and metal buildings in high seismic and wind regions need to be tested in order to provide certainty that the database developed by Smith and Uang is consistent with the built environment.

Finally, the applicability of the ELF procedure should be studied in detail. 3D, nonlinear response history analysis is recommended to evaluate the interaction between the primary and secondary framing under design level loads, as well as looking at the inelastic displacements and drift demands in the most loaded frames. A 2D analysis may not be enough to ensure adequate reliability.

Bibliography

- AISI S310-16 (2016). *North American Standard for the Design of Profiled Steel Diaphragm Panels, 2016 Edition*. American Iron and Steel Institute, Washington, D.C.
- Allemang, R. J. (2003). The modal assurance criterion - twenty years of use and abuse. *Sound and Vibration*.
- Antoni, J. (2006). The spectral kurtosis: a useful tool for characterising non-stationary signals. *Mechanical Systems and Signal Processing*, 20(2):282–307.
- ASCE/SEI 7-16 (2017). *Minimum Design Loads and Associated Criteria for Buildings and Other Structures*. American Society of Civil Engineers, Reston, VA.
- Avcı, O., Luttrell, L. D., Mattingly, J., and Easterling, W. S. (2016). Diaphragm shear strength and stiffness of aluminum roof panel assemblies. *Thin-Walled Structures*, 106:51–60.
- Bajwa, M. S. (2010). Assessment of analytical procedures for designing metal buildings for wind drift serviceability. Master's thesis, Virginia Tech, Blacksburg, VA.
- Bajwa, M. S., Charney, F. A., and Moen, C. D. (2010). Assessment of analytical procedures for designing metal buildings for wind drift serviceability. Technical Report No. CE/VPI-ST 10/05, Virginia Tech, Blacksburg, VA.
- Brinker, R. and Ventura, C. E. (2015). *Introduction to Operational Modal Analysis*. John Wiley and Sons, Ltd, Chichester, UK.

- Charney, F. A. (2008). A transformational approach to teaching matrix structural analysis, and visual implementation using mathcad. In *Structures Congress 2008*, Vancouver, Canada.
- Charney, F. A., Heausler, T. F., and Marshall, J. D. (2020). *Seismic Loads: Guide to the Seismic Load Provisions of ASCE 7-16*. American Society of Civil Engineers, Reston, VA.
- Charney, F. A., Iyer, H., and Spears, P. W. (2005). Computation of major axis shear deformations in wide flange steel girders and columns. *Journal of Constructional Steel Research*, 61(11):1525–1558.
- Charney, F. A. and Marshall, J. D. (2006). A comparison of the krawinkler and scissors models for including beam column joint deformations in the analysis of moment resisting steel frames. *AISC Engineering Journal*, 43:23–48.
- Charney, F. A. and Pathak, R. (2008a). Sources of elastic deformation in steel frame and framed-tube structures: Part 1: Simplified subassemblage models. *Journal of Constructional Steel Research*, 64(1):87–100.
- Charney, F. A. and Pathak, R. (2008b). Sources of elastic deformations in steel frame and framed-tube structures: Part 2: Detailed subassemblage models. *Journal of Constructional Steel Research*, 64(1):101–117.
- Chopra, A. K. (2017). *Dynamics of Structures: Theory and Applications to Earthquake Engineering*. Pearson, Hoboken, NJ, 5th edition.
- CSI (2021). *SAP2000 Integrated Software for Structural Analysis and Design*. Computers and Structures Inc., Berkeley, CA.
- Davies, J. M. (2006). Developments in stressed skin design. *Thin-Walled Structures*, 44(12):1250–1260.

- Davies, J. M. and Bryan, E. R. (1982). *Manual of Stressed Skin Diaphragm Design*. Granada Publishing, London, England.
- Döhler, M. and Mevel, L. (2013). Efficient multi-order uncertainty computation for stochastic subspace identification. *Mechanical Systems and Signal Processing*, 38(2):346–366.
- ECCS (1995). *European Recommendations for Application of Metal Sheetting Acting as Diaphragm No. 88*. TC7, European Convention for Constructional Steelwork.
- Fischer, A. W. and Schafer, B. W. (2021). Wall-diaphragm interactions in seismic response of single-story building systems. *Engineering Structures*, 247:113150.
- Fisher, J. M. and Nunnery, J. N. (1996). Stability of standing seam roof-purlin systems. In *13th International Specialty Conference on Cold-Formed Steel Structures*, St Louis, MO.
- Goel, R. K. and Chopra, A. K. (1997). Period formulas for moment-resisting frame buildings. *Journal of Structural Engineering*, 123(11):1454–1461.
- Gryniewicz, M., Roberts, M. J., and Davies, J. M. (2021). Testing and analysis of a full-scale steel-framed building including the consideration of structure-cladding interaction. *Journal of Constructional Steel Research*, 181:106611.
- Kim, J. Y., Yu, E., Kim, D. Y., and Kim, S.-D. (2009). Calibration of analytical models to assess wind-induced acceleration responses of tall buildings in serviceability level. *Engineering Structures*, 31(9):2086–2096.
- Kohler, M. D., Davis, P. M., and Safak, E. (2005). Earthquake and ambient vibration monitoring of the steel-frame ucla factor building. *Earthquake Spectra*, 21(3):715–736.
- Kumar, A., Charney, F. A., and Sarlo, R. (2020). Development of methodology for measuring the period of vibration for metal buildings. Technical Report No. CE/VPI-ST 20/04, Virginia Tech, Blacksburg, VA.

- Lamarche, C.-P., Proulx, J., Paultre, P., Turek, M., Ventura, C. E., Le, T. P., and Lévesque, C. (2009). Toward a better understanding of the dynamic characteristics of single-storey braced steel frame buildings in Canada. *Canadian Journal of Civil Engineering*, 36(6):969–979.
- Langley, M. and Marshall, J. D. (2017). 3-d analytical modeling of metal building systems with hard walls. In *16th World Conference on Earthquake Engineering*, Santiago, Chile.
- Langley, M. J. (2016). 3-d model development of metal building systems with hard walls. Master's thesis, Auburn University, Auburn, AL.
- Langley, M. J. (2018). *Development, Testing, and Analysis of a Rotational Friction Connection for Improving the Seismic Performance of Metal Building Systems with Hard Walls*. PhD thesis, Auburn University, Auburn, AL.
- Liu, K.-S. and Tsai, Y.-B. (2010). Observed natural frequencies, damping ratios, and mode shapes of vibration of a 30-story building excited by a major earthquake and typhoon. *Earthquake Spectra*, 26(2):371–397.
- Luttrell, L. D., Mattingly, J. A., Schultz, W., and Sputo, T. (2015). *Diaphragm Design Manual*. Steel Deck Institute, St. Louis, MI, 4th edition.
- Luttrell, L. D. (1965). *Structural Performance of Light Gage Steel Diaphragms*. PhD thesis, Cornell University, Ithaca, NY.
- Luttrell, L. D. and Mattingly, J. A. (2004). *A Primer on Diaphragm Design*. Metal Construction Association, Glenview, IL, 1st edition.
- MBMA (2019a). *Metal Building Systems Manual*. International Code Council, Washington, D.C., 2018 edition.

- MBMA (2019b). *Seismic Design Guide for Metal Building Systems*. International Code Council, Washington, D.C., 3rd edition.
- MBMA (2020). *MBMA Annual Report*. Metal Building Manufacturers Association, Cleveland, OH.
- McGuire, W., Gallagher, R. H., and Ziemian, R. D. (2020). *Matrix Structural Analysis*. Faculty Books, 2nd edition.
- Moen, C. D., Torabian, S., and Schafer, B. W. (2019). Evaluation of metal building system seismic response modification coefficients. Technical Report No. CFSRC;R-2019-05, NBM Technologies, Inc., Blacksburg, VA.
- NBC 2015 (2015). *National Building Code of Canada: 2015*. Canadian Commission on Building and Fire Codes, Ottawa, Canada.
- Newman, A. (2015). *Metal Building Systems: Design and Specifications*. McGraw-Hill Education, New York, NY, 3rd edition.
- Overschee, P. V. and De Moor, B. (1996). *Subspace Identification for Linear Systems*. Kluwer Academic Publishers, Amsterdam, Netherlands.
- Pan, T.-C., Goh, K. S., and Megawati, K. (2014). Empirical relationships between natural vibration period and height of buildings in singapore. *Earthquake Engineering & Structural Dynamics*, 43(3):449–465.
- Peeters, B. and De Roeck, G. (1999). Reference-based stochastic subspace identification for output-only modal analysis. *Mechanical Systems and Signal Processing*, 13(6):855–878.
- Reynders, E., Houbrechts, J., and De Roeck, G. (2012). Fully automated (operational) modal analysis. *Mechanical Systems and Signal Processing*, 29:228–250.

- Reynders, E., Maes, K., Lombaert, G., and De Roeck, G. (2016). Uncertainty quantification in operational modal analysis with stochastic subspace identification: Validation and applications. *Mechanical Systems and Signal Processing*, 66-67:13–30.
- Roberts, M. J., Davies, J. M., and Wang, Y. C. (2021). Numerical analysis of a clad portal frame structure tested to destruction. *Structures*, 33:3779–3797.
- Rogers, C. A. and Tremblay, R. (2010). Impact of diaphragm behavior on the seismic design of low-rise steel buildings. *AISC Engineering Journal*, 47:21–36.
- Sarlo, R., Tarazaga, P. A., and Kasarda, M. E. (2018). High resolution operational modal analysis on a five-story smart building under wind and human induced excitation. *Engineering Structures*, 176:279–292.
- Shan, J., Shi, W., and Wang, J. (2013). Regional study on structural dynamic property of buildings in china. *Earthquake Engineering & Structural Dynamics*, 42(7):1013–1029.
- Smith, M. D. (2013). *Seismic Testing and Analytical Studies for the Development of New Seismic Force Resisting Systems for Metal Buildings*. PhD thesis, University of California, San Diego, La Jolla, CA.
- Smith, M. D. and Uang, C.-M. (2013). Approximate natural periods for metal building moment frames. Technical Report No. SSRP-12/07, University of California, San Diego, La Jolla, CA.
- Sockalingam, B. (1988). A dynamic test procedure for analyzing low-rise metal buildings. Master’s thesis, Clemson University, Clemson, SC.
- Sparks, P. R. and Sockalingam, B. (1988). Frame-diaphragm interaction in an enclosed metal building. Technical report, Clemson University, Clemson, SC.

- Tremblay, R. (2005). Fundamental periods of vibration of braced steel frames for seismic design. *Earthquake Spectra*, 21(3):833–860.
- Tremblay, R. and Rogers, C. A. (2011). Seismic design of low-rise steel buildings with flexible steel roof deck diaphragms – a canadian perspective. *Steel Construction*, 4(4):242–250.
- Trifunac, M. D. (1972). Comparisons between ambient and forced vibration experiments. *Earthquake Engineering & Structural Dynamics*, 1(2):133–150.
- Verma, A. (2012). Influence of column-base fixity on lateral drift of gable frames. Master’s thesis, Virginia Tech, Blacksburg, VA.
- Wei, G., Schafer, B. W., Seek, M., and Eatherton, M. R. (2020). Experimental study on the in-plane behavior of standing seam roof assembly and its use in lateral bracing of rafters. Technical Report No. CFSRC R-2020-02, Cold-Formed Steel Research Consortium, Baltimore, MD.
- White, D. W., Jeong, W. Y., and Slein, R. (2021). Aisc design guide 25: Frame design using nonprismatic members, second edition. Technical report, American Institute of Steel Construction, Chicago, IL.
- Wrzesien, A. M., Lim, J. B., Xu, Y. Y., MacLeod, I. A., and Lawson, R. M. (2015). Effect of stressed skin action on the behaviour of cold-formed steel portal frames. *Engineering Structures*, 105:123–136.
- Xia, Y., Friswell, M. I., and Saavedra Flores, E. I. (2012). Equivalent models of corrugated panels. *International Journal of Solids and Structures*, 49(13):1453–1462.

Appendix A

Plan and Elevation Drawings for Tested buildings

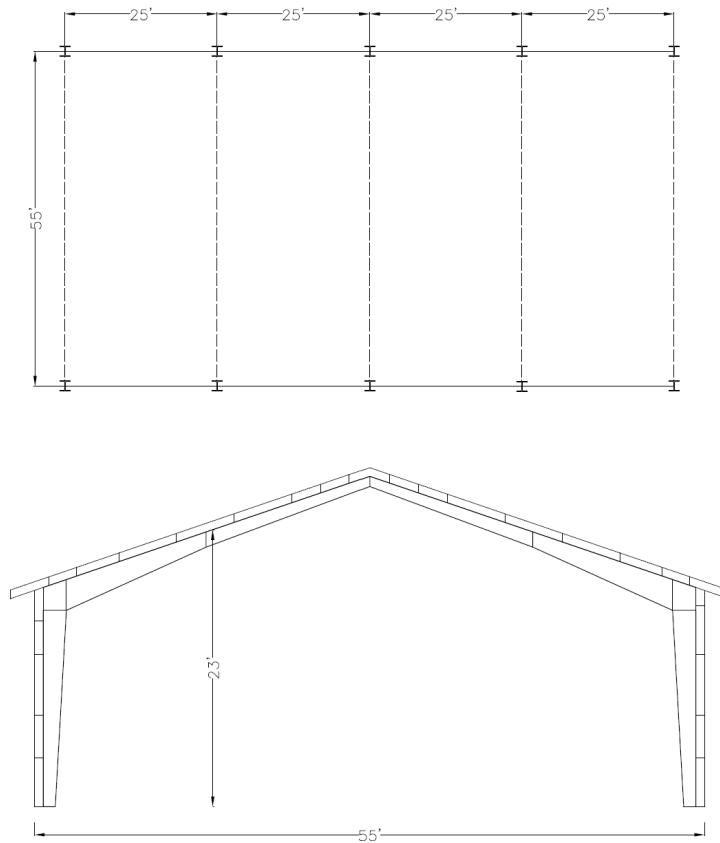


Figure A.1: Plan and elevation drawings for Building VA-1.

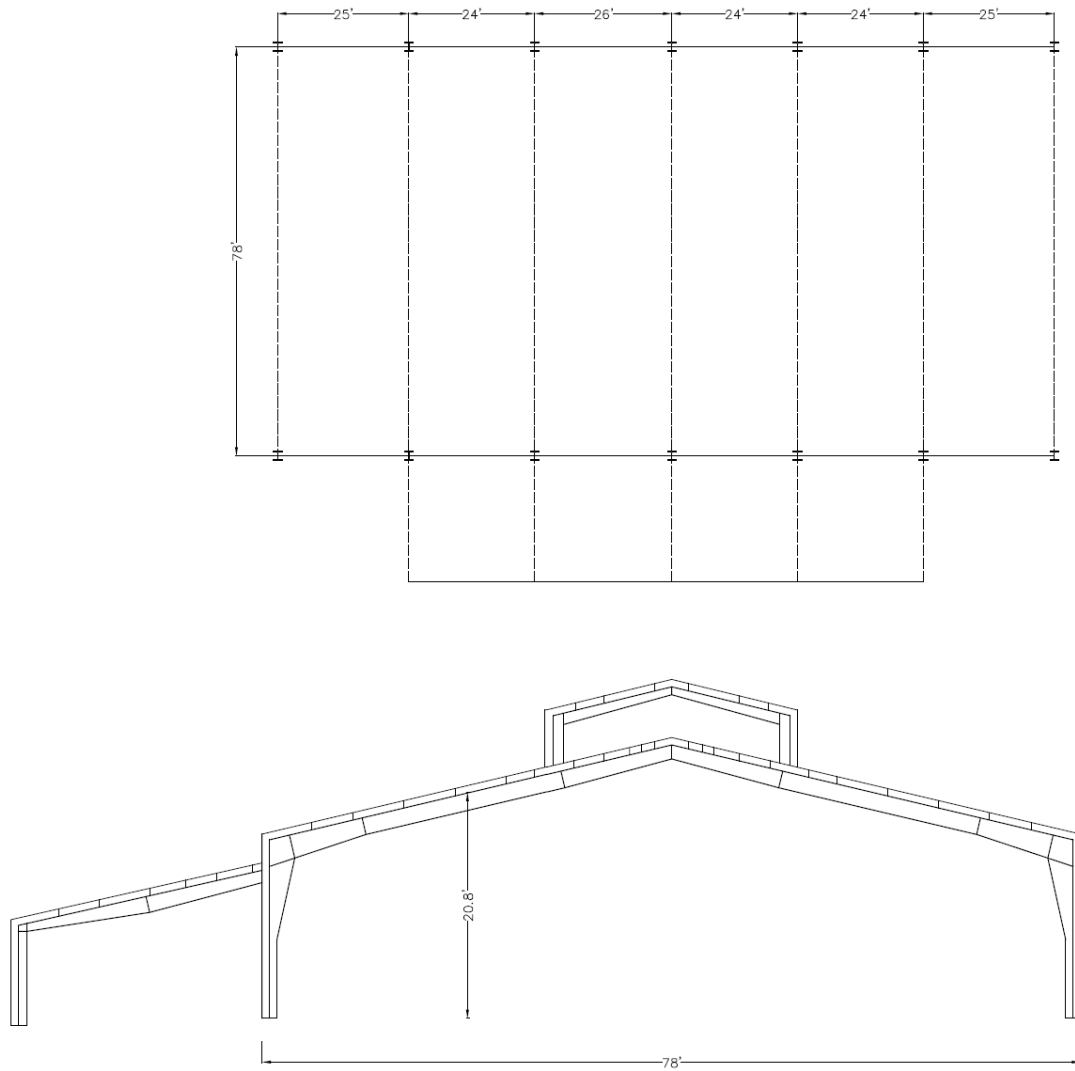


Figure A.2: Plan and elevation drawings for Building VA-2.

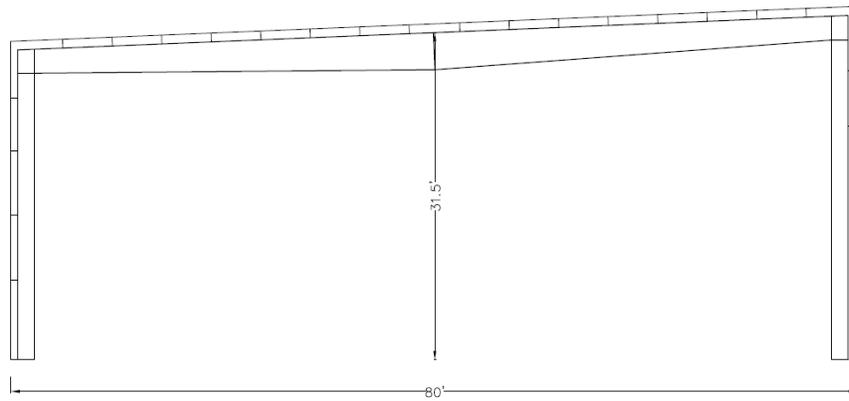
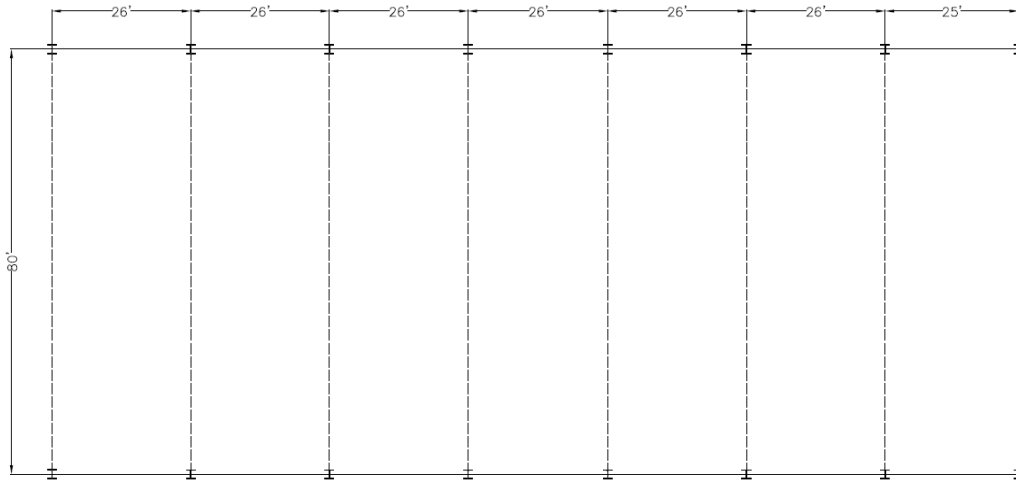


Figure A.3: Plan and elevation drawings for Building WV-1.

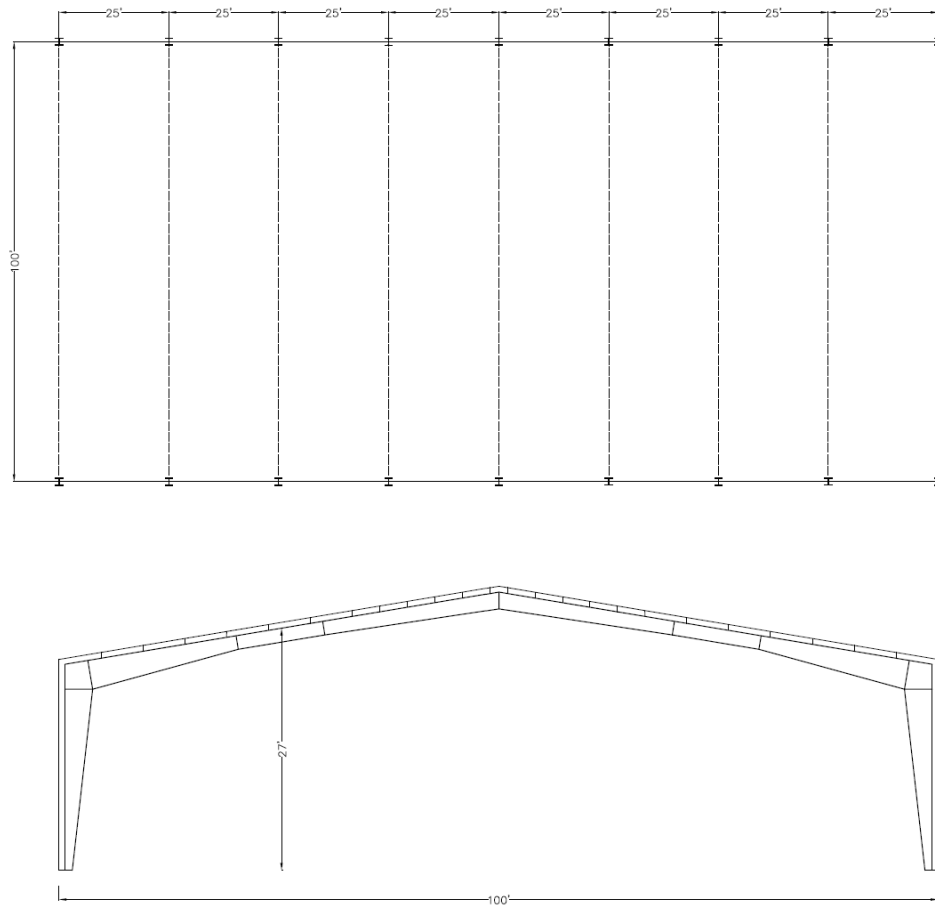


Figure A.4: Plan and elevation drawings for Building WV-2.

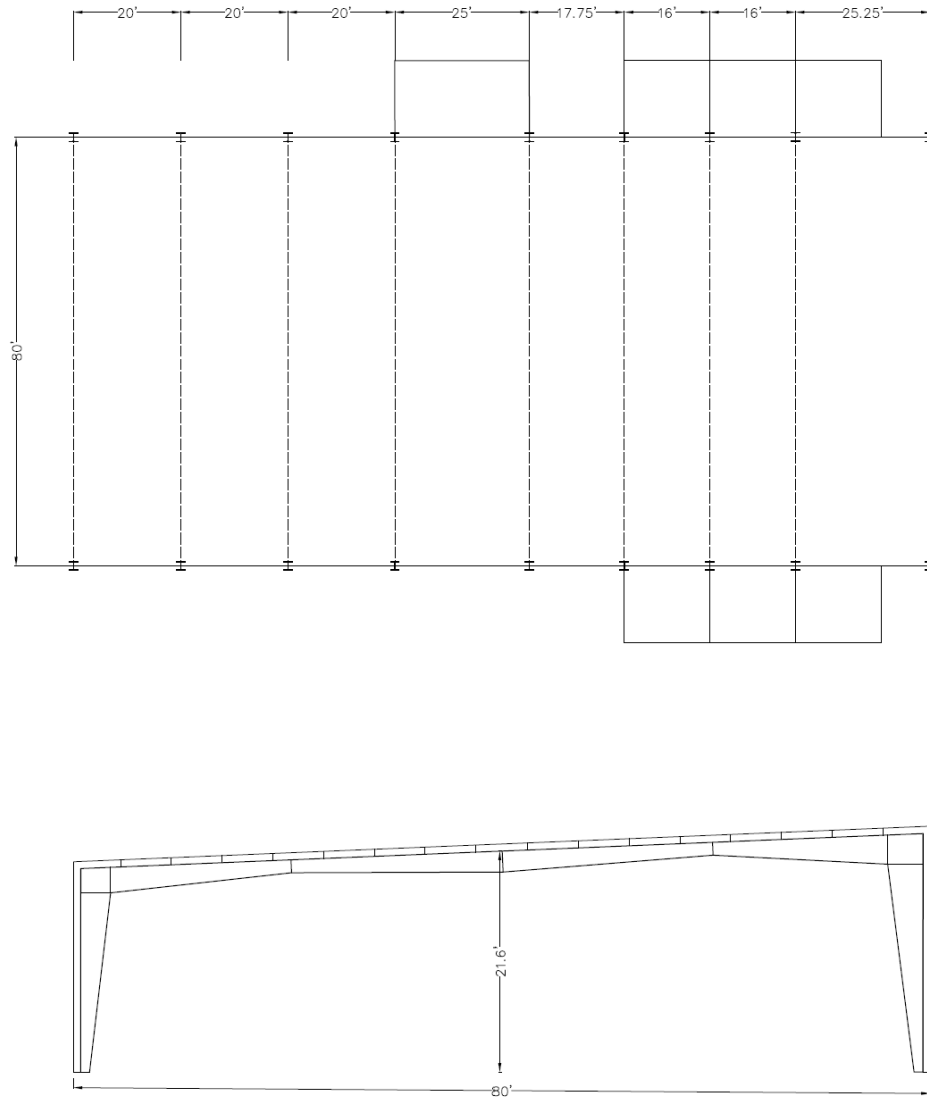


Figure A.5: Plan and elevation drawings for Building NC-1.

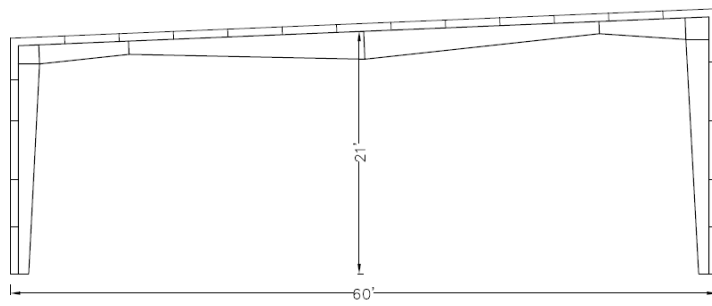
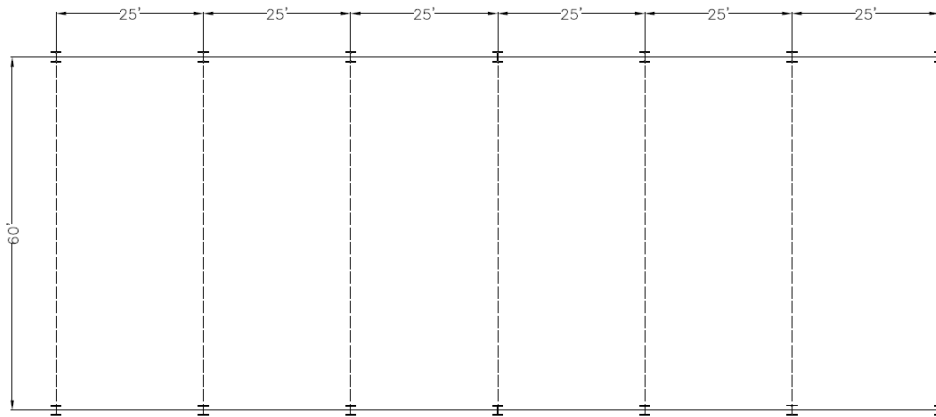


Figure A.6: Plan and elevation drawings for Building NC-2.

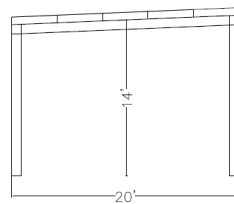
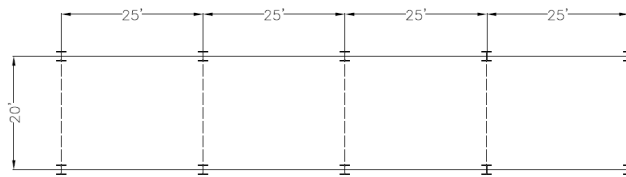


Figure A.7: Plan and elevation drawings for Building NC-3.

Appendix B

Summary of Tests on Fully-Clad Metal Buildings to Date

Table B.1: Summary of properties of the buildings tested to date - structural classification

Name	Cladding	Type	Roof	Partitions	Comments
VA-1	Metal Panels	Clear Span	Gabled	None	N/A
VA-2	Metal Panels	Clear Span	Gabled	None	Appendices in every interior frame, Clerestory
WV-1	Metal Panels	Clear Span	Monoslope	None	Expansion to existing building
WV-2	Metal Panels	Clear Span	Gabled	None	Endwall at an “interior” frame
NC-1	Metal Panels	Clear Span	Monoslope	Heavy	Appendices in several frames
NC-2	Metal Panels	Clear Span	Monoslope	None	N/A
NC-3	Metal Panels	Clear Span	Monoslope	None	N/A
BBTC	Metal Panels	Clear Span	Gabled	None	Mezzanine (Kumar et al., 2020)
VTH	Metal Panels	Clear Span	Gabled	None	Hangar door (Kumar et al., 2020)
VTL	Metal Panels	Clear Span	Gabled	None	2-story structure attached (Kumar et al., 2020)
IBHS C	Metal Panels	Clear Span	Monoslope	Moderate	(Kumar et al., 2020)
IBHS D	Metal Panels	Clear Span	Monoslope	Light	(Kumar et al., 2020)
IBHS G	Metal Panels	Clear Span	Monoslope	Moderate	(Kumar et al., 2020)

Table B.2: Summary of properties of the buildings tested – design parameters and measured period

Name	Length [<i>ft</i>]	Height h_n [<i>ft</i>]	Aspect Ratio α	Weight W [<i>kips</i>]	Period T [<i>s</i>]
VA-1	55	23	2.39	5.3	0.43
VA-2	78	20.8	3.74	11.5	0.31
WV-1	80	31.5	2.54	9.5	0.38
WV-2	100	27	3.70	11.4	0.72
NC-1	80	21.6	3.70	7.0	0.50
NC-2	60	21	2.86	5.2	0.63
NC-3	20	14	1.43	1.8	0.15
BBTC	120	29.75	4.03	16.0	0.50
VTH	140	30	4.67	20.6	0.39
VTL	54	27.75	1.95	11.7	0.21
IBHS C	60	24.3	2.47	10.0	0.19
IBHS D	55	37	1.49	8.3	0.33
IBHS G	40	21.6	1.85	6.5	0.18